ANALYSIS OF HMA PERMEABILITY THROUGH MICROSTRUCTURE CHARACTERIZATION AND SIMULATION OF FLUID FLOW IN X-RAY CT IMAGES

A Dissertation

by

ASLAM ALI MUFLEH AL OMARI

Submitted to the Office of Graduate Studies of
Texas A&M University
in partial fulfillment of the requirements for the degree of

DOCTOR OF PHILOSOPHY

December 2004

Major Subject: Civil Engineering

ANALYSIS OF HMA PERMEABILITY THROUGH MICROSTRUCTURE

CHARACTERIZATION AND SIMULATION OF FLUID FLOW IN X-RAY CT

IMAGES

A Dissertation

by

ASLAM ALI MUFLEH AL OMARI

Submitted to Texas A&M University
in partial fulfillment of the requirements
for the degree of

DOCTOR OF PHILOSOPHY

Approved as to style and content by:

Eyad Masad	Dallas Little
(Chair of Committee)	(Member)
Robert Lytton	Hamn-Ching Chen
(Member)	(Member)
Charles Glover	Paul Roschke
(Member)	(Head of Department)

December 2004

Major Subject: Civil Engineering

ABSTRACT

Analysis of HMA Permeability through Microstructure Characterization and Simulation

of Fluid Flow in X-Ray CT Images. (December 2004)

Aslam Ali Mufleh Al Omari, B.S., Jordan University of Science and Technology;

M.S., Jordan University of Science and Technology

Chair of Advisory Committee: Dr. Eyad Masad

The infiltration of water in asphalt pavements promotes moisture damage primarily through damaging the binder cohesive bond and the adhesive bond between aggregates and binder. Moisture damage is associated with excessive deflection, cracking, and rutting. The first step in addressing the problems caused by the presence of water within pavement systems is quantifying the permeability of hot mix asphalt (HMA) mixes. This dissertation deals with the development of empirical-analytical and numerical approaches for predicting the permeability of HMA. Both approaches rely on the analysis of air void distribution within the HMA microstructure.

The empirical-analytical approach relies on the development of modified forms of the Kozeny-Carman equation and determining the material properties involved in this equation through three dimensional microstructure analyses of X-ray Computed Tomography (CT) images. These properties include connected percent air voids (effective porosity), tortuosity, and air void specific surface area. A database of materials and permeability measurements was used to verify the developed predicting equation.

The numerical approach, which is the main focus of this study, includes the development of a finite difference numerical simulation model to simulate the steady incompressible fluid flow in HMA. The model uses the non-staggered system that utilizes only one cell to solve for all governing equations, and it is applicable for cell Reynolds number (Re_c) values that are not restricted by $|Re_c| \leq 2$. The validity of the numerical model is verified through comparisons with closed-form solutions for idealized microstructure.

The numerical model was used to find the components of the three-dimensional (3-D) permeability tensor and permeability anisotropy values for different types of HMA mixes. It was found that the principal permeability directions values are almost in the horizontal and vertical directions with the maximum permeability being in the horizontal direction.

DEDICATION

I dedicate this dissertation to the best family on this earth to my father, Ali Al-Omari; to my mother, Anaam Al-Omari; to my sisters, Wesal, Najat, Abeer, Islam, and Rasha; to my brothers, Ashraf, Mohammad, and Tareq; to my colleagues at Texas A&M University (TAMU), Ahmad Al Waked, Khaled Qaraqe, Khaled Mriziq, Rasheed Jaradat, Taleb Al-Rousan, Mohammad Rababaah, Abdulrahman Al Deeb, Mohammad Mohammad, Adnan Jaradat, Shadi Saadeh, Samer Dessouky, Tareq Abdallah, Mohammad Jaradat, Maan Abdelraheem, Walid Alaaly, Emad Qasem, Samer Kiswani, and Enad Mahmoud; to my colleagues at Washington State University (WSU), Omar Hatamleh, Firas Awwadi, Ayman Al-Omari, Nasim Shattarat, Murad Al-Holy, Mutasem Shehadeh, and Alaa Abbas; to my best friends, Khaled Abu Laila, Nabil Al-Jarrah, Ahmad Bdour, Yazan Khasawneh, and Ahmad Al-Bzour; and to my uncles, aunts, cousins, and my dear nephew, Qosay Al-Bzour. I dedicate this dissertation to the above persons, to all who care about me, and to those whom I love for their support and help in accomplishing my graduate study in the United States of America.

ACKNOWLEDGMENTS

I would like to thank Dr. Eyad Masad for his generous advice, guidance, and help. For the past four years, he has been a well qualified advisor who has a brilliant way of thinking and addressing the suddenly arisen research issues. I will never forget his favors, advice, help, encouragement, and support that gave me support to earn this Ph.D. degree. It is because of my good fortune and my mother's and father's prayers for me that I was advised by a very nice, helpful, great, and gracious person, Dr. Eyad Masad.

I also would like to convey my special thanks to the distinguished professors, Dallas Little, Robert Lytton, Hamn-Ching Chen, and Charles Glover, for serving as valuable committee members and for their very kind advice and helpful ideas.

I would like to express my thanks to my friends, Dr. Ala Abbas at Turner-Fairbank Highway Research Center and Dr. Laith Tashman at Washington State University, for their great help in the image processing part of the dissertation. Special thanks are also due to Adhara Castelblanco, graduate student at the Civil Engineering Department at Texas A&M University, for her great help.

Special thanks go to all the faculty members and staff in the Civil Engineering Department at Texas A&M University and Texas Transportation Institute (TTI) for their

TABLE OF CONTENTS

LIST OF FIGURES

LIST OF TABLES

CHAPTER I

INTRODUCTION

Hot mix asphalt (HMA) is a porous material that has three components: asphalt, aggregates, and air voids. One of the primary factors controlling pavement performance is the ability of HMA to prevent water from remaining within the pavement system. Moisture-related damage can be caused by two primary mechanisms. The first mechanism is associated with the chemical interaction of water with asphalt and aggregates leading to the loss of cohesive bonding within the binder and loss of adhesive bonding between aggregates and binder (Little 2003; Kim et al. 2004; Lytton 2004). The second damage mechanism is the buildup of pore pressure due to the saturation of voids with water and the dynamic loading of traffic. Moisture damage leads to excessive deflection, cracking, permanent deformation, and reduction in the load carrying capacity of pavement (Lindly and Elsayed 1995).

The significant influence of water on pavement performance is described accurately by Cedergren (1974). He pointed out that the pavement systems that are not designed to prevent infiltration of water have the ingredients built in for self-destruction. He stated that: "When free water gets into the boundaries between structural layers, the multi-layered systems act very much as diaphragm pumps under the pounding of heavy wheel loads" (p.4). He gave examples of the pavement deterioration caused by each heavy-load

---

This dissertation follows the style and format of the *Journal of Computing in Civil Engineering*.

impact. It causes water to move at the interface between the base course and the wearing course. As a result, the material will be eroded and ejected through cracks and joints. Finally, these actions will produce channels and cavities that weaken the pavement, and the result could be a total failure of the pavement. Several reports by the Federal Highway Administration have emphasized that the existence of free water in the pavement system throughout most of the United States is a major factor contributing to damage in a majority of these pavements.

Problem Statement

Permeability of a porous material is defined as the ability of this material to transmit fluids through its voids when subjected to pressure or a difference in head. Permeability of HMA mixes is a function of the characteristics of the different mix constituents, mix compaction, and some geometrical properties of the pavement such as layer thickness. All these factors, however, affect permeability through altering the air void distribution in terms of size, connectivity, spatial distribution, and directional distribution. It has been reported that slight changes in HMA mix design can change permeability by orders of magnitude.

Understanding the mechanisms of moisture damage starts with developing experimental and analytical techniques to accurately assess the HMA permeability and its relationship to the mix constituents. This study is concerned with the development of the analytical methods to predict HMA permeability with the aid of microstructure analysis of air void

distribution using X-ray Computed Tomography (CT) and image analysis techniques. The directional and spatial distributions of HMA permeability are studied in this dissertation. In doing so, the effect of the permeability measurement methods and microstructure resolution on the permeability results is discussed.

The first contribution of this study is the development of empirical-analytical equations that relate permeability to the different properties of air void distribution, aggregates, and asphalt binder.

The second primary contribution of this study is the development of a program for numerical simulation model for fluid flow in HMA. The developed numerical solution uses the actual three dimensional microstructures that are captured using the X-ray CT. The numerical model also uses the non-staggered grid system to solve the Navier-Stokes equations including the nonlinear terms. The numerical model outputs include the values of the different elements of the symmetrical permeability tensor of the given microstructure and its anisotropy, and velocity and pressure distributions within this microstructure.

Objectives

The objectives of this study are summarized as follows:

a. Use X-ray CT and image analysis techniques to quantify the 3-D air void distribution and connectivity,

b. Characterize air void distribution as the main factor that controls permeability irrespective of the differences in the mix constituents that create the air void distribution,

c. Develop empirical-analytical equations that relate the HMA permeability to the properties of the constituents,

d. Develop a non-staggered finite difference numerical model for the simulation of the steady incompressible fluid flow in a 3-D microstructure of asphalt mixes by solving the governing equations: the continuity equation and the Navier-Stokes equations,

e. Validate the developed models through comparing their results with closed-form solutions,

f. Calculate the element of the permeability tensor using the developed numerical model and assess the permeability anisotropy, and

g. Compare the numerical permeability values to HMA permeability measurements.

Dissertation Outline

The style and format of the *Journal of Computing in Civil Engineering* was followed in writing this dissertation. The dissertation consists of six chapters. In Chapter I, an introduction to the dissertation is presented. The introduction includes the problem statement, the specific objectives of the research, and the dissertation outline.

Chapter II describes the literature review that is relevant to the subject. Factors affecting permeability of porous materials are discussed. Permeability models including the analytical, probabilistic, and numerical models are also presented. The different experimental methods for measuring permeability of HMA in the field or in the laboratory are reviewed.

Chapter III describes the X-ray CT, image processing techniques, and air void distribution analysis. The materials and HMA mixes that are used in this study are also included in this chapter.

In Chapter IV, two empirical-analytical approaches for predicting permeability based on air void distribution characteristics and HMA mix properties are presented. These approaches consider air void size, tortuosity, aggregate size, asphalt content, and degree of saturation in predicting permeability.

Chapter V includes the derivation of the numerical model for fluid flow simulation. The development of the model using the governing equations of the flow, numerical stability of the model, and verification of this simulation model using some idealized microstructures are also included in Chapter V.

In Chapter VI, the outputs of the numerical model are discussed. These outputs include the permeability tensor and the velocity and pressure distributions within the analyzed

HMA microstructures. Permeability results obtained numerically are also compared to the measured permeability of HMA mixes. The principal permeability and corresponding principal directions are also found. The anisotropy of permeability tensor is also studied in Chapter VI.

The last chapter, Chapter VII, is the dissertation summary that reviews the main tasks of this study and includes the dissertation conclusions and some recommendations for future work.

CHAPTER II

LITERATURE REVIEW

Introduction

This chapter presents a review of the literature pertinent to the topic of this dissertation on fluid flow in porous materials with emphasis on HMA. The basics that govern the permeability of porous media are discussed first. Then, a review of permeability models (analytical, probabilistic, morphological, and numerical models) is presented. Permeability measurement devices and methods are presented briefly to develop appreciation of the experimental factors that influence the ability to compare the permeability of different HMA mixes. Finally, recent studies on the permeability of HMA are summarized.

Factors Affecting Permeability of Porous Materials

Fluid flow can be classified into steady, transient, or turbulent flow depending on the flow velocity. The steady flow, often termed as laminar flow, is the flow with low velocity. At higher velocity, the steady flow becomes transient and then turbulent (Scheidegger 1974).

Fluid flow in porous media is driven by two different mechanisms. The first one is known as the creeping flow, which is due to the fluid viscosity. The second one is convection flow, which is due to the inertial forces. The significance of either one of

these terms depends on the value of the Reynolds number (Re), which combines fluid density (ρ), viscosity (μ), velocity of flow (v), and a characteristic dimension of porous media (l), Eq. (2.1) (Scheidegger 1974).

$$\text{Re} = v\rho l / \mu \tag{2.1}$$

For the same fluid and porous material, the velocity changes as a function of the applied pressure gradient in the direction of the flow as illustrated in Fig. 2.1. The linear part of the curve represents the region of small Re where creeping flow is the dominant mechanism.
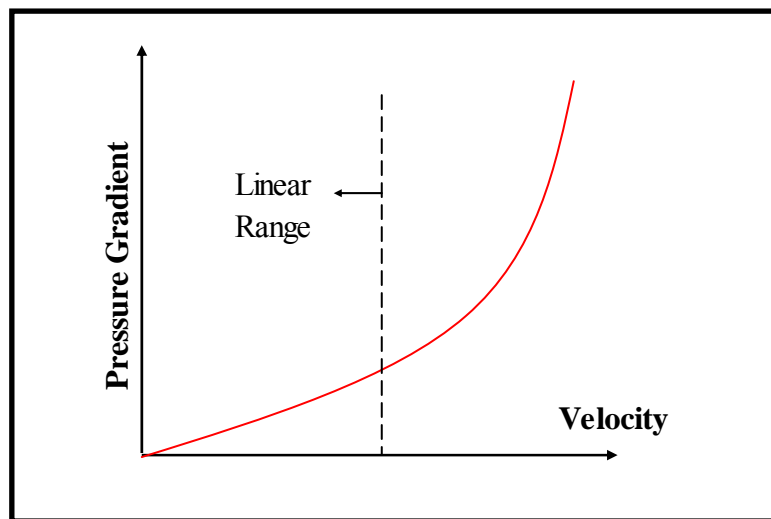
Fig. 2.1. Relationship between pressure gradient and velocity

Holtz and Kovacs (1981) pointed out that fluid flow in soils can be considered laminar flow in which the velocity (v) is proportional to the pressure gradient (i) as shown in Eq. (2.2). The proportionality coefficient in this equation (k) is the permeability coefficient.

$$v = ki \qquad (2.2)$$

Since fluid flow in porous materials is considered as laminar flow, then, permeability of most porous materials is usually calculated based on assuming small Re in the linear range of the curve shown in Fig. 2.1. This assumption has been verified in numerical simulations of fluid flow in the internal structure of porous media such as sandstone, cement paste, and sands (Adler et al. 1990; Martys et al. 1994; Masad et al. 2000).

Eq. (2.2) was developed originally based on the work by the French engineer Darcy. Darcy (1856) showed experimentally that the flow rate (q) in units of volume per unit time through a cross-sectional area (A) is proportional to the pressure gradient (i), Eq. (2.3). Fig. 2.2 shows a schematic diagram for the experiment done by Darcy (1856). Using this diagram, the pressure gradient (i) is defined as the pressure difference (Δh) divided by the specimen length (l). Permeability coefficient (k) is then expressed in velocity units for a given hydraulic head.

$$q = kiA \qquad (2.3)$$
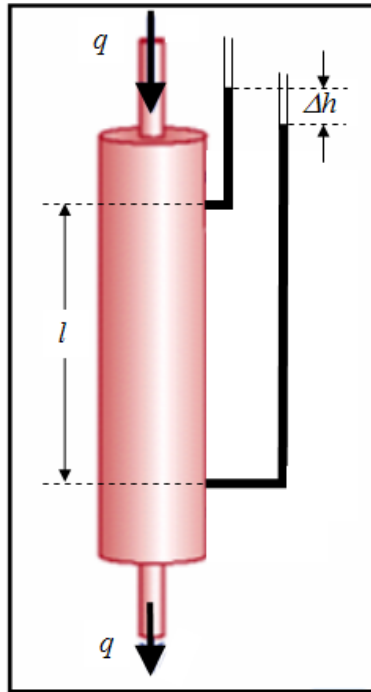
Fig. 2.2. A schematic diagram of Darcy's experiment

Because the fluid flow average velocity is simply the flow rate (q) divided by the cross-sectional area (A), Eqs. (2.2) and (2.3) are identical. Eq. (2.4) presents the differential multidimensional form of Darcy's law (Dullien 1979) in which $\vec{V}$ is the average velocity vector within a specimen, μ is the viscosity coefficient, $\vec{\nabla}P$ is the pressure gradient, and K is Darcy's symmetric absolute permeability tensor.

$$\vec{V} = -\frac{1}{\mu}K \cdot \vec{\nabla}P \tag{2.4}$$

A component (K) of the absolute permeability tensor has area units and is related to Darcy's permeability coefficient (k) with velocity units by the relationship in Eq. (2.5), where γ is the unit weight of the fluid.

$$k = K \frac{\gamma}{\mu} \qquad (2.5)$$

It can be seen from Eq. (2.5) and as reported by Scheidegger (1974) that permeability of porous materials depends on the properties of the porous material and the permeative fluid. The properties of the porous material are presented by the absolute permeability (K) which is a function of the porous material only. The properties of the permeative fluid are presented, on the other hand, by its unit weight and viscosity. As Dullien (1979) pointed out, it is more scientific and more useful to separate the contribution of porous material from that of the permeative fluid.

Since permeability of porous materials depends on the properties of the fluid and those of the porous material, permeability will be affected by any changes in their properties. The viscosity and the unit weight of the permeative fluid are mainly affected by temperature. The porous material, on the other hand, is changed whenever the properties of its constituents are changed.

The effective grain size, air void (pore) size, shapes of air voids and flow paths, and the material's degree of saturation were mentioned by Holtz and Kovacs (1981) as some of

the factors that affect permeability of porous materials. The same factors were listed by Scheidegger (1974), who also pointed out that the effect of these factors on permeability cannot be represented by simple correlations. He also referred to some studies that tried to relate permeability of porous materials to grain angularity or roundness, grains orientation, and specific surface area. Several studies can be found in the literature on relating permeability to the characteristics of porous media such as rocks, clays, concrete, and asphalt (Soonswang et al. 1991; Huang et al. 1999; Shackelford et al. 2000; Shang et al. 2003; Mohammad et al. 2003).

For HMA mixes, the permeability and the factors affecting the permeability of these mixes should be determined in order to control water infiltration to asphalt pavements. Permeability of HMA, as in the case of any other porous material, depends on the properties and proportions of its constituents: aggregates, asphalt, and air voids. The aggregates and air voids can have different sizes, shapes, and distributions. The different characteristics of aggregates and air voids can be considered as the key factor affecting fluid flow in HMA pavements. Specimen thickness and compaction procedures are other possible factors affecting the permeability of asphalt mixes.

Several studies have shown that the permeability of asphalt mixes is a function of percent air voids, size and number of air voids, aggregate gradation, aggregate shape, specimen thickness, and compaction procedures (Zube 1962; Hudson and Davis 1965; Cecheitini 1974; Ford and McWilliams 1988; Brown et al. 1989; Choubane et al. 1998;

Cooley 1999; Huang et al. 1999; Cooley and Brown 2000; Cooley et al. 2001; Kanitpong et al. 2001; Kandhal and Mallick 2001; Mallick et al. 2001; Maupin 2001; Cooley et al. 2002a; Christensen and Bonaquist 2003; Mohammad et al. 2003).

Zube (1962) and later Brown et al. (1989) indicated that dense-graded pavements become excessively permeable at in-place air voids above 8%. However, a study conducted by the Florida Department of Transportation (Florida DOT) indicated that coarse-graded Superpave mixes could be excessively permeable to water at in-place air voids less than 8% (Choubane et al. 1998).

Mohammad et al. (2003) had related the permeability of Superpave asphalt mixtures to different factors including air void content, compaction effort, mix gradation, and lift thickness. They found that air void content and aggregate gradation have significant effects on permeability of Superpave mixes. Generally, they reported that fine-graded Superpave mixes are not permeable. On the other hand, coarse-graded mixes with air void content that is more than 5.3% are found to be permeable. A general trend of lower permeability for lift thickness that is higher than 6 cm was predicted.

Effect of density, nominal maximum aggregate size (NMAS), and lift thickness on permeability of coarse-graded Superpave mixes was studied by Cooley et al. (2002a). In their study, they concluded that either field or laboratory permeability is affected by the density of the coarse-graded Superpave mixes: as density increases, permeability

decreases. Mixes with aggregates NMAS of 9.5 and 12.5 mm were found to have similar permeability characteristics, but in general and at the same percent air voids level, mixes with high NMAS have more potential for higher permeability. They also reported that as the lift thickness increases permeability decreases.

Another study by Christensen and Bonaquist (2003) related permeability to aggregate size and void and asphalt contents. They found that permeability decreased with increasing voids filled with asphalt and increasing aggregate fineness. Prowell and Dudley (2002) showed that both field and laboratory measurements of permeability were correlated with pavement density. All the HMA studies mentioned above showed that several factors have effects to different extents on permeability. However, none of these studies had developed methods or analytical relations to predict permeability.

Permeability Models

This section provides a brief review of the different permeability models. These permeability models are categorized as analytical, probabilistic, morphological analysis, and numerical models (Masad 1998).

Analytical Models

Most methods relate permeability of porous materials to some measures of air voids. Bear (1972) had provided a group of models that have been used to represent flow

through porous media. These models were summarized by Rajani (1988) as shown in Table 2.1.

Table 2.1. Description of Some of the Permeability Models

Model	Permeability	Constants	Comments
Fissure	$K = Cn_a b^2$	C=1/12 for parallel fissures of width b	Applicable to fissured rock
Capillary Tubes	$K = Cn_a \delta^2$	C=1/32 for tube in 1-D C=1/96 for tube in 3-D	Based on Haggen-Poiseulle's law
	$K = Cn_a \int_0^\delta \delta^2 \alpha(\delta) d\delta$	C=1/96 for capillarity in orthogonal directions	Assume 1/3 of the tubes are in each mutually orthogonal direction
Resistance to Flow	$K = \dfrac{Cn_a^2 D_s^2}{\lambda(1-n_a)}$	Factor of packing, λ=3π for single sphere in infinite fluid; C=π/6 for spherical particles	Based on Stokes' equations for drag
Hydraulic Radius	$K = \dfrac{Cn_a^3 D_s^2}{(1-n_a)^2}$	C=1/180 for spherical particles	Kozeny-Carman equation. Based on the idea of hydraulic radius.

n_a = porosity (percent air voids), δ = air void diameter, $\alpha(\delta)$= fraction of air void diameter δ, D_s = average particle size.

Although the models shown in Table 2.1 are derived based on entirely different assumptions, they can all be expressed in the following unified form (Bear 1972; Masad 1998):

$$K = f(n) \cdot C \cdot D_s^2 \qquad (2.6)$$

where $f(n)$ is a function of percent air voids or porosity; n, of the porous medium, C is a factor that accounts for the distribution of air voids, and D_s is the average size of the particles. Common to most of the available models represented by Eq. (2.6) is the simplified assumptions on the shape of air voids and the distributions of solids and voids. These assumptions allow the models to describe the internal structure by average parameters such as percent air voids, average particle size, and specific surface area. However, since HMA mixes include a wide range of aggregate sizes compared to other porous media such as soils and rocks, it would be difficult to represent the effect of gradation by one particle size.

Probabilistic Models

In addition to the analytical permeability models, probabilistic-based flow models constitute another family of permeability models. The most popular probabilistic model is the one proposed by Childs and Collis-George (1950) and later modified by Marshall (1958). Masad (1998) had elaborated and explained the model by Childs and Collis-George (1950). Millington and Quirk (1959), Mualem (1976), Garcia-Bengochea (1978), Juang and Holtz (1986), and Taylor et al. (1990) had developed different probabilistic models based on different assumptions in regard to the probability of air voids being connected. In general, these probabilistic models utilize elaborate procedures to describe the distribution of air voids in porous materials. They, however, employ simplified assumptions on the probabilistic distribution of air voids and their connectivity.

Morphological Analysis Models

Permeability models based on morphological analysis of the microscopic geometry of air voids are also presented in the literature (e.g., Koplic et al. 1984 and Lock et al. 2002). They constructed an equivalent random network of cylinders or tubes to model the microstructure based on the microscopic geometry of air voids. This approach requires laborious experimental procedures that might alter the air void distribution. The results gave permeability coefficients that were too high and differed by a factor of 10 from actual measurements. Blair et al. (1996) analyzed images of porous media captured using a scanning electron microscope (SEM) to determine the material porosity, specific surface area, and grain and pore sizes. These quantities were used in a modified Kozeny-Carman equation to predict permeability. Arns et al. (2001) discussed the effects of experimental factors such as image size and image resolution on the calculated microscopic properties.

Numerical Models

A number of recent studies attempted to calculate the permeability of porous materials by solving the fluid flow equations numerically. These equations govern the fluid flow in the porous material and include the continuity equation and the momentum (Navier-Stokes) equations. These governing equations are generally represented in their differential forms. They are nonlinear equations that can be solved using the computational fluid mechanics (Roberson and Crowe 1997). The principle of the

computational fluid mechanics is the representation of these governing equations in algebraic forms that can be solved suitably using different mathematical techniques.

In the simulation of fluid flow in porous materials, the numerical studies had considered different fluid flow types that, generally, range from the simple unidirectional flow to more complicated flows such as the two-dimensional (2-D) and three-dimensional (3-D) fluid flows. Some of these numerical studies used artificial microstructures in representing the porous material while other studies used the actual microstructure of the porous material with no presumptive or deductive assumptions. Different computational techniques were used in simulating fluid flow in porous materials, among which are the finite difference and finite element techniques.

Adler et al. (1990) and Martys et al. (1994) generated isotropic artificial media and solved the Stokes equations in that media assuming Newtonian fluids with low Re fluid flow. Stokes equations differ from the full set of Navier-Stokes equations in that Stokes equations govern only the creeping fluid flow that has low Re and negligible inertial forces.

In the finite difference approach, the differentials in these governing equations are first represented by finite differences and then the whole differential equations are converted to algebraic equations (Roberson and Crowe 1997). These algebraic equations are solved

iteratively, and the average velocity components are obtained. The average velocity components are then used to solve for the permeability using Darcy's law: Eq. (2.4).

Masad et al. (2000) and Tashman et al. (2003) used the finite difference technique in solving the full Navier-Stokes equations in 2-D anisotropic microstructure of soils specimens. These numerical models account for the effect of the microstructure of the porous media directly and without the need to characterize the complex microstructure.

In numerical models, either a staggered or non-staggered scheme can be used to solve the governing equations of fluid flow. The non-staggered grid scheme uses one computational cell while the staggered scheme uses two different computational cells in solving the governing equations of the fluid flow; one cell is used in solving the continuity equation, and the other is used in solving the momentum equations. The staggered grid scheme was used by Adler et al. (1990), Martys et al. (1994), Masad (1998), Masad et al. (2000), and Masad et al. (2002b). The non-staggered grid scheme, on the other hand, was proposed by Rhie and Chow (1983) and Peric (1985). Tashman et al. (2003) used the non-staggered grid scheme in simulating fluid flow in 2-D granular microstructures where only one cell is needed to solve for the continuity and Navier-Stokes equations.

In addition to the finite difference technique, other computational techniques were used by Wang et al. (2003a) and Pilotti (2003). Wang et al. (2003a) used the finite element

method (FEM) to solve for fluid flow in porous media. They proposed using homogenization theory to model fluid flow in porous media. Their analysis used two levels of flows; one is at the pore level, and the other is at the macro level. The governing equations for both levels were derived from Navier-Stokes equations at low Re. Pilotti (2003) used the Lattice Boltzmann technique to solve Navier-Stokes equations in reconstructed or artificial 3-D microstructures. He showed that the Lattice Boltzmann is capable of solving Navier-Stokes equation once there is a comprehensive description of the hydrodynamics of fluid flow with a low Re. Both of these studies (Wang et al. 2003a; Pilotti 2003) used some idealized 2-D and 3-D microstructures to simulate real porous microstructures.

Permeability Measurement Methods

Permeability of asphalt mixes and other porous materials such as soil samples can be measured either in-situ or in laboratory. Different field permeameters have been used in measuring in-situ HMA permeability (Cooley 1999). The main advantage of the field permeameters is that the test is nondestructive. Their shortcomings can be summarized as: the ability of fluid to flow in any direction, the inaccurate determination of degree of saturation, the inability of thickness and area to be determined exactly, and the inability of number of layers in which fluid flows to be determined (Cooley 1999). Four in-situ permeameters are evaluated in Cooley (1999). An example of one of these field permeameters is presented in Fig. 2.3, which is a three-tier setup comprised of different

sizes of graduated cylinders used by the National Center for Asphalt Technology (NCAT) (Cooley et al. 2001).

Fig. 2.3. Three-tier field permeameter (after Allen et al. 2001)

Experimental setups have been developed for measuring HMA permeability in the laboratory. Laboratory setups overcome some of the previous shortcomings of the field permeability testing setups. Consistent degree of saturation can be assured during the laboratory permeability test, and the dimensions of a test specimen are available for calculations. Laboratory setups have been developed to measure the vertical and/or horizontal permeability. Vertical permeability can be measured using two setups: the falling-head and constant-head setups, as presented by Lindly and Elsayed (1995), Richardson (1995), Fwa et al. (1998), Choubane et al. (1998), and Huang et al. (1999).
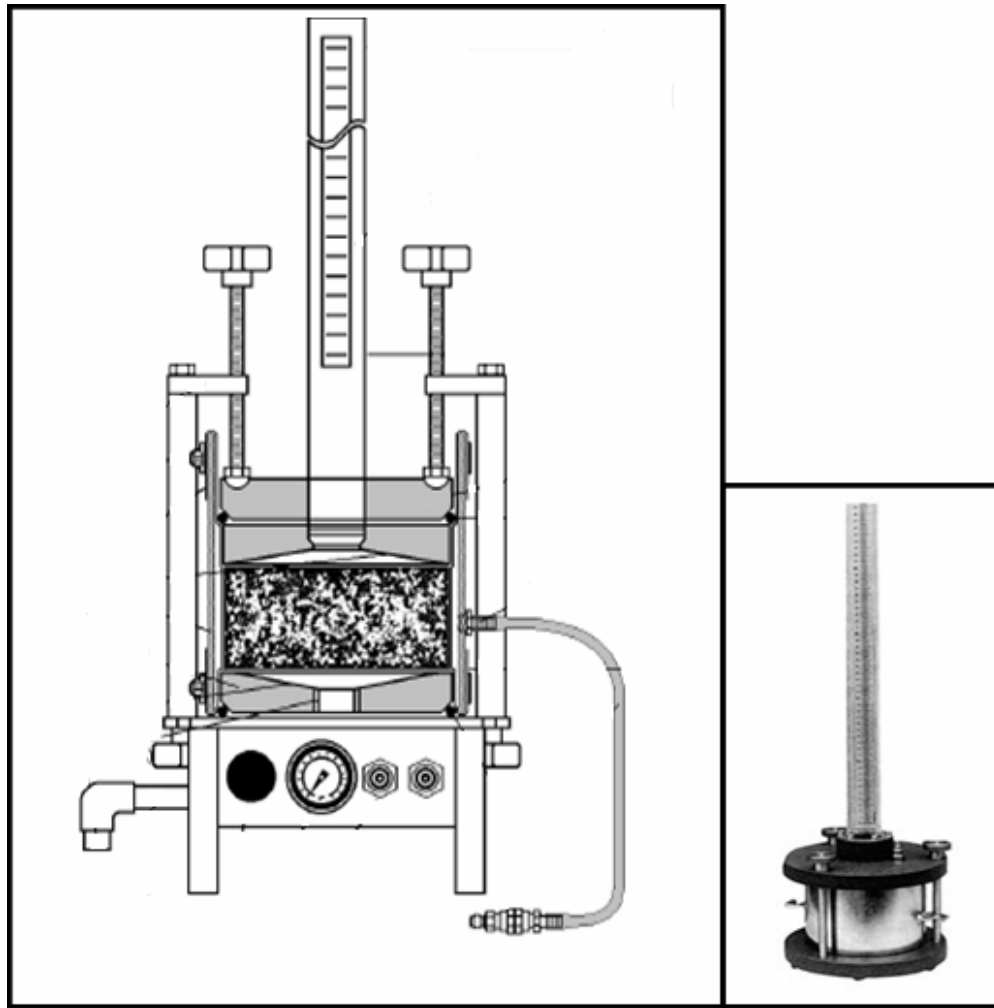
Fig. 2.4. Falling-head laboratory permeameter

These setups differ mainly in type of head difference applied during testing (constant-head vs. falling-head), method by which the hydraulic head difference is measured during the test, and the use of flexible triaxial compression chamber (ASTM D5084-90 1999) or rigid wall permeameter (ASTM D2434-68 2000). Fig. 2.4 shows an example of the falling-head permeameters; it is the device manufactured by Karol-

Warner Company (ASTM PS129 2001). An example of the constant-head permeameter is shown in Fig. 2.5.

Choubane et al. (1998) and Maupin (2001) presented a device that consists of a metal cylinder with a flexible membrane on the inside of the cylinder where air pressure can be applied. In this device, the circumference of a specimen is coated with a layer of petroleum jelly to prevent the flow of water along its surface before it is placed in the metal cylinder.

(a) Permeability Cell   (b) Pressure Control Panel

Fig. 2.5. Constant-head laboratory permeameter

Huang et al. (1999) have presented a dual mode apparatus that allows for either falling-head or constant-head permeability. The dual mode apparatus enables switching of test mode from falling-head to constant-head or vice versa without disturbing the test material. This setup was used in measuring hydraulic conductivity of different materials from dense-graded low permeable mixtures to open-graded drainable mixtures under both constant-head and falling-head modes (Huang et al. 1999; Fwa et al. 1998).

Kanitpong et al. (2001) used the flexible-wall permeameter (ASTM D5084-90 1999) in measuring permeability of laboratory-compacted asphalt mixes. This setup allows verifying the specimen saturation, which is an important factor that influences the measured permeability values. In order to decrease the leakage along the specimen surface, Kanitpong et al. (2001) applied a thin layer of bentonite paste along the sides of the specimen to fill voids and provide a smooth surface for the membrane to contract.

Laboratory setups for measuring horizontal permeability of granular materials have been developed by Wit (1966), Latini (1967), Moore (1979), and Pare et al. (1982). The quality of the results given by these permeameters is limited by at least one of the following factors: porous stones much smaller than the sample, lateral leakage, and a lack of real control of the saturation degree. Chapuis et al. (1989) have designed an apparatus (Fig. 2.6) that overcomes most of these limitations. It has design details similar to those described in (ASTM D2434-68 2000) except for the fact the permeameter is horizontal instead of vertical. In order to avoid lateral leakage, a water

pressure is applied against a flexible membrane along the walls of the permeameter (Chapuis et al. 1989).
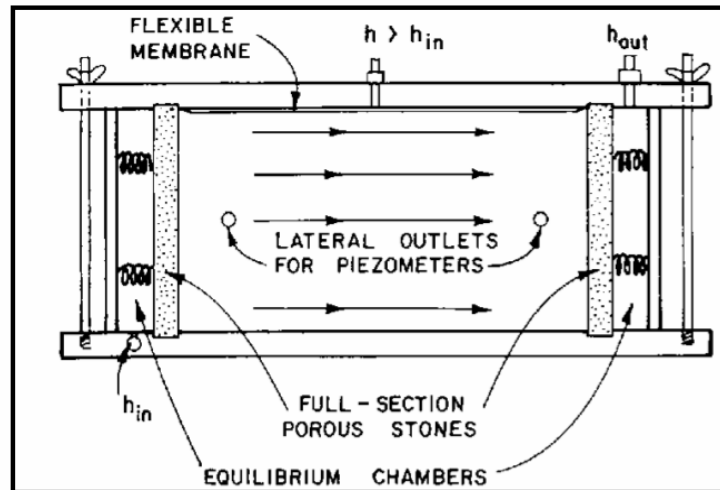
Fig. 2.6. Cross section of the horizontal permeameter for granular material (after Chapuis et al. 1989)

HMA Permeability Models

Most of the previous studies focused on developing empirical relationships that relate HMA permeability to percent air voids only. Figs. 2.7, 2.8, 2.9, and 2.10 show some relationships between permeability of different types of HMA mixes and percent air voids in these mixes.
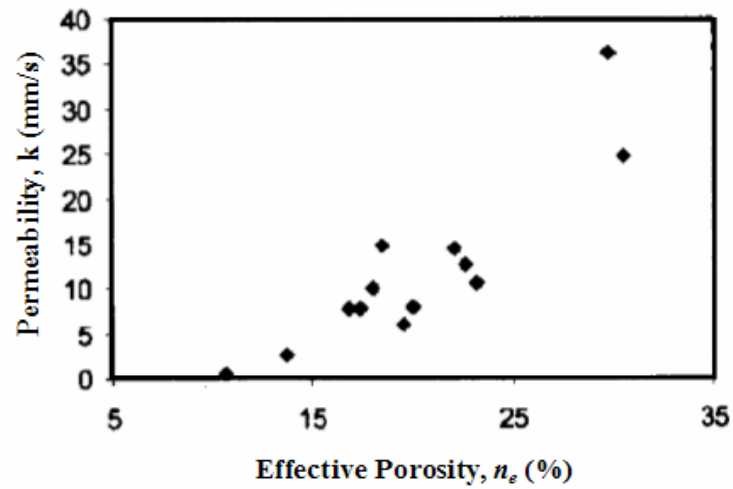
Fig. 2.7. Permeability as a function of the effective porosity (after Huang et al. 1999)
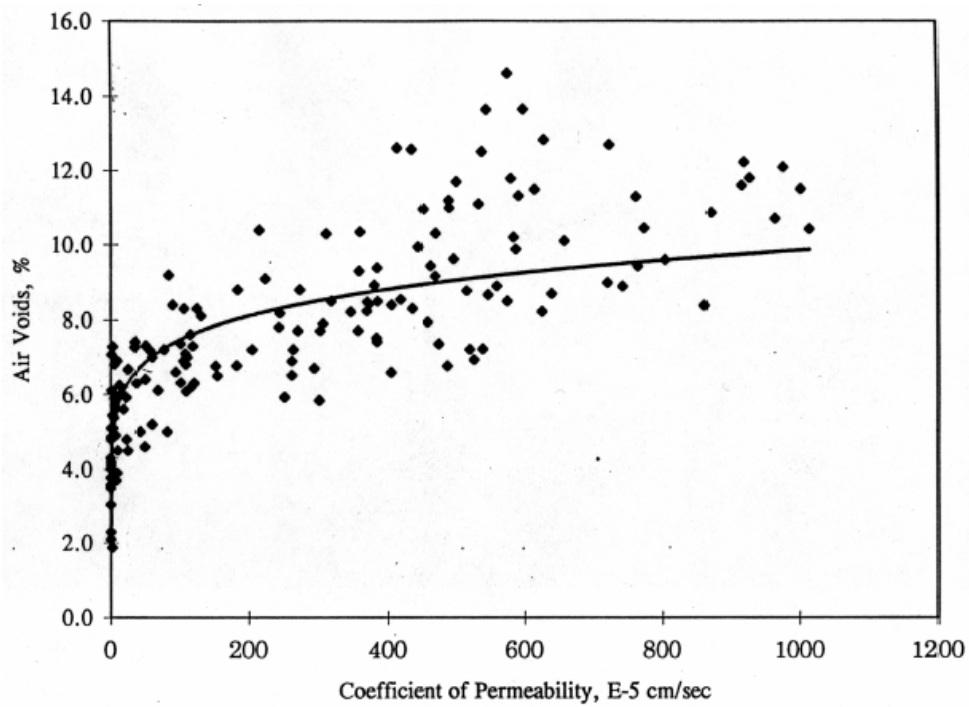
Fig. 2.8. Permeability-air void content (%) relationship (after Choubane et al. 1998)
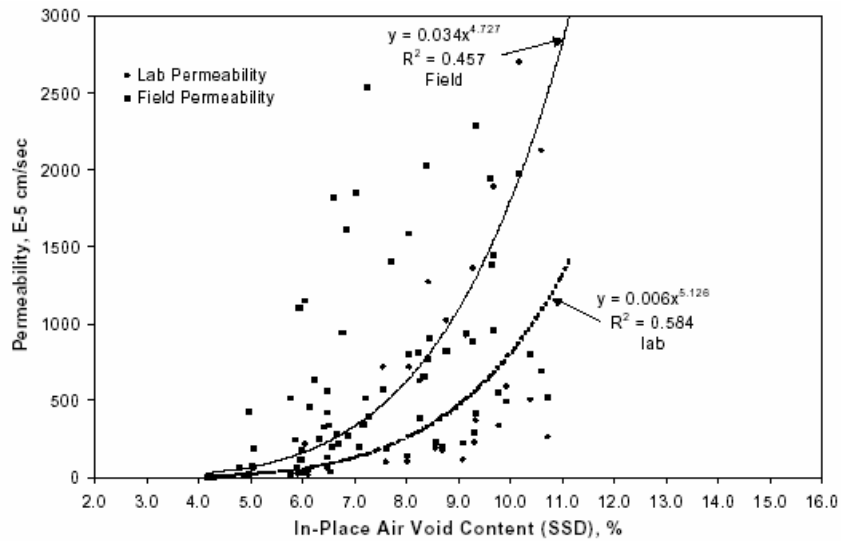
Fig. 2.9. Relationship between permeability and in-place air void content for mixes with 19.0 mm NMAS (after Cooley et al. 2002a)
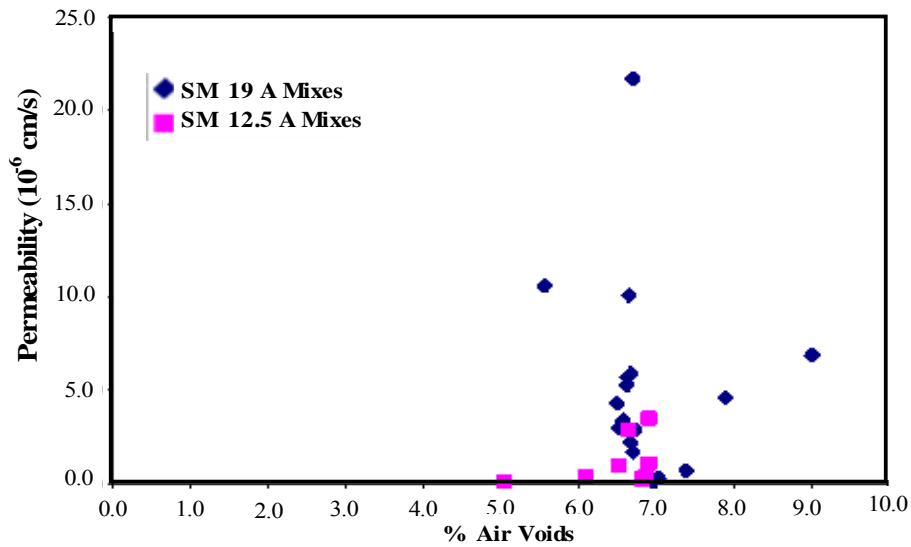
Fig. 2.10. Relationship between permeability and percent air voids (after Gogula et al. 2003)

Most of previous studies showed the general trend of higher permeability for mixes with higher percent air voids. However, one can easily see the large scatter in the data around the developed regression models. This is expected given the wide range of distributions of air void connectivity and sizes in HMA mixes that influence the measured permeability. The high variability in permeability measurements led Gogula et al. (2003) in their study on Superpave pavements to believe that there were no meaningful correlations between permeability and percent air voids. Fig. 2.10 shows their results for two mixes with 12.5 and 19.0 mm NMAS.

A critical review of the experimental permeability measurements conducted using different devices indicated clearly that the measurement method plays a very important role in determining permeability. As discussed earlier, these devices differ in their control on specimen saturation and control of water leakage around a specimen. Obviously, these differences make it difficult to develop an analytical equation for permeability without an empirical coefficient that depends on the measuring device.

Summary

This chapter discussed the literature review relevant to fluid flow in porous materials and HMA in particular. This review reveals clearly that there is a need to develop equations that relate HMA permeability to mix properties more than percent air voids. These properties should be related to the size and distribution of air voids. Consequently, the subsequent chapter of this dissertation includes the development of empirical-analytical

equations that rely on quantifying the air void distribution using image analysis techniques and the nondestructive X-ray CT imaging technique.

In addition, the numerical models available in the literature have either assumed creeping flow only in porous media and/or used computer-reconstructed microstructures rather than the actual material microstructure. In this study, a numerical model that accounts for both the creeping flow and convective flow in 3-D images of HMA microstructure is developed.

CHAPTER III

X-RAY COMPUTED TOMOGRAPHY, IMAGE PROCESSING, AND

EXPERIMENTAL PLAN

Introduction

This chapter discusses X-ray computed tomography (CT) and the image processing techniques that were used in characterizing the HMA microstructures. First, the X-ray CT system is described. Then, the use of this system and image analysis techniques in analyzing air void structures is discussed. This is followed by a description of the asphalt mixes that will be used throughout the rest of the dissertation. These asphalt mixes include HMA mixes that were scanned using the X-ray CT system and a database of asphalt mixes with their measured permeability. This database was gathered from a number of studies on the permeability of HMA.

X-Ray Computed Tomography and Image Processing

Most of the studies on HMA permeability have focused on relating permeability to the total air void percentage. However, microstructure characteristics such as the size, distribution, and connectivity of air voids are key factors that must be considered in addition to the total volume of voids. Limited efforts have been directed at considering these microstructure characteristics due to the lack of experimental techniques to capture them. Recently, advances in nondestructive evaluation and imaging techniques have lead to the development of X-ray CT for visualizing features in the interior of opaque solid

objects to obtain digital information on their 3-D geometry and properties (Flannery et al. 1987; Dennis 1989).

The power of the X-ray CT is that it is a nondestructive technique that is not restricted by the shape or the composition of the material under consideration. Masad (2004) provided a summary of the applications of X-ray CT in civil engineering in general and in the characterization of asphalt mixes and aggregates in particular. X-ray CT has been widely used in engineering as an effective tool in characterizing material microstructures. Petrovic et al. (1982), for example, used the X-ray CT in studying the spatial distribution of soil density. X-ray CT was also used by Hainsworth and Aylmore (1983) in studying soil water content. Several studies had used X-ray CT in characterizing the void distribution and damage of asphalt mixes. Some of these studies are Synolakis et al. (1996), Shashidhar (1999), Masad et al. (1999a), Wang et al. (2001), Masad et al. (2002a), Wang et al. (2003b), and Tashman et al. (2004).

Some of the other applications of the X-ray CT include studying the relationship between the asphalt mix sample size and its global properties (Romero and Masad 2001), quantifying damage in asphalt mixes (Braz et al. 1999; Tashman et al. 2004), and analyzing fluid transport in porous media (Auzerais et al. 1995). The above and other applications for the use of X-ray CT technique are found in Masad (2004).
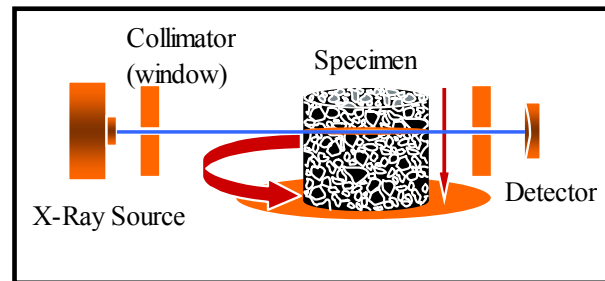
Fig. 3.1. Components of X-ray CT system

Description of the X-Ray Computed Tomography System

Fig. 3.1 shows the X-ray CT system, which consists of an X-ray source and a detector with a test specimen placed in between. The source generates X-ray radiation with certain intensity. Part of the radiation, when X-rays penetrate through a specimen, will be either absorbed or scattered. The remaining part, on the other hand, will penetrate through the specimen. The intensities of these transmitted X-rays are recorded with detectors placed at the other side of the specimen.

The linear attenuation coefficient (μ) is a property of the material occupying each point within the test specimen, and the amount of radiation energy scattered and absorbed at each point is a function of μ. Computed tomography deals with the determination of the X-ray intensities through the determination of the value of μ at all the points. The linear attenuation coefficient (μ) at each point depends directly on the density of the specimen at that point; therefore, it is feasible to distinguish the different features within the specimen.

The test specimen is scanned using the X-ray CT system via different scanning mechanisms (ASTM E1441 2003), among which are the parallel beam translate/rotate, the narrow fan beam translate/rotate, the wide fan beam rotate/rotate, and the inverted fan beam rotate/stationary scanning mechanisms (Masad 2004). The result of the scanning process is group of 2-D images which can be then stacked to form the 3-D specimen microstructure. In each scanning mechanism, there is a vertical shift between successive scans which determines the vertical resolution in the final 3-D microstructure. Another scanning mechanism is the cone beam in which the collimator is removed and the source transmits X-rays with a cone shape as the specimen is rotated. This scanning mechanism is faster than the fan beam. Though, the algorithm for the reconstruction of the 3-D microstructure is time-consuming and computationally expensive (Grangeat 1991).

The X-ray CT images presented in this dissertation are all scanned using the wide fan beam rotate/rotate scanning mechanism. The outcome of the scanning process is horizontal slices of 1.0 mm thickness that were captured every 0.8 mm of the specimen total thickness. These images were saved in tagged image file (TIF) format. Fig. 3.2 shows an example of X-ray CT image of an asphalt concrete specimen with a diameter of 150 mm. The captured image consists of 256 levels of gray intensity that correspond to different densities within the specimen. Air voids (low density) are presented by the darker spots, whereas the high density constituents (aggregates and asphalt binder) are presented by the brighter spots.
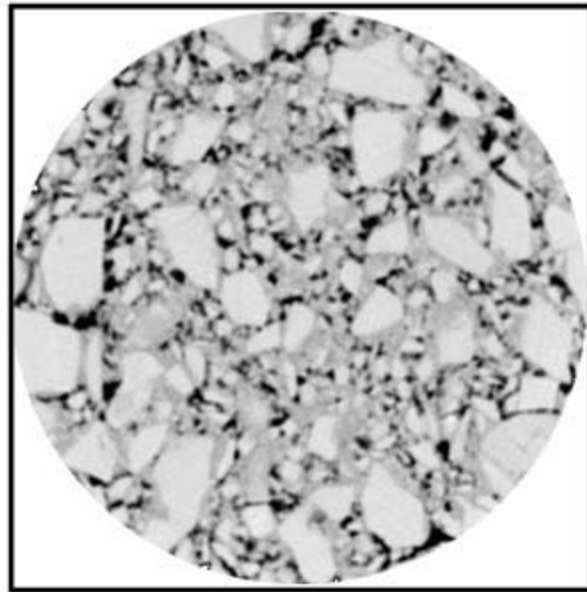
Fig. 3.2. Horizontal X-ray CT image of an asphalt concrete specimen

Image Processing of X-Ray CT Scanned Images

Air voids are the part of the microstructure through which fluid is allowed to flow. Therefore, the scanned gray images are processed in order to identify air voids from the other material constituents. Once air voids are identified, the air void distribution within the 3-D microstructure can be analyzed.

The gray scale images were transformed to binary images of white and black phases that correspond to the solids and air voids, respectively. The transformation was accomplished by choosing a threshold value for the intensity to identify the air voids from the other solid parts of the microstructure. The gray intensity measured on a given point may be higher or lower than this threshold value. Using this threshold value, the

original image is transformed to a binary image of black (air voids) and white (solid) phases.

Fig. 3.3. Corelok device (after Cooley et al. 2002b)

The threshold value was selected based on visual evaluation of the images and matching the percent air voids measured using the Corelok device (Fig. 3.3). The Corelok measurements were favored over the American Association of State Highway and Transportation Officials AASHTO T-166 (2000) because of the inaccuracy of the AASHTO T-166 (2000) measurements at high void contents.
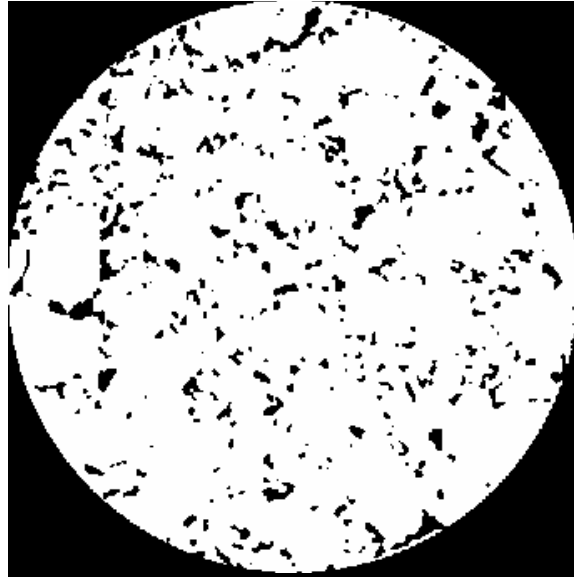
Fig. 3.4. X-ray CT image in Fig. 3.2 thresholded to isolate air voids (black) from solids (white)

Image thresholding and analysis was conducted using standard image analysis techniques available in Image Pro-Plus (Image-Pro Plus 1999). An example of a thresholded image is shown in Fig. 3.4. An IPBasic macro was written to facilitate and expedite the analysis. IPBasic is a built-in language in Image-Pro Plus, which is a sub-programming language of Visual Basic. The macro is able to identify air voids by recognizing the pixels that have density values less than the specified threshold value. It is also able to identify each single air void as a separate object on this image by recognizing the pixels that belong to the same air void. Fig. 3.5 shows the gray X-ray CT scanned image shown in Fig. 3.4 with the air void objects identified and enclosed by yellow boundaries.
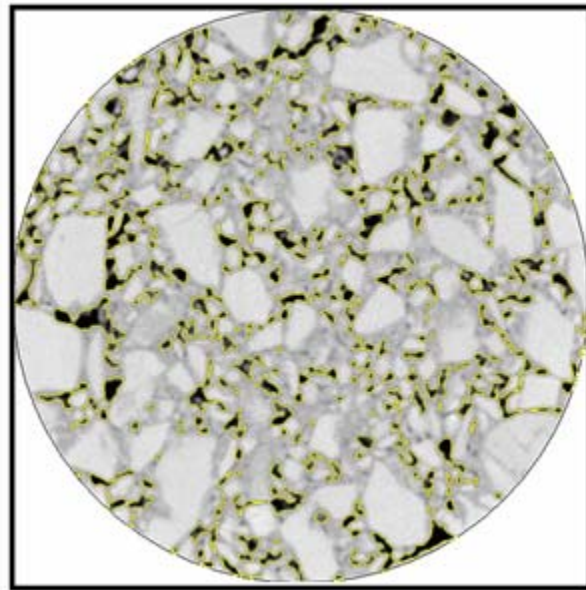
Fig. 3.5. Identifying air void objects on the gray X-ray CT image shown in Fig. 3.2 using

a specified threshold density value
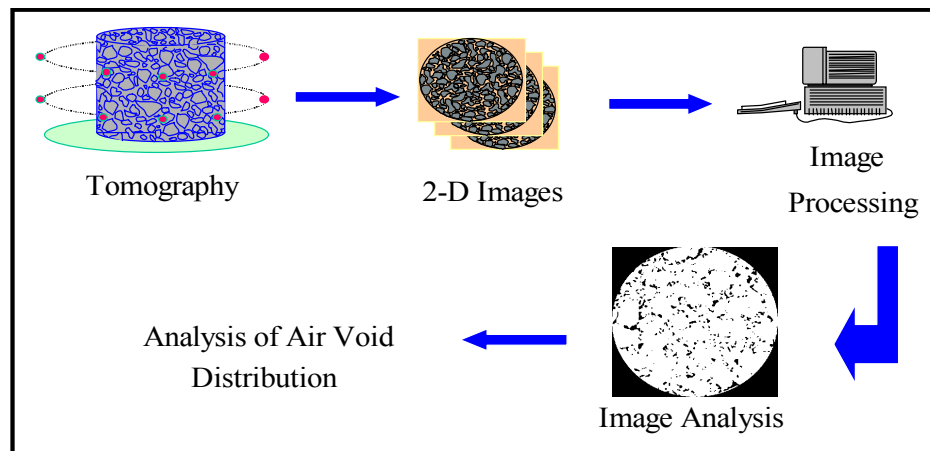
Fig. 3.6. Schematic diagram of CT and image analysis systems

This macro is also capable of loading all images that belong to the same specimen and analyzing several attributes such as area, perimeter, and dimensions of air voids. Fig. 3.6 summarizes the different stages that the images go through starting from scanning using the X-ray CT system to image analysis.

The processed images can be stacked together to form the actual 3-D microstructure. Cubical sections of the 3-D microstructure similar to the ones shown in Fig. 3.7 are used in the numerical simulations of fluid flow presented in Chapters V and VI of this dissertation.

Analysis of Air Void Structure

Different air void characteristics were calculated using the IPBasic macro presented above. These characteristics are the total percent air voids (n), specific surface area of air voids (S), location of connected air voids, and effective percent air voids (n_{eff}). The effective percent of air voids refers to those voids that are connected between the two ends of a specimen.

Percent of total air voids (n) of a specimen was estimated by calculating the average of the ratio of the area of voids (A_v) to the total area of each image (A_T) along the depth of a specimen presented by the number of images (N). Eq. (3.1) gives the equation used to calculate the percent total air voids.

$$n = \frac{\sum\limits_{i=1}^{N} \dfrac{(A_v)_i}{A_T}}{N} \qquad (3.1)$$

(a)

(b)
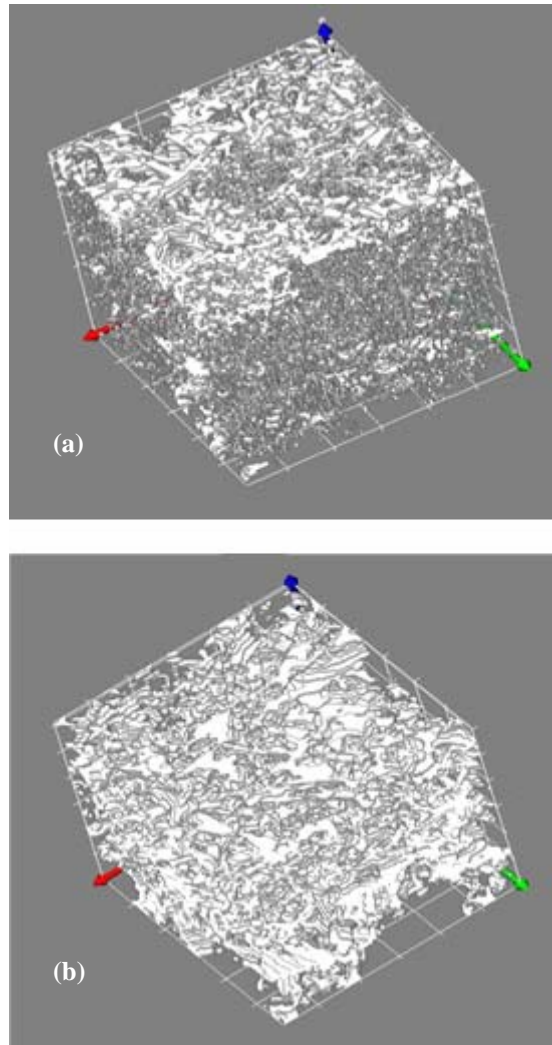
Fig. 3.7. An example of two different assembled 3-D microstructures: (a) Specimen with low porosity of 0.055 and (b) Specimen with high porosity of 0.174

Specific surface area (S) is defined as the ratio of the total surface area of the void-solid phase interface to the total volume of porous material. It was quantified by calculating the ratio of the wetted area of air voids to the specimen volume. The wetted area was measured as the perimeter of each air void multiplied by its thickness, which was 0.8 mm for all X-ray CT images. Since the thickness was constant for all images, surface area can be calculated as given in Eq. (3.2), where P_{ij} is the perimeter of an air void, M is the number of air voids on an image, and N is the number of images captured on a specimen.

$$S = \frac{\sum\limits_{i=1}^{N}\sum\limits_{j=1}^{M} P_{ij}}{A_T \times N} \qquad (3.2)$$

Air void connectivity is a 3-D property that involves working with all images captured in a specimen at the same time. It also requires keeping track of all connected voids and neglecting those that were not connected from the top to the bottom of a specimen. Another image analysis macro was developed to analyze air void connectivity. The method works by comparing the location of air voids on an image with those present on the image underneath it. If any two voids have partial or total overlap (connected), they are preserved, and their size and coordinates are stored. This process continues until all voids that are connected from the top surface to the bottom surface are quantified. Percent connected air voids (n_{eff}) is then defined as the ratio of the volume of the connected air voids to the total volume of the specimen. Voids that are not connected to the top and bottom surfaces are deleted. The macro was developed to capture any multiple overlapping

of air voids that might occur. Once the connected air voids are identified, the flow paths are also recognized and their lengths are calculated. Tortuosity (T), which is defined as the ratio of the length of a true flow path for a fluid to the straight line distance between inflow and outflow, can also be calculated.

The connectivity macro analyzes all the slices in one step, which makes the analysis very rapid. For example, it takes about one minute to analyze the connectivity in a specimen of 100 mm thickness. Fig. 3.8 illustrates the methodology used in analyzing air void connectivity by calculating the corresponding n_{eff} and T.
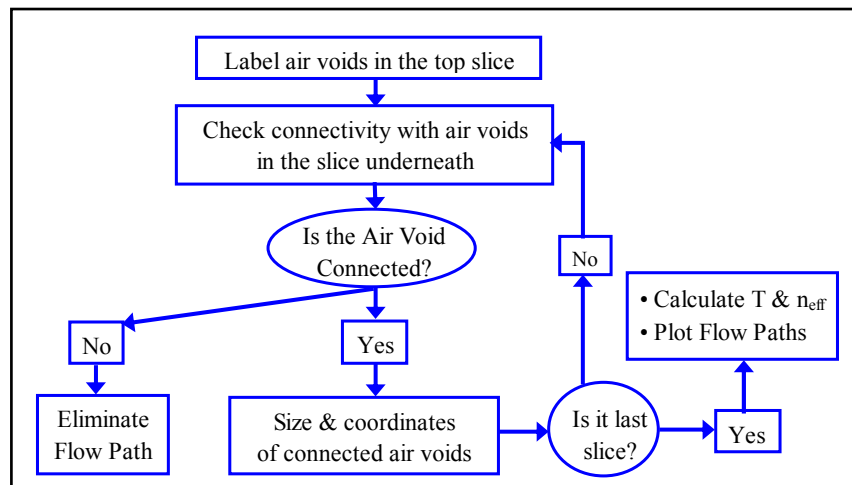
Fig. 3.8. Methodology of analyzing air void connectivity and tortuosity

At this stage, as the images are processed and different air void attributes are calculated, the air void distribution of the specimen can be easily characterized. The different air void attributes (n, n_{eff}, S, and T) will be used in Chapter IV of this dissertation to develop empirical-analytical equations to predict permeability. The 3-D images of connected voids will be used in Chapters V and VI in the simulation of fluid flow in HMA microstructure.

Description of HMA Mixes and Permeability Measurements

The HMA mixes used in this dissertation are divided into two sets. The first set consisted of HMA mixes that were scanned using the X-ray CT system. These HMA mixes will be used in this dissertation in predicting permeability using air void structure characteristics and in the simulation of fluid flow in HMA microstructure.

The second set consisted of mixes that were used by different researchers in studies that involved measurements of permeability. This set includes mixes with a wide range of characteristics that are known to influence permeability measurements. These characteristics include percent air voids, aggregate size distribution, and specimen thickness. In addition, the permeability measurements were conducted using different devices. This set of mixes is shown later to be invaluable in developing the empirical-analytical equations for predicting permeability.

Table 3.1. Description and Reported Permeability Measurements of the HMA Mixes

Specimen	Aggregate Type	% AV	No. of Images per Specimen	No. of Pixels [a]	Image Resolution (mm/pixel)	Reported k_{zz} (10^{-5} cm/s)	Reference	Label in Original Reference
LKC-01	LS	13.1	75	1024	0.146	2984		LS1279
LKC-02	LS	11.7	66	1024	0.146	1137		LS1281
LKC-03	LS	15.4	69	1024	0.146	7949		LS1283
LKC-04	LS	18.8	67	1024	0.146	24525		LS1290
LKC-05	LS	05.5	65	1024	0.146	0		LS1972
LKC-06	LS	05.7	66	1024	0.146	0		LS1974
LKC-07	LS	15.4	78	1024	0.146	6371	Romero (2000)	LS1984
LKC-08	LS	14.3	72	1024	0.146	1746		LS2579
LKC-09	LS	15.4	70	1024	0.146	8716		LS2584
LKC-10	LS	20.0	75	1024	0.146	32350		LS2591
LKC-11	GV	09.2	69	1024	0.146	223		GV1276
LKC-12	GV	13.7	71	1024	0.146	2049		GV1279
LKC-13	GV	14.7	74	1024	0.146	6553		GV1281
LKC-14	GV	17.4	74	1024	0.146	9850		GV1284
F-01	NA	13.9	43	1024	0.146	697		11-1
F-02	NA	06.6	48	1024	0.146	10		11-4
F-03	NA	07.0	39	1024	0.146	37		11-6
F-04	NA	04.4	59	1024	0.146	1		11-7
F-05	NA	05.3	62	1024	0.146	0		12-6
F-06	NA	09.5	54	1024	0.146	49		12-7
F-07	NA	07.1	59	1024	0.146	76		12-9
F-08	NA	06.9	63	1024	0.146	119		12-11
F-09	NA	08.8	33	1024	0.146	120		3-7
F-10	NA	08.2	24	1024	0.146	54		3-11
F-11	NA	09.0	46	1024	0.146	291	Cooley et al. (2002a)	3-14
F-12	NA	08.7	58	512	0.195	269		17-6
F-13	NA	11.0	51	512	0.195	1386		17-7
F-14	NA	09.6	66	512	0.195	656		17-8
F-15	NA	06.0	41	512	0.195	1		17-13
F-16	NA	07.5	56	512	0.195	178		17-14
F-17	NA	04.7	57	1024	0.146	0		4-3
F-18	NA	07.2	54	1024	0.146	28		4-6
F-19	NA	10.6	61	1024	0.146	527		4-9
F-20	NA	09.5	55	1024	0.146	327		4-13
F-21	NA	10.6	88	512	0.186	13477		18-10
F-22	NA	09.6	73	512	0.186	16307		18-11
F-23	NA	07.6	74	512	0.186	1619		18-12
F-24	NA	12.6	51	512	0.186	17789		18-13

Table 3.1. *Continued*

Specimen	Aggregate Type	% AV	No. of Images per Specimen	No. of Pixels (a)	Image Resolution (mm/pixel)	Reported k_{zz} (10^{-5} cm/s)	Reference	Label in Original Reference
SGC-01	GR	7.9	98	512	0.195	67.5		GA-C1
SGC-02	GR	6.9	94	512	0.195	59.0		GA-C2
SGC-03	GR	7.1	93	512	0.195	56.0		GA-C3
SGC-04	GR	7.8	93	512	0.195	25.3		GA-F1
SGC-05	GR	7.4	90	512	0.195	9.3	Birgisson et al. (2003)	GA-F2
SGC-06	GR	7.5	94	512	0.195	34.3		GA-F3
SGC-07	LS	6.6	90	512	0.195	72.4		WR-C1
SGC-08	LS	6.6	72	512	0.195	64.2		WR-C2
SGC-09	LS	6.9	94	512	0.195	29.4		WR-C3
SGC-10	LS	7.0	92	512	0.195	69.6		WR-F1
SGC-11	LS	6.9	84	512	0.195	17.8		WR-F2
SGC-12	LS	7.3	100	512	0.195	9.7		WR-F3
OG-SGC-01	GV	20.3	120	512	0.293	NA		5-GV-30
OG-SGC-02	GV	24.3	107	512	0.293	NA		4-GV-60
OG-SGC-03	GR	24.0	103	512	0.293	NA		5-GR-30
OG-SGC-04	GR	22.2	101	512	0.293	NA		4-GR-60
OG-SGC-05	TR	24.2	116	512	0.293	NA	Watson et al. (2004)	4-TR-30
OG-SGC-06	TR	25.4	111	512	0.293	NA		5-TR-30
OG-SGC-07	TR	18.6	109	512	0.293	NA		5-TR-60
OG-MAR-08	GV	20.1	63	512	0.195	NA		13-GV-25
OG-MAR-09	GV	14.2	64	512	0.195	NA		1-GV-50
OG-MAR-10	GV	12.2	60	512	0.195	NA		2-GV-50

(a): Number of pixels in horizontal (x- or y-) direction.

HMA Mixes Used in the Analysis of Air Void Structure and Numerical Simulation

This set consists of four data groups that are used in predicting permeability of HMA

mixes using different air void characteristics. Table 3.1 shows the HMA properties with

the labels used in this dissertation and the labels in the original references to facilitate referring to these studies.

The first group of HMA mixes consisted of laboratory specimens that were prepared from two different aggregate sources: limestone (LS) and gravel (GV). Three mixes were prepared from LS, while the fourth mix was prepared from GV. The GV mix had a NMAS of 12.5 mm. The other three LS mixes were prepared with NMAS of 12.5mm, 19.0mm, and 25.0 mm. The gradations of the four mixes are shown in Fig. 3.9. Slabs of different thicknesses were prepared using the Linear Kneading Compactor (LKC) at Turner-Fairbank Highway Research Center.

Specimens with 150 mm diameter were cored out of the slabs. All specimens were scanned using X-ray computed tomography. Percent of air voids of the specimens was measured using AASHTO T-166 (2000) and the Corelok device shown in Fig. 3.3 (Cooley et al. 2002b). The measured Corelok percent air voids and measured permeability values are given in Table 3.1. The falling-head Karol-Warner permeameter was used to measure the permeability of all specimens. This device has been described by Maupin (2001). More information on these mixes is given by Romero (2000).
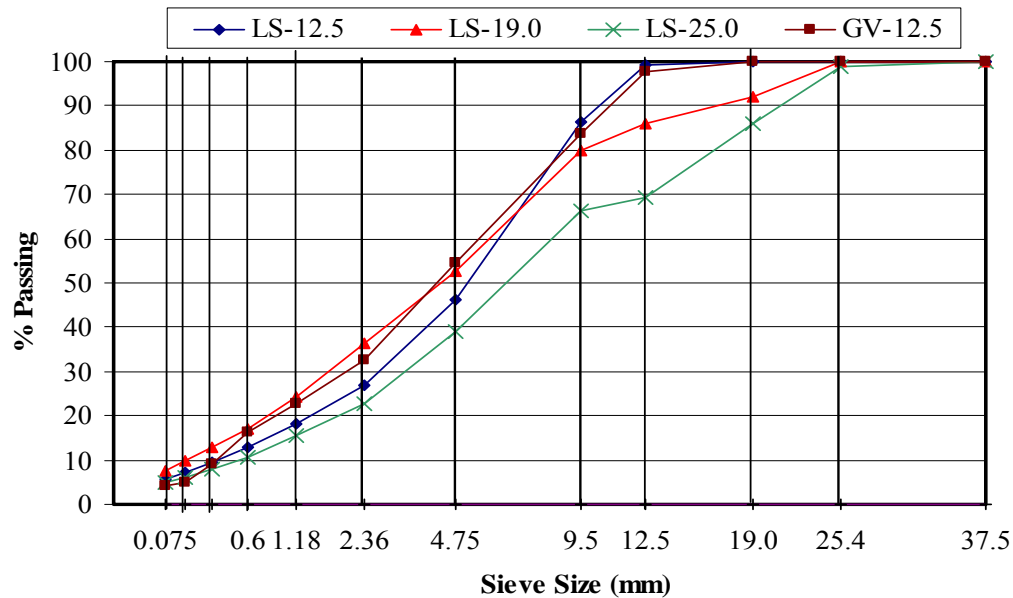
Fig. 3.9. Aggregate gradation of laboratory specimens

Some parts of the top surfaces of the laboratory specimens were cut to obtain smooth surfaces in order to conduct permeability measurements. Percent of air voids were measured on specimens before and after cutting these parts. The results showed that the percent of air voids after cutting the top parts was higher in most specimens than before cutting. This is attributed to the air void distribution in LKC specimens. Fig. 3.10 shows examples of the distribution of air voids in two LKC specimens. As can be seen, percent of air voids increases with depth. Therefore, cutting the top parts that had smaller percent air voids relative to the rest of the specimen, yields higher average percent air voids.
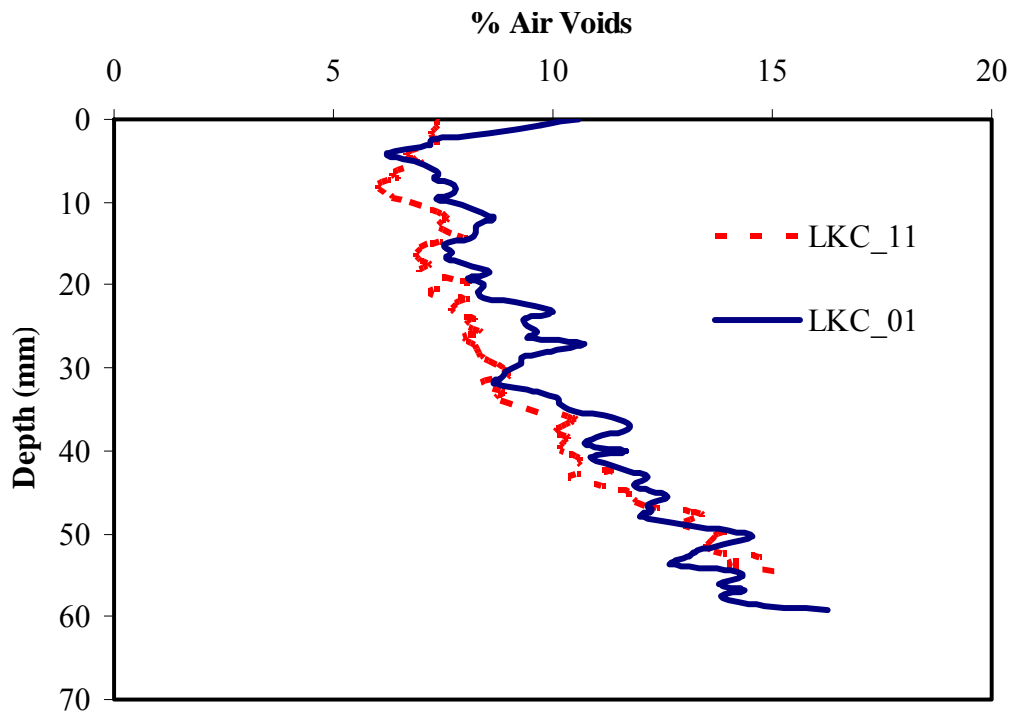
Fig. 3.10. Air void distribution in LKC specimens

Percent of air voids measured using AASHTO T-166 (2000) is in most cases less than percent of air voids measured using the Corelok device. This is similar to the findings by Buchanan and Brown (2001). X-ray CT images showed that the difference in measurements between the two methods is due to the air void distribution of the surface air voids that are located at the edges of the specimen. The ratio of surface air voids to the total air voids in a specimen was calculated using image analysis techniques. As it can be seen in Fig. 3.11, this ratio is much smaller in gravel specimens compared with limestone specimens. This indicates that the gravel specimens had less percent of air voids at the surface, and hence less difference is expected between AASHTO T-166 (2000) and Corelok compared with limestone specimens.
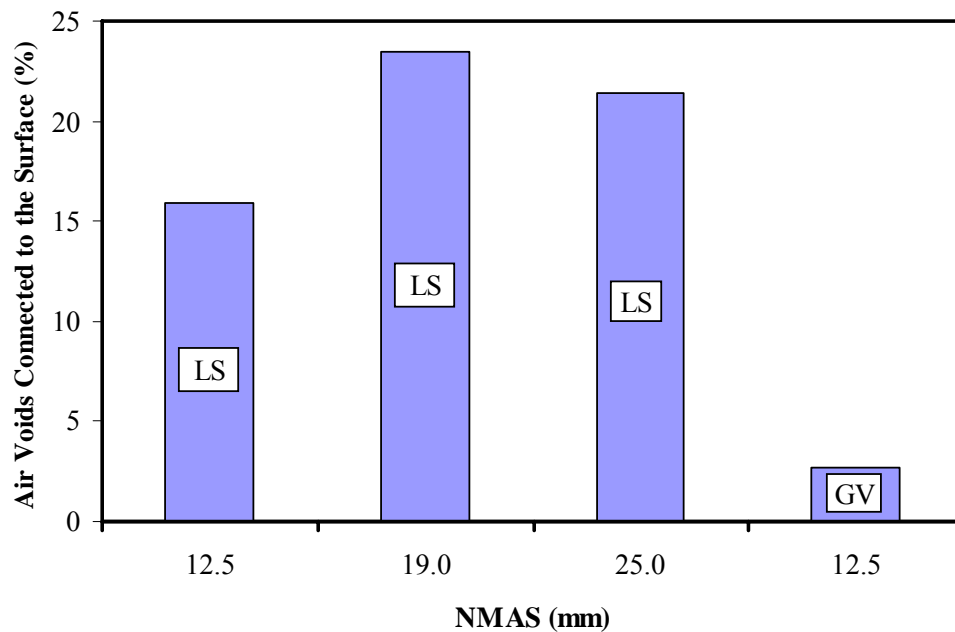
Fig. 3.11. Percent of surface air voids from X-ray CT

The second group consisted of cores that were part of an experiment that involved measuring field permeability of cores recovered from twenty three asphalt pavements (Cooley et al. 2002a; Cooley et al. 2001). These cores are labeled in the original study (Cooley et al. 2002a) by referring to their project number and core number (e.g., core 11-4 is the fourth core from project number eleven). The cores were taken from mixes with NMAS of 9.5, 12.5, and 19.0 mm. Their gradations are passing either above or below the Superpave defined maximum density line at the 2.36 mm (No. 8) sieve. All asphalt mixes were designed according to the Superpave criteria.

The third group of data consisted of Superpave mixes made of two types of aggregates that are used extensively in Florida. Some of the specimens were prepared using limestone (WR) aggregate, whereas the remaining specimens were prepared using crushed granite (GA). A complete description of these Florida Superpave specimens along with their gradations is found in Birgisson et al. (2003) and Castelblanco et al. The permeability of these mixes was measured using a falling-head test method, which was designed by the Florida DOT (Choubane et al. 1998). This is similar to the device used by Cooley et al. (2002a) in the second group of specimens described above. Table 3.1 shows some properties for these Superpave mixes.

The fourth group consisted of open-graded (OG) asphalt specimens. Seven of the specimens were compacted using the Superpave gyratory compactor (OG-SGC), while the other three were compacted using the Marshall hammer (OG-MAR). These specimens were prepared from granite (GR), gravel (GV), and traprock (TR) aggregates, and a NMAS of 19.0 mm (Watson et al. 2004). Table 3.1 shows some of the properties of these OG mixes.

HMA Mixes with Permeability Measurements Used in Empirical-Analytical Equations

This set includes five groups of HMA mixes that are used in Chapter IV in the development of empirical-analytical equations for permeability. Table 3.2 shows the original references where these data sets were used.

Table 3.2. Description of Projects and Permeability Measurements

Reference	Label in the Original Data Source	Permeameter	Test Specimen
Cooley et al. (2002a)	Project 1	NCAT Field Device	Asphalt Pavement
	Project 2		
	Project 3		
	Project 4		
	Project 5		
	Project 6		
	Project 7		
	Project 8		
	Project 9		
	Project 10		
	Project 11		
	Project 12		
	Project 13		
	Project 14		
	Project 15		
	Project 16		
	Project 17		
	Project 18		
	Project 19		
	Project 20		
	Project 21		
	Project 22		
	Project 23		
Cooley et al. (2002a)	Project 5	Florida DOT Device	Field Core
	Project 6		
	Project 7		
	Project 8		
	Project 9		
	Project 10		
	Project 12		
	Project 13		
	Project 14		
	Project 15		
	Project 21		
	Project 22		

Table 3.2. *Continued*

Reference	Label in the Original Data Source	Permeameter	Test Specimen
Kanitpong et al. (2001)	Blend 1 (WI Fine)	ASTM D5084	SGC Specimen
	Blend 2 (Super Fine)		
	Blend 5 (Super Coarse)		
	Blend 6 ("S" Shape)		
Maupin (2000)	Mix 1 (12.5 mm)	Florida DOT Device	SGC Specimen
	Mix 2 (SM-1)		
	Mix 3 (9.5 mm)		
	Mix 4 (12.5 mm)		
	Mix 5 (12.5 mm)		
Mallick et al. (2001)	9.5 mm (Fine Mix)	NCAT Field Device	Asphalt Pavement
	9.5 mm (Coarse Mix)		
	12.5 mm (Coarse Mix)		
	19.0 mm (Coarse Mix)		
	25.0 mm (Coarse Mix)		
Choubane et al. (1998)	I-75 Columbia (19.0 mm)	Florida DOT Device	Field Core
	I-10 Columbia (19.0 mm)		
	I-10 Escambia (19.0 mm)		
	A1A Nassau (19.0 mm)		
	I-10 Okaloosa (19.0 mm)		
	I-10 Suwannee (19.0 mm)		
	I-95 Brevard (12.5 mm)		
	I-75 Columbia (12.5 mm)		
	I-10 Columbia (12.5 mm)		
	I-10 Escambia (12.5 mm)		
	A1A Nassau (12.5 mm)		
	I-10 Okaloosa (12.5 mm)		
	I-10 Suwannee (12.5 mm)		
	I-95 Volusia (12.5 mm)		

The first group of data includes field cores from twenty three projects that were included

in the study by Cooley et al. (2002a). Laboratory permeability was also conducted on a

subset of the field cores using the Florida DOT falling-head permeameter (Cooley et al.

2002a) (Table 3.2).

The second group was obtained from a study by Kanitpong et al. (2001) (Table 3.2). Superpave gyratory compacted (SGC) specimens were produced from four gradations that vary between fine and coarse gradations and one that exhibited "S" shaped aggregate gradation.

In this group of asphalt mixes, all gradations had 12.5 mm NMAS, and the mixes were designed according to the Superpave gradation requirements. For each aggregate gradation blend, specimens were mixed at three different asphalt contents. A total of twelve SGC specimens were tested. The permeability device used here was similar to the one described in ASTM D5084-90 (1999) which operates under constant-head pressure.

The source of the third group is Maupin (2000) (Table 3.2), who prepared SGC specimens from five mixes. Three of the five mixes were designed according to the 12.5 mm Superpave specifications, and one was designed with 9.5 mm Superpave specifications. The fifth mix, which was referred to as SM-1 mix, was a Virginia dense-graded mix with 12.5 mm NMAS and was designed using the Marshall method. The laboratory specimens were prepared at different percentages of air voids. All laboratory permeability measurements were conducted using the Florida DOT device.

The fourth group is from Mallick et al. (2001). They used a modified version of the NCAT field permeameter to measure the permeability of five Superpave projects in

Maine (Table 3.2). The five projects included four coarse-graded mixes of 9.5, 12.5, 19.0, and 25.0 mm NMAS and one project with a fine-graded mix of 9.5 mm NMAS.

A study by Choubane et al. (1998) is the source of the fifth group of data (Table 3.2). They conducted laboratory permeability measurements on field cores using the Florida laboratory permeameter. All field cores were obtained from Superpave mixes with 12.5 mm and 19.0 mm NMAS aggregates. All mixes had gradations that pass below the restricted zone and thus classified as coarse mixes.

Summary

In this chapter, the basic principles and operations of X-ray CT are presented. The result of X-ray CT scanning of HMA mixes is a set of 2-D gray images. These gray images are processed in order to calculate the air void characteristics affecting HMA permeability (porosity, effective porosity, specific surface area, and tortuosity). Two data sets are presented in the chapter. The first data set will be used in this dissertation to relate permeability to air void characteristics and to simulate fluid flow in HMA microstructure. The second data set consists of HMA mixes with a wide range of characteristics. This data set will be used in the development of empirical-analytical equations to predict HMA permeability.

CHAPTER IV

EMPIRICAL-ANALYTICAL PERMEABILITY EQUATIONS USING THE 3-D

DISTRIBUTION OF AIR VOIDS AND HMA PROPERTIES[*]

Introduction

This chapter includes the results of relating HMA permeability to microstructure characteristics such as total percent air voids (n), effective percent air voids (n_{eff}), air void specific surface area (S), and tortuosity (T) of the fluid flow paths. These characteristics were obtained through the analysis of X-ray CT images of the LKC laboratory specimens and field cores shown in Table 3.1. Consequently, empirical-analytical equations are developed to predict permeability based on HMA properties such as aggregate size distribution and percent air voids. The analytical development of these equations is based on the Kozeny-Carman equation. The empirical part of the development was found to be necessary to account for the differences in the permeability measuring devices, the level of saturation, and air void distribution.

Predicting HMA Permeability Using Air Void Characteristics

The air void characteristics of the HMA mixes listed in Table 3.1 will be used in predicting permeability of these mixes. Measured permeability results are plotted for all

---

[*] Material in this chapter is printed with permission from "Proposed methodology for predicting HMA permeability." by Al-Omari, A., Tashman, L., Masad, E., Cooley, A., and Harman, T., (2002). *Journal of the Association of Asphalt Paving Technologists*, 71, 30-58. © 2002 by The Association of Asphalt Paving Technologists. And from "Analytical derivation of permeability and numerical simulation of fluid flow in hot-mix asphalt." by Masad, E., Birgisson, B., Al-Omari, A., and Cooley, A. (2004). *Journal of Materials in Civil Engineering*, ASCE, 16(5), 487-496. © 2004 by American Society of Civil Engineers.

laboratory specimens vs. the percent total air voids measured using Corelok and AASHTO T-166 (2000) in Figs. 4.1 and 4.2, respectively. The method for measuring the percent air voids influences the permeability predictions. For example, one would predict that gravel specimens had less permeability than limestone specimens based on the AASHTO T-166 (2000) measurements, but comparable permeability can be predicted based on the Corelok results. It should be noted that although the percent total air voids is shown to have excellent correlation with permeability for a specific mix, such a relationship cannot be generalized to other mixes due to the different air void distributions in these mixes.
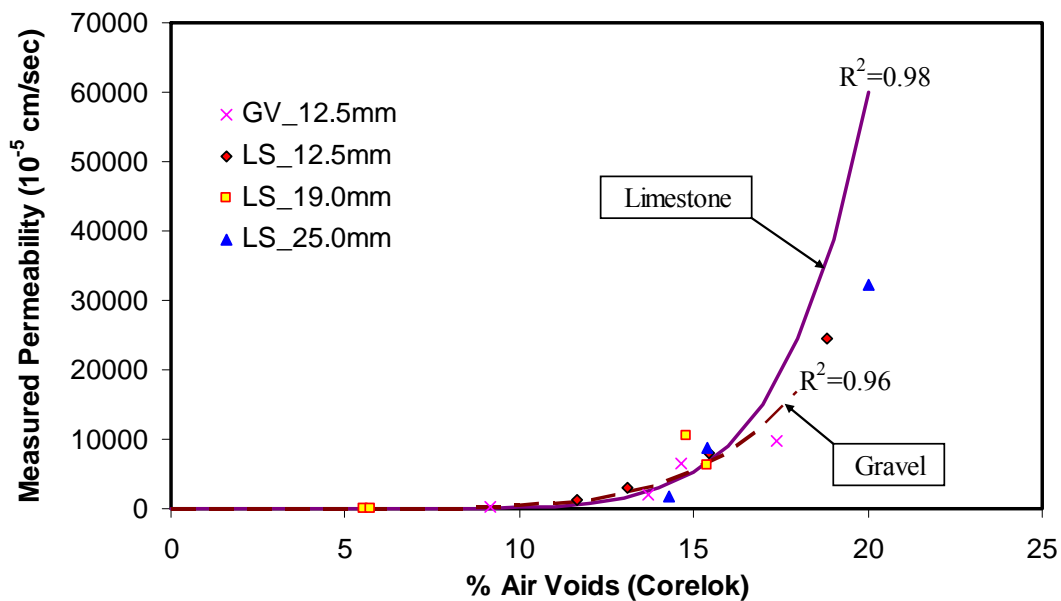
Fig. 4.1. Corelok percent of air void vs. measured permeability

An equation that captures different characteristics of air void distribution is needed to calculate permeability. The difficulty of measuring air void distribution in the past has led several researchers to use average aggregate size as a characteristic length of the material as shown in equations given in Table 2.1. However, HMA mixtures have a wide range of aggregate size distribution, which makes it difficult to use any of the equations given in Table 2.1. In this study, a modified expression of the Kozeny-Carman equation that depends on air void distribution is used. This is advantageous since air void distribution is the controlling factor of fluid flow. Walsh and Brace (1984) presented an alternative form for the Kozeny-Carman equation (Kozeny 1927; Carman 1956) that relates permeability to percent air voids (n), tortuosity (T), and specific surface area (S) as follows:

$$k = \frac{n^3}{c.T^2.S^2} \frac{\gamma}{\mu} \qquad (4.1)$$
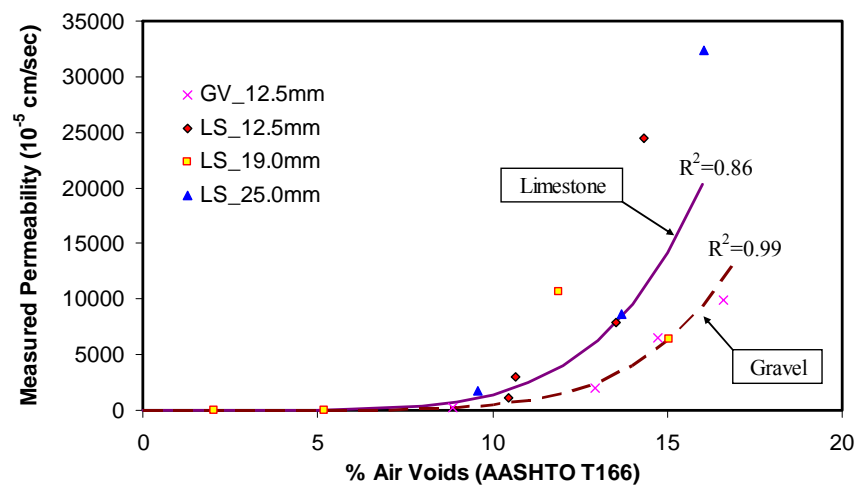
Fig. 4.2. AASHTO percent of air voids vs. measured permeability

In Eq. (4.1), k is the coefficient of permeability in m/sec, c is a constant that ranges between 2 to 3 and depends on the shape of air voids (Blair et al. 1996), S is the surface area parameter, T is tortuosity, and n is the percent air voids. As can be seen later, n can represent either all air voids or only those connected through the specimen. Eq. (4.1) shows that permeability is a function of n, shape of air voids captured using S, and the length of flow paths captured in T. Thus, several air void properties are captured in this equation. As shown in Chapter III, these properties were determined using X-ray CT and image analysis techniques.

The analysis showed that there were a large number of connected paths in most of the laboratory specimens. The splitting of voids along the different paths prevented calculating an average value of tortuosity of all paths. Doing so would yield an average tortuosity value skewed toward the path that has most of the splitting. Also, the average would not reflect the contributions of different paths based on their cross-sectional areas. Therefore, it was decided to classify the paths to different groups. Each group consists of flow paths that initiate from the same surface air void. Then, the weighted average tortuosity was determined for each group (group equivalent tortuosity). The weighted average was based on the smallest cross-sectional area along the path, which actually controls the amount of flow through that path. The smallest cross-sectional area is referred to as the "bottleneck". The tortuosity of the specimen was calculated based on the weighted average of the groups' equivalent tortuosities.

Most studies assume all air voids are involved in the fluid flow process; that is, dead ends, stagnant regions, and isolated air voids are all involved in the flow although they should be neglected (Walsh and Brace 1984). Therefore, these studies had no distinction between the percent total air voids (n) and the effective value (n_{eff}). In this study, however, X-ray CT and image analysis techniques were utilized to quantify (n_{eff}) as described in Chapter III (Fig. 3.8), which represents only the connected air voids that are involved in the fluid flow.

Table 4.1. X-ray CT Measurements and Predicted Permeability for Laboratory Specimens

Specimen	% Air Voids		Specific Surface Area (mm^{-1})	Average Diameter of Air Voids (mm)	Tortuosity	K-C Permeability (10^{-5} cm/sec)
	Total (n)	Effective (n_{eff})				
LKC-01	13.0	3.1	0.24	2.03	3.90	3546
LKC-02	11.6	0.5	0.20	2.28	4.05	2477
LKC-03	15.4	3.9	0.26	2.35	3.49	8010
LKC-04	18.9	9.7	0.30	2.55	3.94	19079
LKC-05	5.3	0.0	0.15	0.72	No Path	42
LKC-06	5.8	0.0	0.12	1.47	No Path	120
LKC-07	15.5	8.3	0.32	1.86	3.67	5372
LKC-08	14.4	3.3	0.23	2.49	3.71	6592
LKC-09	15.4	6.1	0.24	2.53	4.06	9077
LKC-10	20.0	10.7	0.28	3.01	4.94	31931
LKC-11	9.2	0.2	0.21	1.52	3.19	564
LKC-12	13.6	4.3	0.29	1.76	3.527	2951
LKC-13	14.6	1.8	0.25	2.28	3.16	5843
LKC-14	17.2	2.3	0.32	2.24	3.35	9846

The permeability was predicted using the modified Kozeny-Carman equation, Eq. (4.1), with the values of effective percent air voids, tortuosity, and surface area given in Table 4.1. The calculated permeability is compared with laboratory measurements in Fig. 4.3. This is considered reasonable correlation given the wide range of permeability values that can be measured on the same mix using different devices (Lindly and Elsayed 1995; Richardson 1995; Choubane et al. 1998; Huang et al. 1999; Maupin 2001), and the fact that the predictions are based on direct measurements only without fitting parameters.
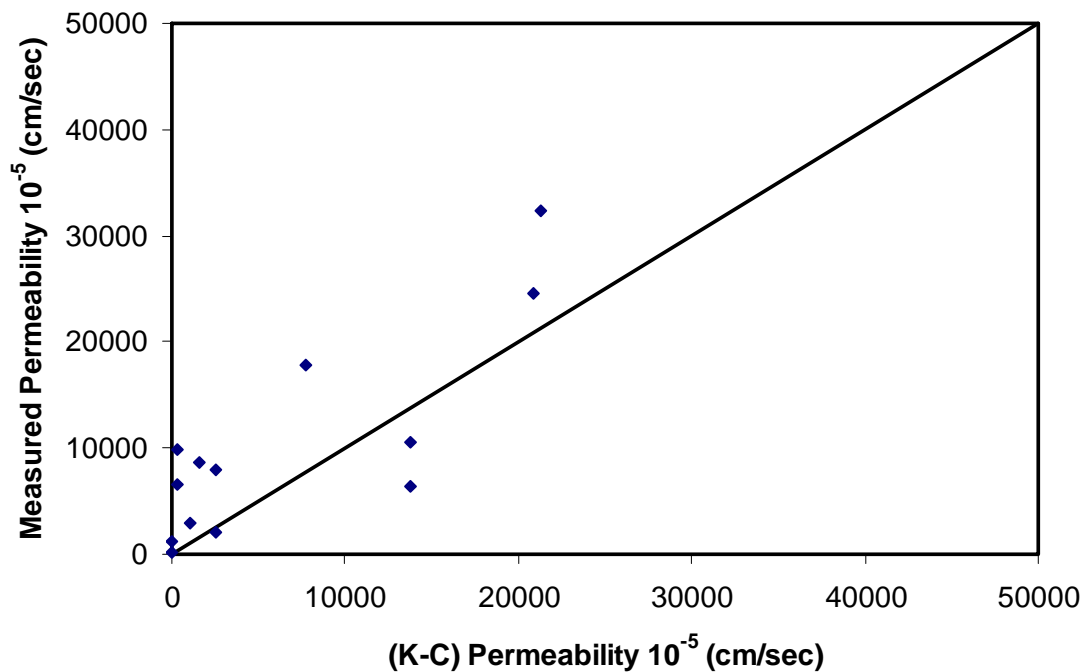
Fig. 4.3. Comparison between predicted and measured permeability values for the LKC specimens, C=3

Even though the modified form of the Kozeny-Carman equation, Eq. (4.1), captures average values of very important characteristics of the HMA internal structure, it is still limited in reflecting the complex distribution of these properties. Consider, for example, the comparison of flow paths shown in Fig. 4.4 between two specimens with approximately the same percent air voids. The first one is a field core, and the second one is an LKC laboratory specimen.

The specimen shown in Fig. 4.4(b) has much higher tortuosity than the one in Fig. 4.4(a). Also, the tortuosity varies among the different paths within the same specimen. Therefore, an average tortuosity value might not be an accurate representation of the flow path irregularity.

Fig. 4.5 shows the distribution of the cross-sectional area of two paths in a field core. This figure illustrates the effect of the bottleneck phenomenon on fluid flow. Although, a flow path might have a large cross-sectional area along the path, the presence of a bottleneck would control the flow in this path. Thus, the field core and LKC specimen exhibited different tortuosity and effective porosity even though the two specimens had approximately the same percent total air voids. Consequently, their permeability values were distinctly different.
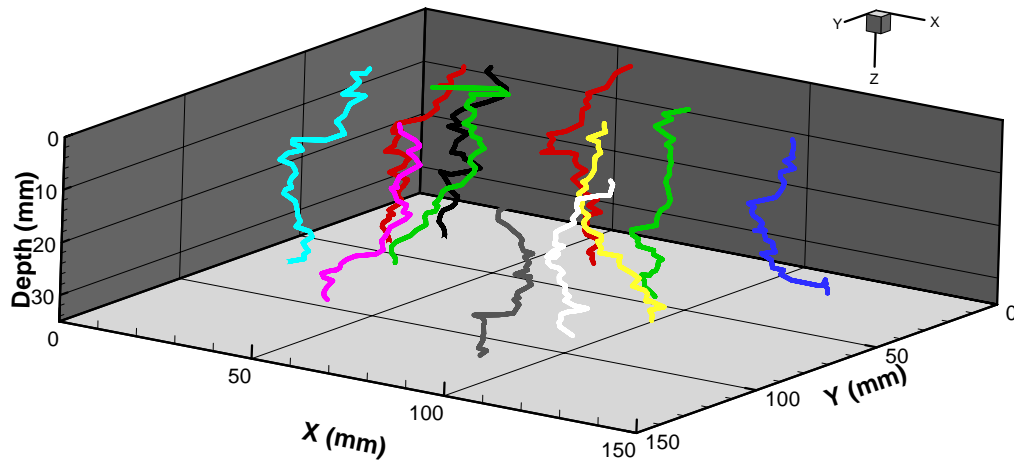
(a) Field core
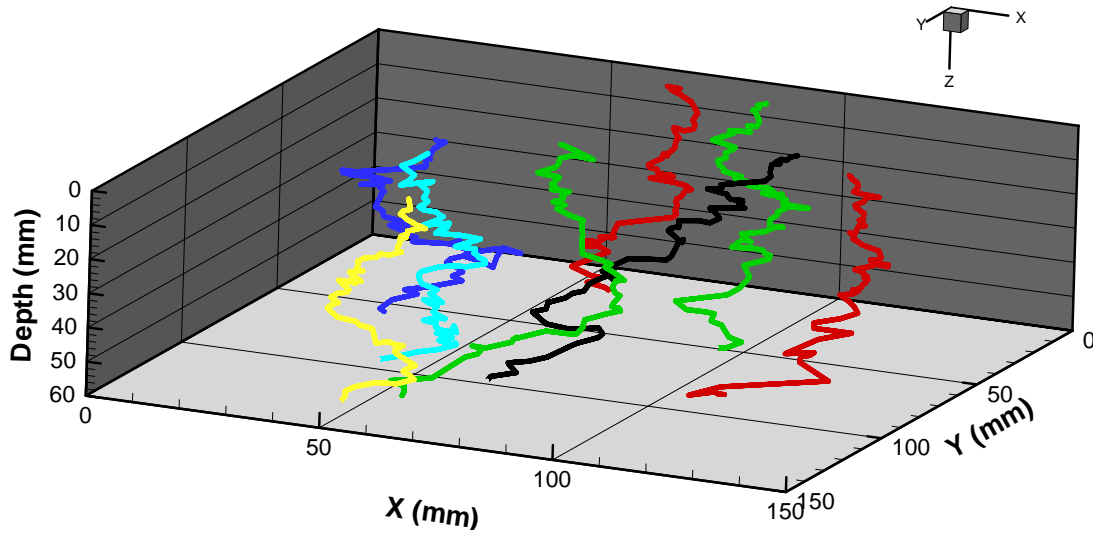
(b) Laboratory LKC specimen

Fig. 4.4. Group representative fluid flow paths in field core and LKC specimen
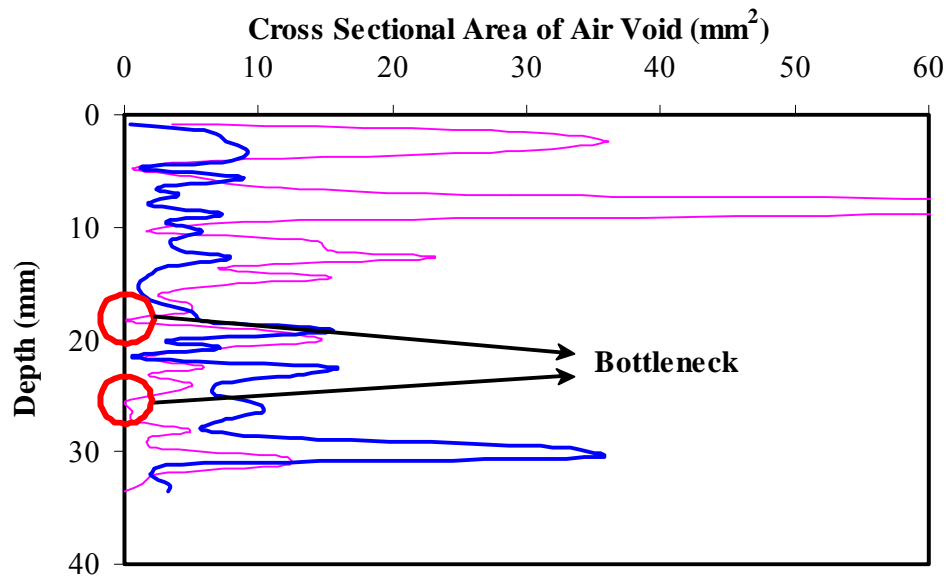
Fig. 4.5. Examples of the distribution of cross-sectional area of fluid flow paths in a field core

The microstructure characteristics were further used to simplify the Kozeny-Carman equation such that the permeability can be predicted based on HMA properties obtained in the laboratory.

Figs. 4.6 and 4.7 show that the effective percent air voids is proportionally related to the total percent air voids and tortuosity. Therefore, tortuosity and effective percent air voids can be replaced by some proportional function of total percent air voids. A power function is selected here based on the results shown in Figs. 4.6 and 4.7. Therefore, the permeability equation can be written in the following form:

$$k = \frac{n^m}{cS^2}\frac{\gamma}{\mu} \qquad (4.2)$$

where S is the specific surface area measured using image analysis techniques and given in Table 4.1 and m is a regression coefficient. Comparison between the calculated permeability values from Eq. (4.2) and laboratory measurements is shown in Fig. 4.8. The m-value was found to be equal to six.
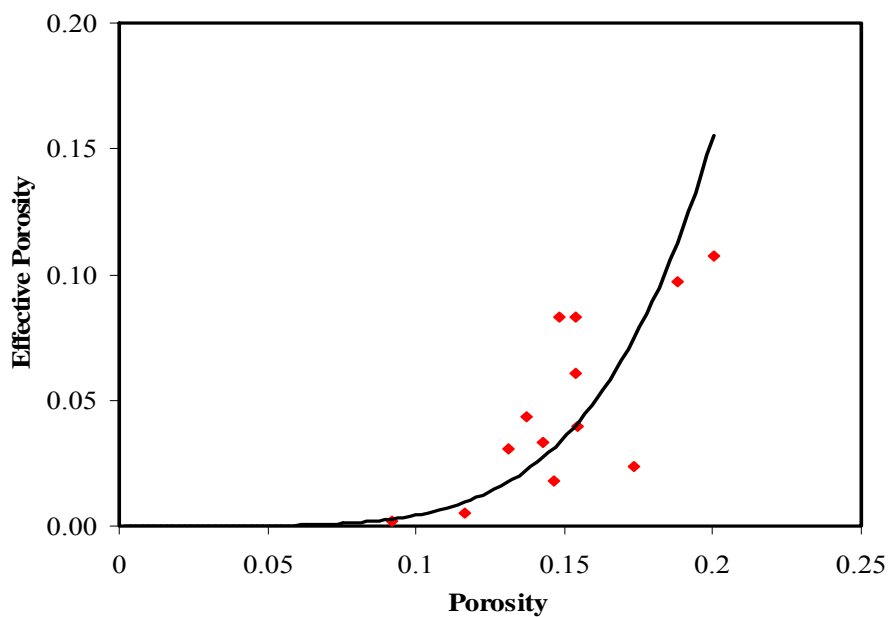
Fig. 4.6. Power law to describe effective porosity in terms of porosity
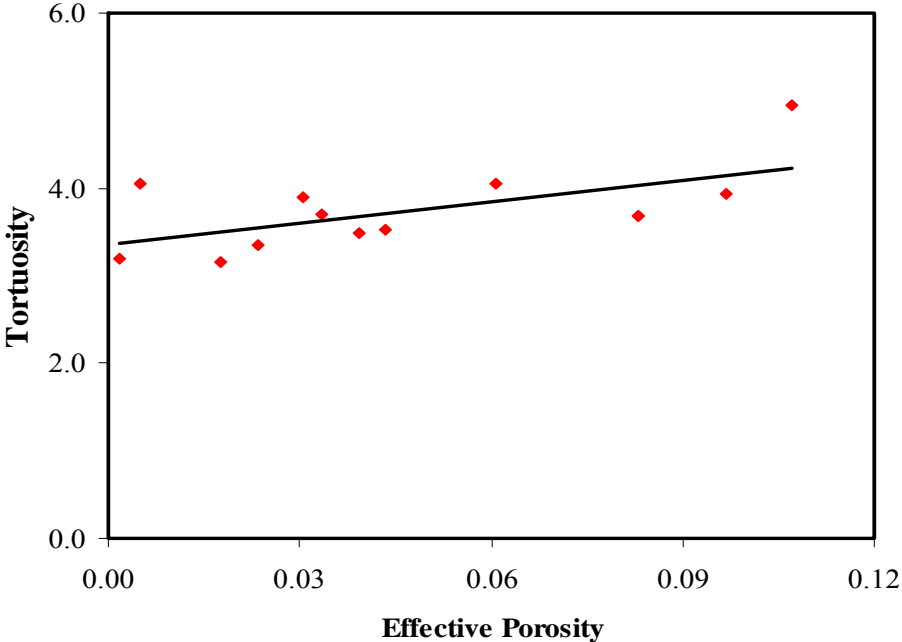
Fig. 4.7. A proportional relationship between tortuosity and effective porosity (n_{eff})
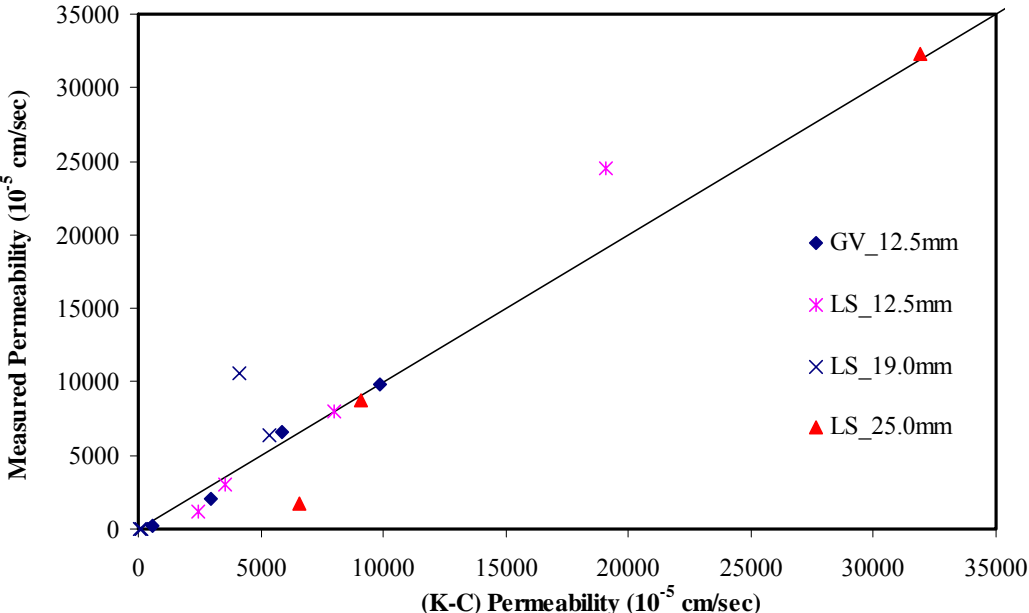
Fig. 4.8. Comparison between K-C and measured permeability for the LKC specimens

Eq. (4.2) was also used to analyze the permeability measurements of field cores. The air

void distribution for some of the field cores is shown in Fig. 4.9, which is quite different

than the distribution shown in Fig. 3.10 for the LKC laboratory specimens.
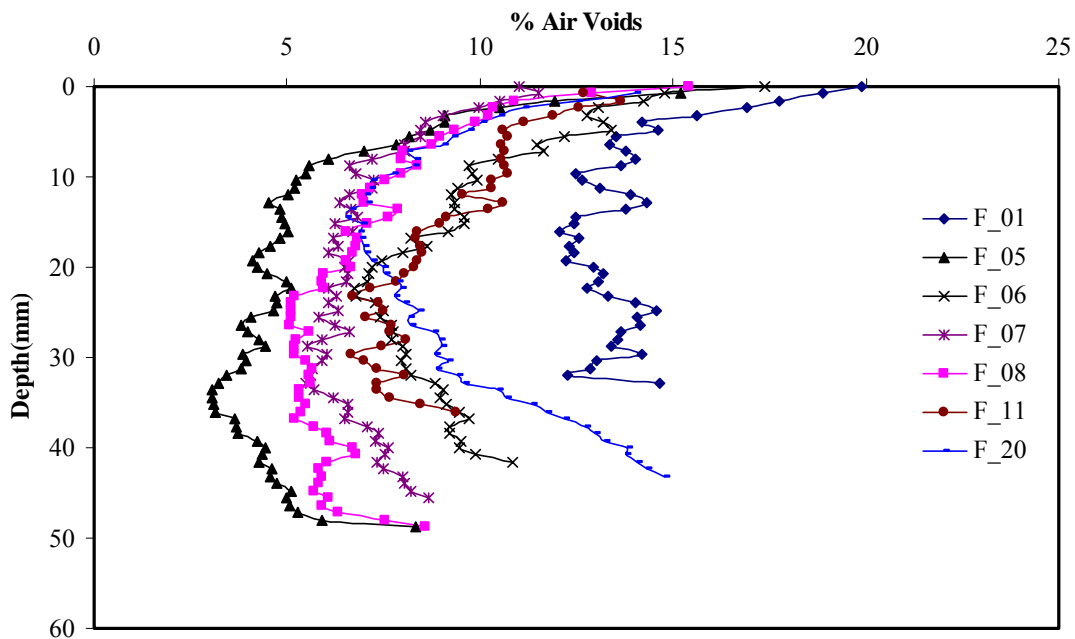
Fig. 4.9. Air void distribution in field cores

The specific surface area of all cores was measured using Eq. (3.2). It was found that the

values were similar among cores that had the same NMAS and gradation type (below or

above the restricted zone). Therefore, the specific surface area values were averaged for

each group of cores that shared these properties. These average values are given in Table

4.2. The coefficient of variation was around 15% for each group of field cores. It can be

seen that mixes with 12.5 mm NMAS had higher specific surface area compared with the 19.0-mm mixes. Also, the gradations above the restricted zone (fine gradation) had higher surface area than the ones below the restricted zone (coarse gradation). Field cores with 9.5 mm NMAS had smaller specific surface area compared with 12.5- and 19.0-mm mixes for the same gradation type. These trends suggest that the air voids become smaller as the NMAS decreases and when the gradation becomes finer.

Table 4.2. Average Specific Surface Area for Field Cores

Projects	Gradation	Average Specific Surface Area (mm^{-1})
3,4	9.5-BRZ	0.229
11	12.5-ARZ	0.352
12	12.5-BRZ	0.182
17	19.0- ARZ	0.180
18	19.0-BRZ	0.161

The average specific surface area given in Table 4.2 along with the percent total air voids given in Table 3.1 were used to predict permeability values using Eq. (4.2). The comparison between field permeability measurements and the values predicted by the Kozeny-Carman equation is shown in Fig. 4.10. This figure is plotted on a log-log scale because of the wide range of values. Similar to laboratory specimens, the *m*-value for the field cores was equal to six. Considering the high variability typically encountered in HMA mix permeability, the correlation in Fig. 4.10 is deemed satisfactory. Most of the

points above the equality line belong to project 18 that had significantly higher field

permeability compared with the other projects.
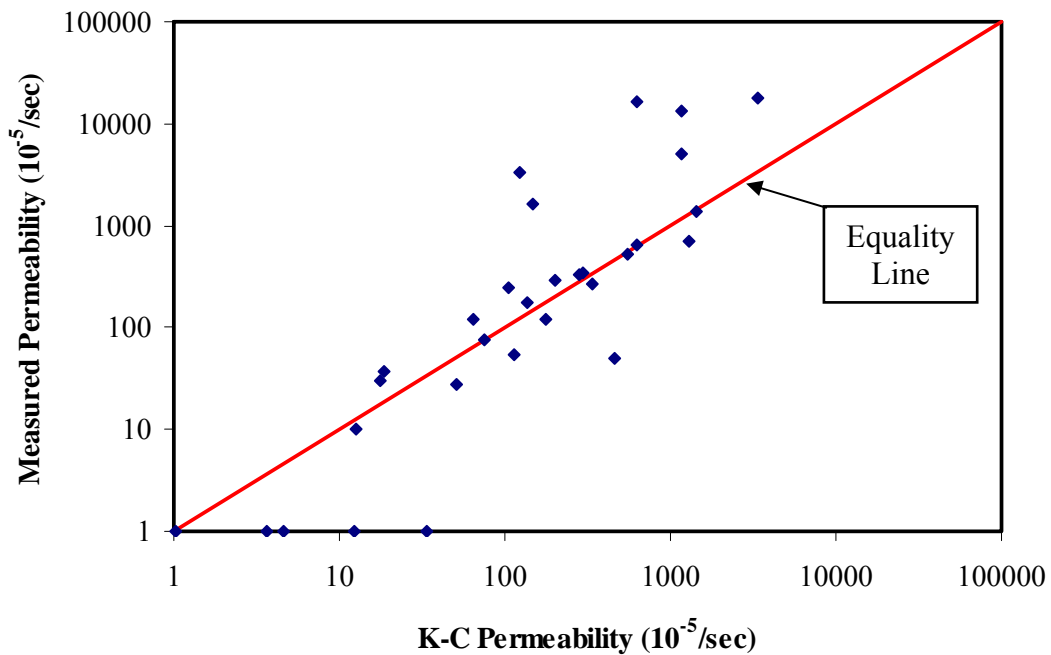
Fig. 4.10. Comparison between the predicted and measured permeability values for field

cores

Predicting HMA Permeability Using Laboratory Measurements

The results presented in the previous section motivated an effort to further simplify Eq.

(4.2) such that all the parameters of the new equation can be measured in the laboratory.

Percent of air voids (n) in Eq. (4.2) can be easily estimated in the laboratory, whereas the

specific surface area of air voids (*S*) needs a more complex approach to be evaluated. For this reason, the relationship between the specific surface area of both aggregates (S_{Agg}) and air voids (*S*) is studied. The surface area of aggregates can be measured simply in the laboratory using the procedure recently developed by Christensen (2001). Only the gradation and density of the aggregates are needed to determine S_{Agg} assuming that the particles are of cubical shape. For each sieve, the weight and average particle size are used to calculate the number of particles with cubical shape that retained on this sieve. The surface area of these particles is calculated with the units of m^2/kg. This value is multiplied by aggregate density to determine the surface area in the units of 1/m. Finally, the surface areas of all sieves are added to get the total surface area for the aggregate sample. The procedure does not address the influence of texture and particle shape on surface area. However, it is considered an improvement over the current method used in the practice for estimating surface area (Roberts et al. 1996).

Fig. 4.11 shows the relationship between the surface area of air voids (*S*) measured using X-ray CT images and the surface area of aggregates (S_{Agg}) for the field cores taken from different projects evaluated by Cooley et al. (2002a). Using the relationship shown in Fig. 4.11, Eq. (4.2) can be substituted by the empirical formula shown in Eq. (4.3):

$$k = \frac{n^m}{cS_{Agg}^t}\frac{\gamma}{\mu} \qquad (4.3)$$

where *n* is the total percent air voids in an asphalt mix, S_{Agg} is the aggregate specific surface area in units of (mm^{-1}), and γ and μ are kept in the above equation simply to

maintain the same form as Eq. (4.1). The *c*, *m*, and *t* values are obatined through statistical data fitting to the permeability values expressed in the units of 10^{-5} cm/sec.
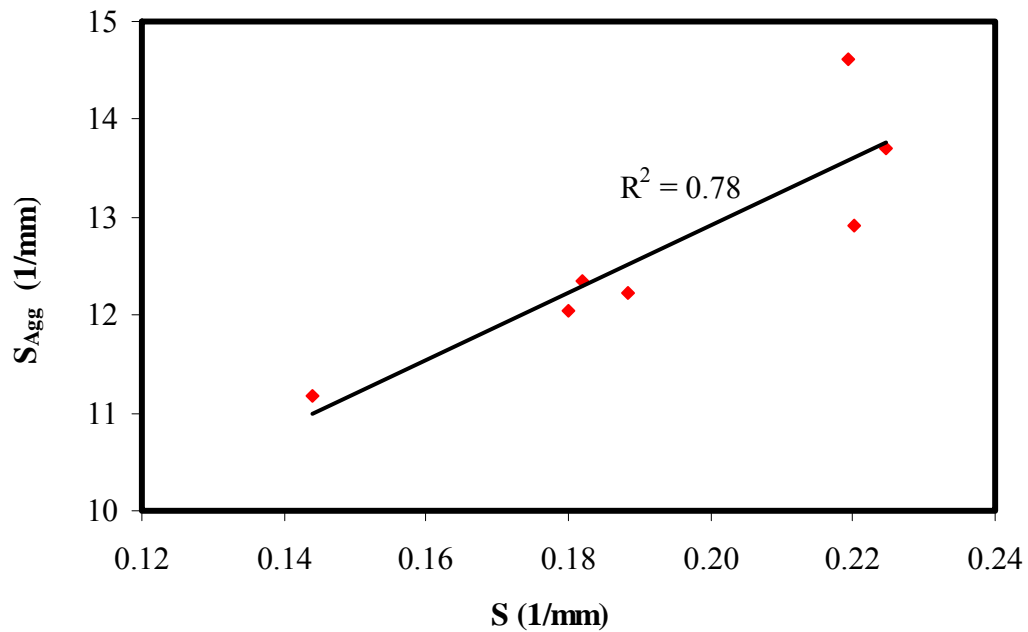
Fig. 4.11. The relationship between surface area of aggregate (S_{Agg}) and air voids (S)

Initial statistical regression analyses using all available permeability measurements were conducted to determine the range of values for the *c*, *t*, and *m* parameters. It was found that the *c* value was close to unity and the *t* value varied within a small range around five (5.02–5.14), irrespective of the measurement method and mix characteristics. Therefore, it was decided to assign constant values to *c* and *t* and fit all the available data using the *m* parameter only.

For the data from Cooley et al. (2002a), the relationship between the laboratory permeability measurements and permeability calculated using Eq. (4.3) is presented in Fig. 4.12 by grouping the projects according to the NMAS. As can be seen, most of the data fall close to the equality line, and reasonable correlation exists between the measurements and the equation except for the projects with 25.0 NMAS. Similar results were found for the field data.
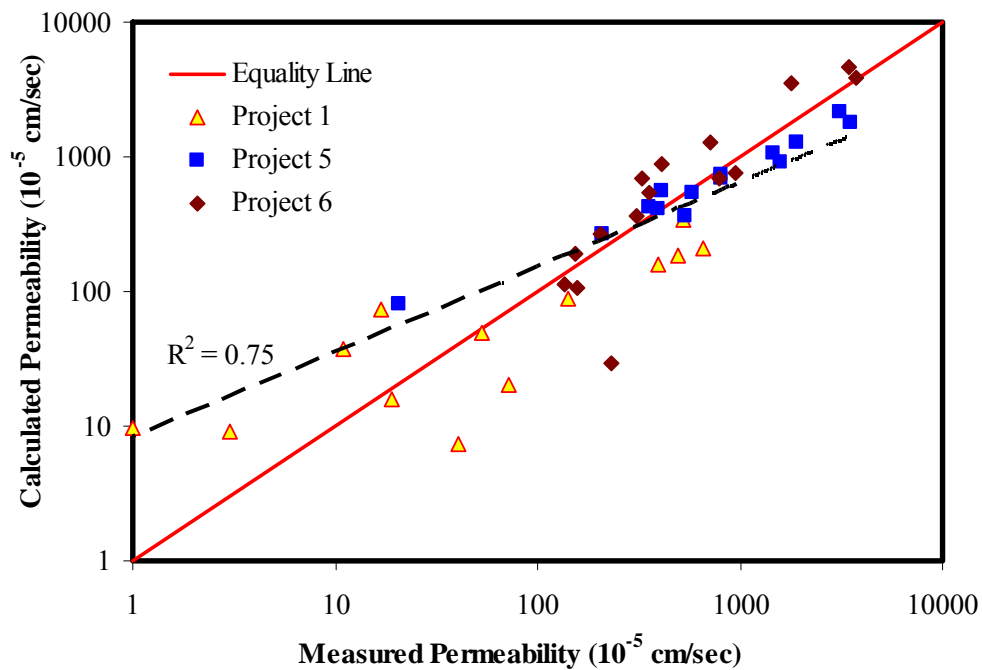
(a) 9.5 mm NMAS

Fig. 4.12. Calculated permeability, Eq. (4.3), vs. laboratory measurements for the data from Cooley et al. (2002a)
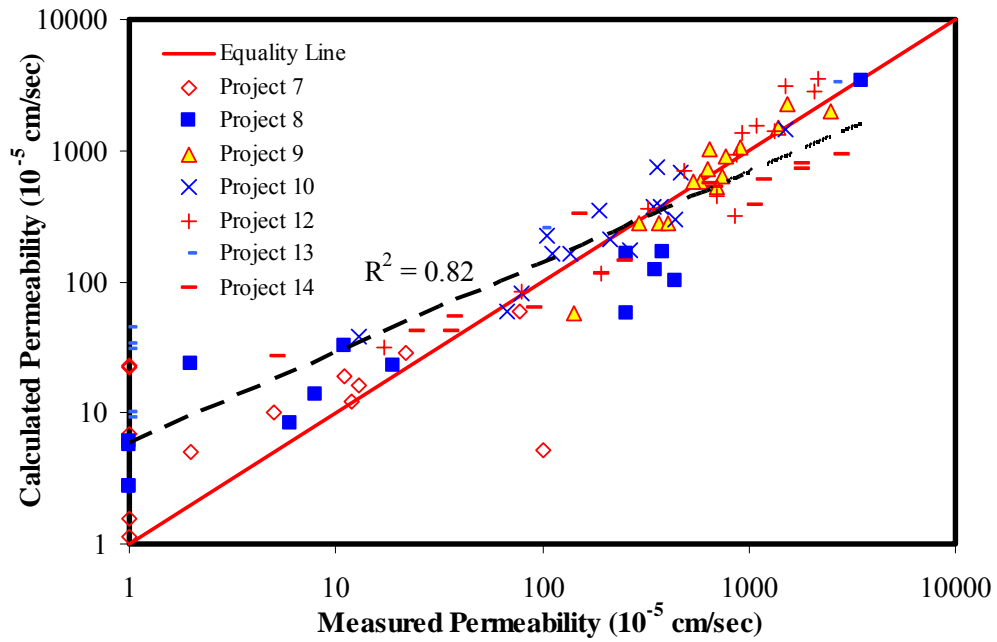
(b) 12.5 mm NMAS
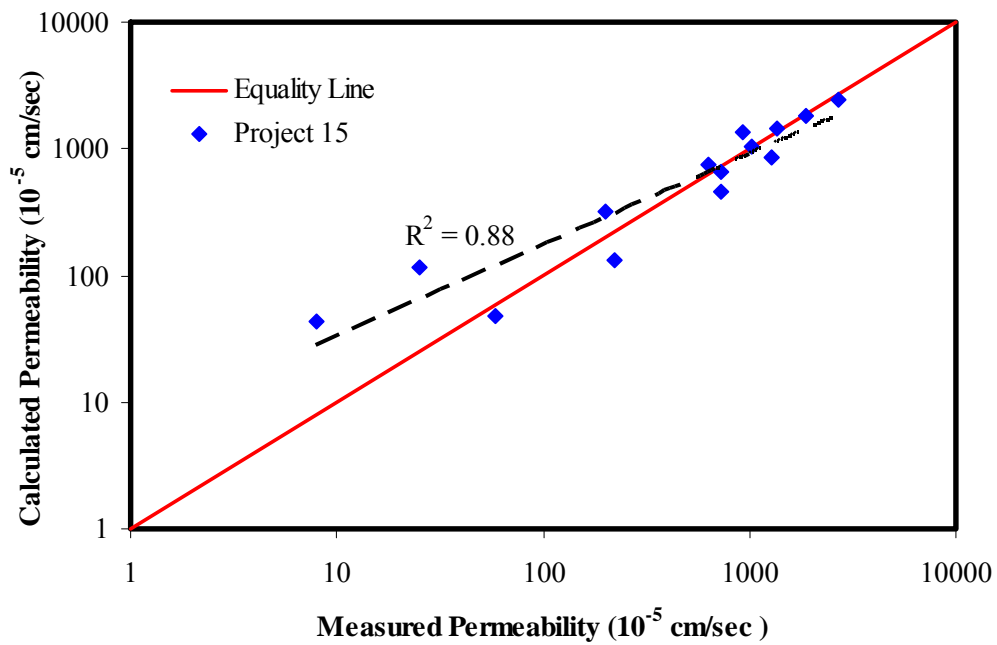
(c) 19.0 mm NMAS
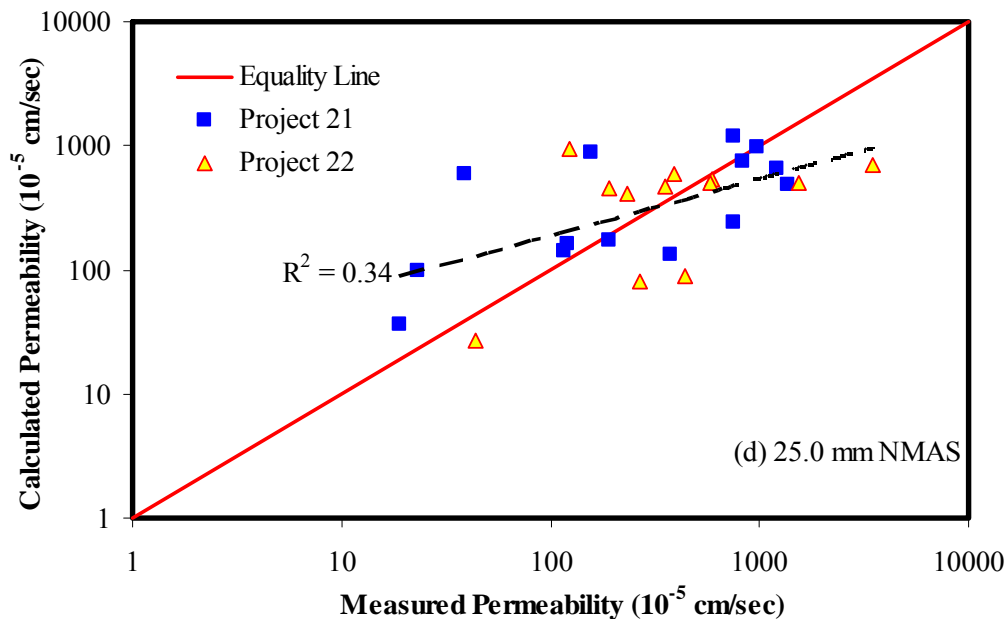
Fig. 4.12. *Continued*

(d) 25.0 mm NMAS

Fig. 4.12. *Continued*

Several factors can contribute to the poor correlation for mixes with 25.0 mm NMAS. These mixes experience very high permeability relative to all other mixes. Therefore, the fluid flow might not adhere to the conditions governing the derivation of the Kozeny-Carman equation such as small Re and creeping flow behavior. In addition, it would be difficult to control leakage around the laboratory specimen circumference due to the high surface irregularity caused by the large NMAS. It is interesting to note that the *m*-value varies within a small range between 4.6 and 5.8 with the exception of project 5, which is a Stone Matrix Asphalt (SMA) mix (Table 4.3).

Table 4.3. Description of Projects and Permeability Measurements

Reference	Label in the Original Data Source	*m*-values
Cooley et al. (2002a)	Project 1	5.7
	Project 2	5.8
	Project 3	5.5
	Project 4	5.3
	Project 5	4.1
	Project 6	5.6
	Project 7	4.9
	Project 8	5.4
	Project 9	5.6
	Project 10	5.8
	Project 11	5.6
	Project 12	5.5
	Project 13	5.6
	Project 14	5.0
	Project 15	5.6
	Project 16	4.8
	Project 17	5.1
	Project 18	4.6
	Project 19	4.9
	Project 20	5.2
	Project 21	4.6
	Project 22	4.6
	Project 23	4.5
Cooley et al. (2002a)	Project 5	4.0
	Project 6	5.5
	Project 7	5.0
	Project 8	5.3
	Project 9	5.1
	Project 10	5.7
	Project 12	5.2
	Project 13	5.5
	Project 14	5.5
	Project 15	5.6
	Project 21	5.0
	Project 22	5.2

Table 4.3. *Continued*

Reference	Label in the Original Data Source	*m*-values
Kanitpong et al. (2001)	Blend 1 (WI Fine)	6.1
	Blend 2 (Super Fine)	6.3
	Blend 5 (Super Coarse)	6.9
	Blend 6 ("S" Shape)	6.3
Maupin (2000)	Mix 1 (12.5 mm)	4.7
	Mix 2 (SM-1)	4.7
	Mix 3 (9.5 mm)	6.0
	Mix 4 (12.5 mm)	4.7
	Mix 5 (12.5 mm)	4.7
Mallick et al. (2001)	9.5 mm (Fine Mix)	5.3
	9.5 mm (Coarse Mix)	6.1
	12.5 mm (Coarse Mix)	6.1
	19.0 mm (Coarse Mix)	5.3
	25.0 mm (Coarse Mix)	4.8
Choubane et al. (1998)	I-75 Columbia (19.0 mm)	5.7
	I-10 Columbia (19.0 mm)	5.3
	I-10 Escambia (19.0 mm)	5.9
	A1A Nassau (19.0 mm)	5.5
	I-10 Okaloosa (19.0 mm)	5.5
	I-10 Suwannee (19.0 mm)	6.0
	I-95 Brevard (12.5 mm)	5.5
	I-75 Columbia (12.5 mm)	5.5
	I-10 Columbia (12.5 mm)	5.3
	I-10 Escambia (12.5 mm)	5.5
	A1A Nassau (12.5 mm)	5.5
	I-10 Okaloosa (12.5 mm)	5.4
	I-10 Suwannee (12.5 mm)	5.2
	I-95 Volusia (12.5 mm)	5.5

The relationship between permeability measurements and Eq. (4.3) for the SGC specimens from the study by Kanitpong et al. (2001) is shown in Fig. 4.13. As can be seen in Fig. 4.13 and Table 4.3, reasonable correlation was obtained with *m*-values in the range between 6.1 and 6.9. As shown in Fig. 4.14 and Table 4.3, very good correlation

between permeability measurements using the Florida DOT device and calculated permeability using Eq. (4.3) was obtained using an *m*-value of 6 for the 9.5-mm mix and 4.7 for the other mixes of the specimens from Maupin (2000).
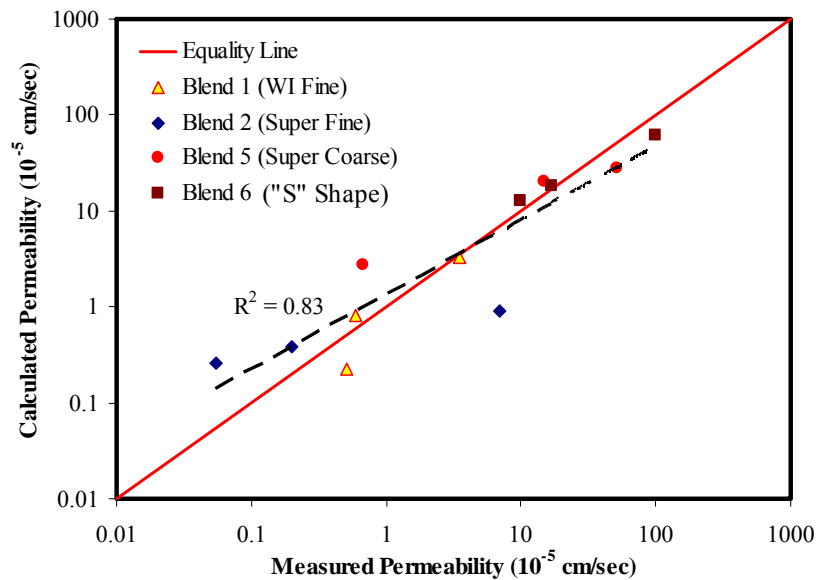
Fig. 4.13. Calculated permeability, Eq. (4.3), vs. laboratory measurements for the data from Kanitpong et al. (2001)

The results of fitting data from Mallick et al. (2001) are shown in Fig. 4.15 and Table 4.3. Excellent correlation was achieved with this set of data using an *m*-value that ranges from 4.8 to 5.3. On the other hand, Fig. 4.16 shows that an *m*-value from 5.2 to 6.0 gave very good correlation with the permeability measurements for data from Choubane et al. (1998).
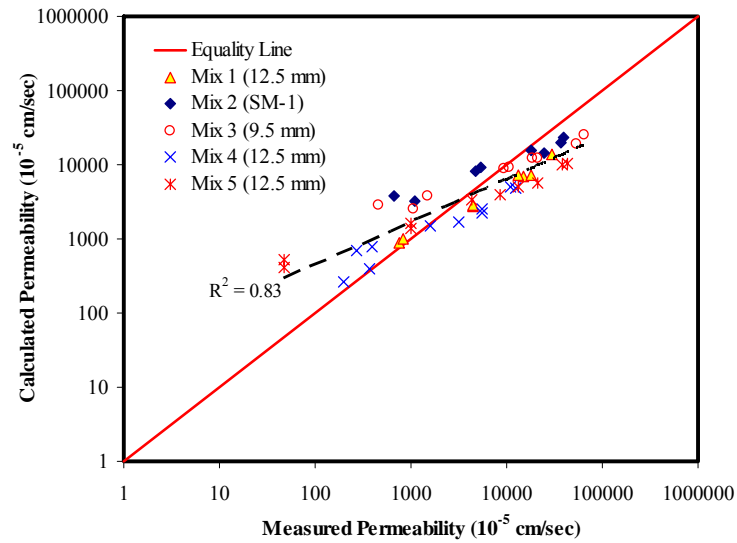
Fig. 4.14. Calculated permeability, Eq. (4.3), vs. laboratory measurements for the data from Maupin (2000)
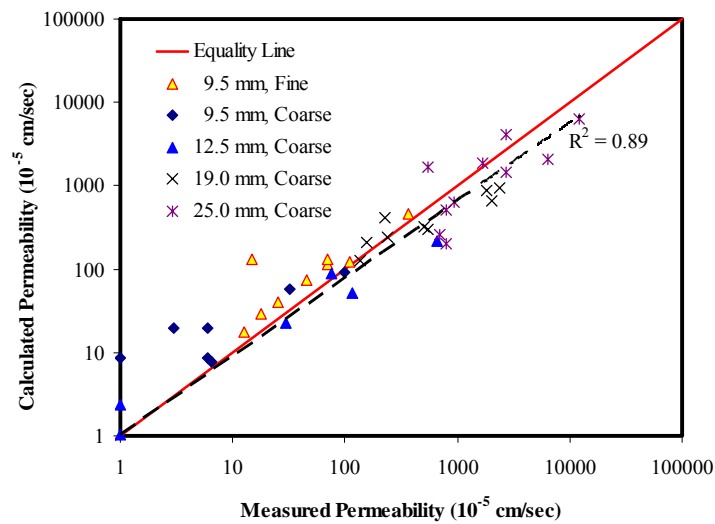
Fig. 4.15. Calculated permeability, Eq. (4.3), vs. field measurements for the data from Mallick et al. (2001)
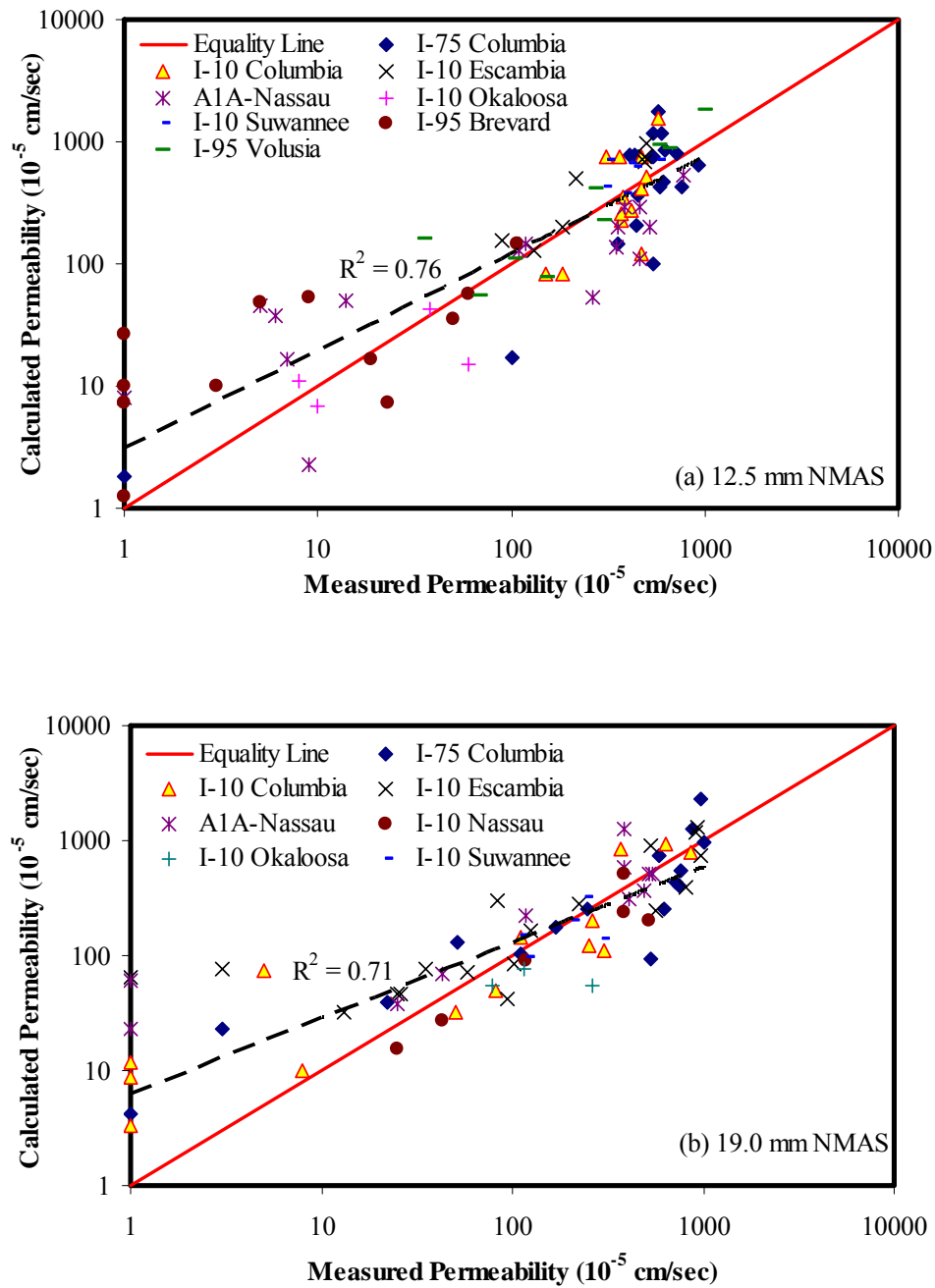
Fig. 4.16. Calculated permeability, Eq. (4.3), vs. laboratory measurements for the data from Choubane et al. (1998)

Statistical analysis was conducted to determine the factors that influence the *m*-value distribution. The *m*-value for each field core and gyratory specimen was calculated using Eq. (4.3) such that the calculated permeability matches the measured value. The *m*-values for the field and laboratory measurements are given in Fig. 4.17. It can be seen that the *m*-values for all measurements had a wide distribution, and consequently, an average or a range for the *m*-value cannot be specified to reasonably approximate all laboratory and field measurements. The relationship between specimen thickness and the *m*-value was also investigated using the measurements by Cooley et al. (2002a), and almost no correlation was detected.
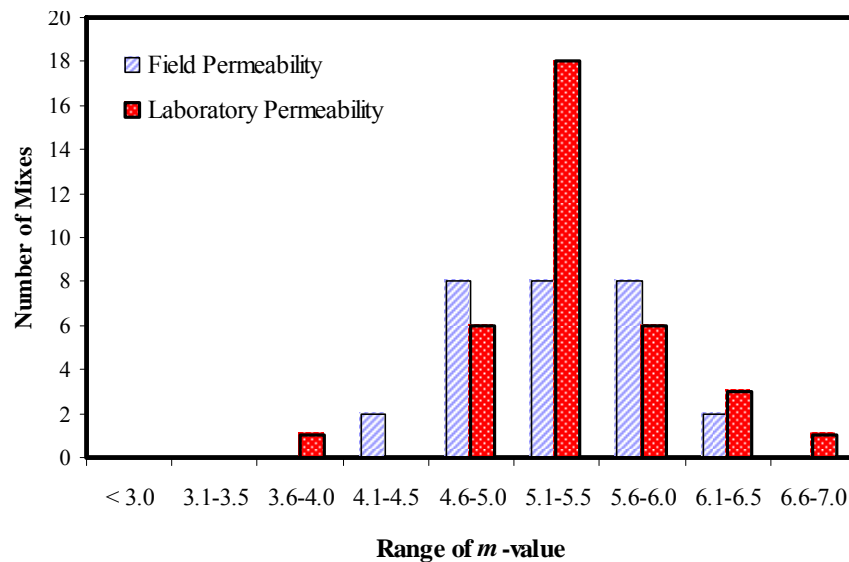
Fig. 4.17. The Distribution of *m*-values for Field and Laboratory Measurements; Laboratory Data. (Average = 5.4, Standard Deviation = 0.54), Field Data (Average = 5.3, Standard Deviation = 0.50)

An important factor that can influence the *m*-value distribution is the test method. The permeability test methods vary significantly in their operational characteristics between the field and laboratory measurements and among laboratory test methods in using field cores or gyratory specimens, constant-head or falling-head, type of control of lateral leakage, and in the procedure used to ensure specimen saturation prior to measuring permeability. In order to investigate the relationship between the test method and *m*-value distribution, the probability density function of the *m*-values of each data set was determined. In general, it was found that the normal distribution gives the best description of each data set as shown in Fig. 4.18.

Fig. 4.18(a) shows that the averages of the data sets from Cooley et al. (2002a) and Choubane et al. (1998), which were obtained using the Florida DOT device and field cores, were very close. The averages of the data sets from Maupin (2000) and Kanitpong et al. (2001) were different from the other two sets. This can be attributed to the use of gyratory specimens in the study by Maupin (2000) and the use of a different testing method (ASTM D5084-90 1999) in the measurements by Kanitpong et al. (2001). The distributions of the *m*-values from the field measurements are shown in Fig. 4.18(b). As expected, the averages of both distributions were very close since the same testing device was used in both studies. The standard deviations of the data sets were different due to the variation in the number of mixes evaluated in each data set.
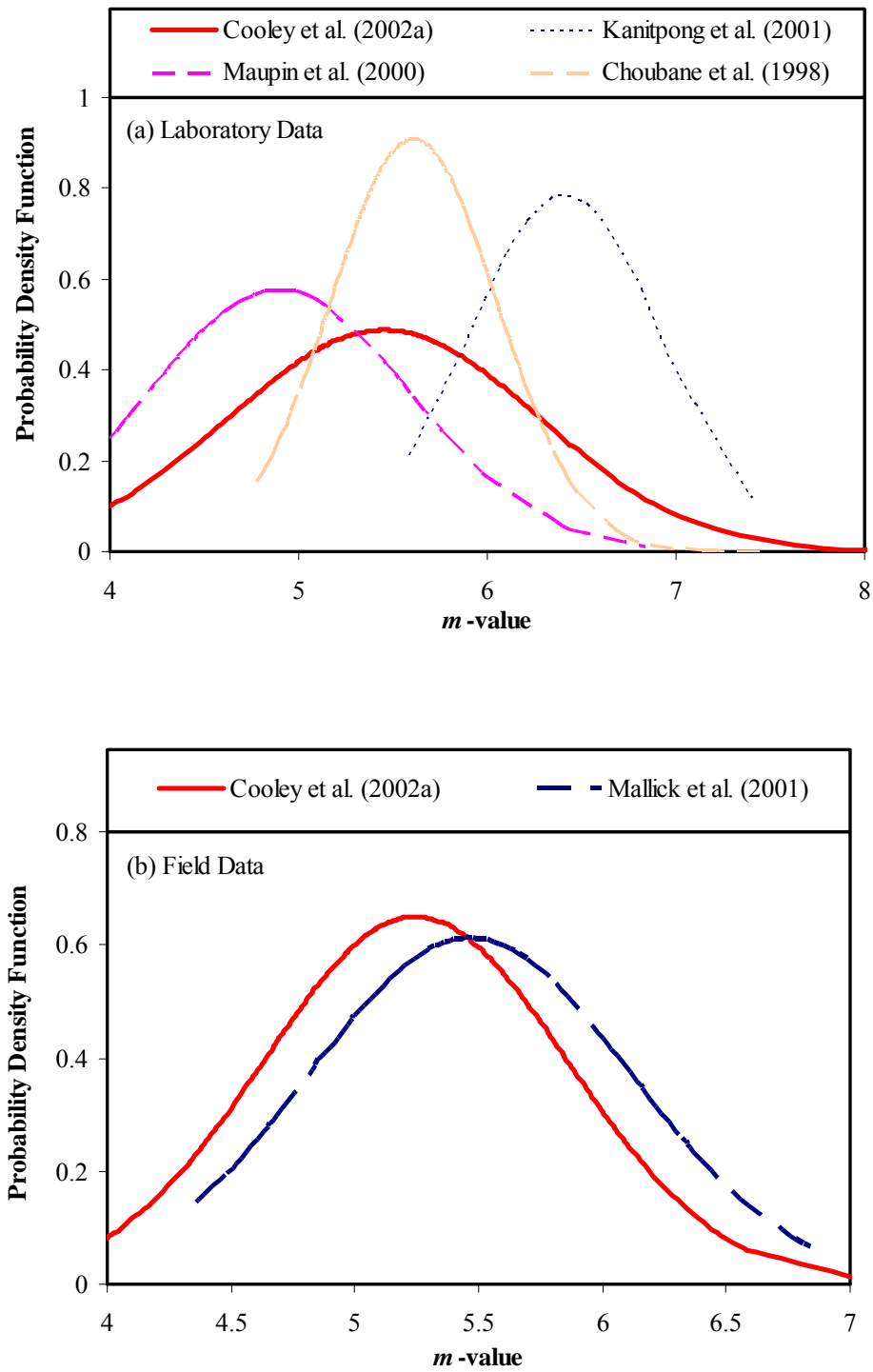
Fig. 4.18. Probability density functions of *m*-values for different test methods

Based on the results discussed above, it is proposed that the *m*-value is mainly dependent on the permeability testing method (i.e., field vs. laboratory and laboratory device type), and test sample (i.e., gyratory specimen and field core). As a result, Eq. (4.3) can be calibrated using available data from each test method to determine the range for the *m*-value that would achieve reasonable approximation of the experimental permeability measurements.

The effect of the asphalt content on permeability of HMA mixes is not explicitly shown in Eqs. (4.1), (4.2), and (4.3). As was suggested by Dr. Lytton at Texas A&M University, this effect can be included by considering an equivalent aggregate size that includes the average particle size and average asphalt film thickness. In order to do so, the original Kozeny-Carman equation shown in Eq (4.4) and Table 2.1 can be used to predict permeability:

$$k = \frac{C n_a^{3} D_s^{2}}{\left(1 - n_a\right)^{2}} \frac{\gamma}{\mu} \qquad (4.4)$$

In this equation, the average diameter of aggregates (D_s) can be substituted by an equivalent average diameter of particles of asphalt mix ($D_{Effective}$) that represents the average diameter of aggregates coated by asphalt binder. The new equivalent average diameter of particles of asphalt mix will be larger than the original diameter of aggregates.

Fig. 4.19 shows a representation of the volumes of phases in a compacted asphalt mix specimen. In this figure, n is the percent air voids in an HMA specimen, b_a and b_e are the percents of the absorbed and effective (or non-absorbed) asphalt, respectively. w_b is the percent of asphalt content in the mix, and γ_t and γ_s are the total and solid unit weights, respectively. G_s is the specific gravity of the solid part of the mix. *VMA* in Fig. 4.19 is the voids in mineral aggregate which represents the volume of intergranular void space between the aggregate particles of a compacted paving mixture. This value includes air voids and volume of the asphalt not absorbed into the aggregate (Roberts et al. 1996). For a unit volume mix, *VMA* is the summation of the percent air voids (n) and the percent of the non-absorbed asphalt (b_e).
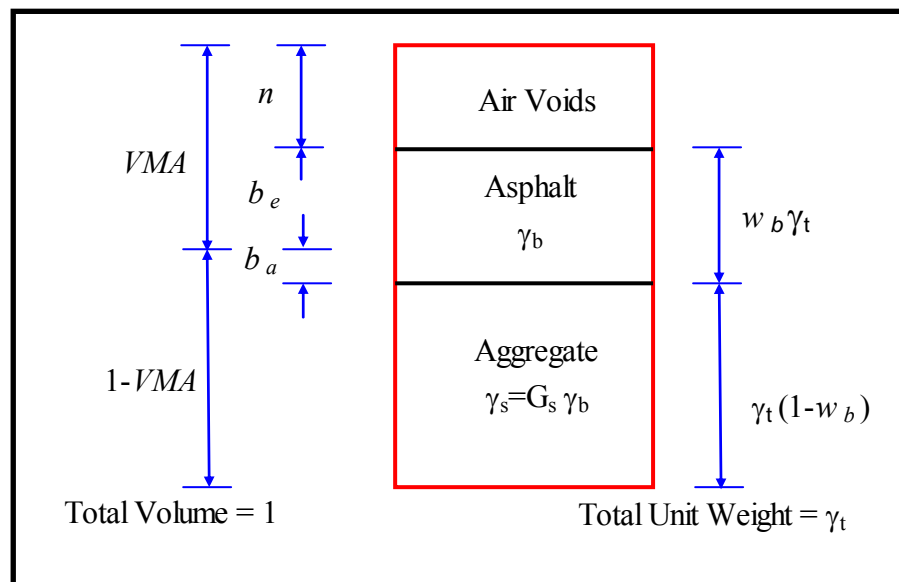
Fig. 4.19. Representation of volumes in a compacted asphalt specimen

This figure can be used in estimating the effective average diameter of particles of asphalt mix ($D_{Effective}$). From Fig. 4.19, it can be noted that D_s corresponds to a volume of the aggregate and the absorbed asphalt (1-VMA) while $D_{Effective}$ corresponds to the volume of the aggregate and both absorbed and effective asphalt [(1-VMA)+b_e]. Then the ratio between D_s and $D_{Effective}$ can be written in the following form:

$$\left(\frac{D_{Effective}}{D_S}\right)^3 = \left(\frac{(1-VMA)+b_e}{(1-VMA)}\right) \tag{4.5}$$

or:

$$D_{Effective} = D_s \left(\frac{(1-VMA)+b_e}{(1-VMA)}\right)^{\frac{1}{3}} \tag{4.6}$$

The volume of the non-absorbed asphalt (b_e) can be written as follows:

$$b_e = w_b \left(\frac{\gamma_t}{\gamma_b}\right) \tag{4.7}$$

Also, from Fig. 4.19, the term (1-VMA) can be replaced with another term as shown in Eq. (4.8).

$$(1-VMA) = \frac{\gamma_t (1-w_b)}{G_s \gamma_b} \tag{4.8}$$

Substituting Eqs. (4.7) and (4.8) in Eq. (4.6), the following expression for $D_{Effective}$ can be found.

$$D_{Effective} = D_s \left(1 + \frac{G_s w_b}{(1-w_b)}\right)^{\frac{1}{3}} \tag{4.9}$$

The final form of Eq. (4.4) that accounts for the effect of asphalt content is then shown in Eq. (4.10).

$$k = \frac{Cn_a{}^3}{(1-n_a)^2}\left[D_s\left(1+\frac{G_s w_b}{(1-w_b)}\right)^{\frac{1}{3}}\right]^2 \frac{\gamma}{\mu} \tag{4.10}$$

As shown in Eq. (4.4), permeability is expected to increase as D_s increases, and since $D_{Effective}$ is proportional to D_s, Eq. (4.9), then permeability is also expected to increase as $D_{Effective}$ increases; this is shown in Eq. (4.10).

The other factor that affects the permeability of HMA mixes is the specimen saturation level during the test. The different permeability models discussed in Chapter II also assume full saturation of the material being tested. Although the permeability procedures in the constant-head or falling-head permeameters assume complete saturation for the tested specimen during the test, some of the tests do not check for saturation. Therefore, the effect of the saturation level should be studied in order to be able to compare measured to calculated permeability results.

Degree of saturation (ψ) is defined as the percent of the void space that is filled with water. Fredlund and Rahardjo (1993) pointed out that when the material is partially saturated, then air is occupying part of the pores volume and water is occupying the rest of the pores volume. This will force the water to flow in smaller pores volume with more tortuous flow paths. Permeability is highly affected by the change in degree of saturation

level, and therefore, permeability is often described as a singular function of ψ. Fredlund and Rahardjo (1993) had suggested the following form for this singular function.

$$k = k_s \left(\psi_e \right)^\delta \tag{4.11}$$

In Eq. (4.11), k is the coefficient of permeability at any saturation level while k_s is its value at fully saturated level. ψ_e is the percent effective saturation level, which can be defined as shown in Eq. (4.12), where ψ_r is the percent residual degree of saturation, which can be defined as the degree of saturation at which an increase in the matric suction will not produce a significant decrease in degree of saturation. δ in Eq. (4.11) is an empirical constant.

$$\psi_e = \frac{\psi - \psi_r}{100 - \psi_r} \tag{4.12}$$

Wyckoff and Botset (1936) had studied the ratio of the permeability of water at a specified degree of saturation (k) to its value at fully saturated level (k_s), and they found that permeability depends on the degree of saturation (ψ) of the sample during the test. They used the experimental values for k and k_s to plot a figure that has the same trend shown in Fig. 4.20. This figure shows that the ratio (k/k_s) is negligible up to a threshold value for ψ, which ranges from 10% to 20%. Then, this ratio increases steeply with increasing ψ to a maximum of 1.0 at 100% saturation level.
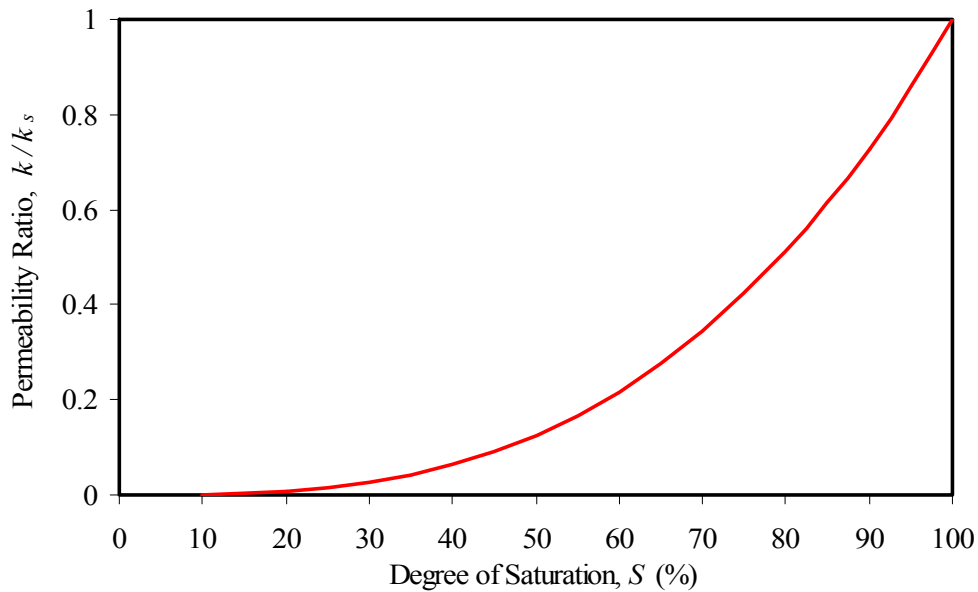
Fig. 4.20. Effect of the degree of saturation (S) on the permeability ratio (k/k_s)

Irmay (1954) had studied the permeability of unsaturated soils and had derived the ratio for k/k_s that is shown in Eq. (4.13). This equation is equivalent to Eq. (4.11) with a value for the empirical constant (δ) is equal to 3 and where the residual degree of saturation (ψ_r) was defined by Irmay (1954) as the part of the voids which is filled with dead water (ψ_o).

$$\frac{k}{k_s} = \left(\frac{\psi - \psi_\circ}{100 - \psi_\circ} \right)^3 \tag{4.13}$$

From the previous discussion, it can be seen that permeability is affected by both asphalt content and degree of saturation of the sample during the test. The effect of the asphalt content is accounted for by using the effective average diameter ($D_{Effective}$) in the

permeability model, as shown in Eq. (4.10). This is not the case for the effect of the degree of saturation on permeability due to the lack of the data on the saturation level of the HMA specimens used in this study. Therefore, it was decided to include the effect of shape factor C and saturation in one coefficient that will be determined by fitting Eq. (4.14) to permeability measurements on a wide range of HMA mixes. The coefficient $\overline{C}$ in Eq. (4.14) accounts for level of saturation, air void shape, and the method used to measure permeability.

$$k = \overline{C} \frac{n_a{}^3}{(1-n_a)^2} \left[D_s \left(1 + \frac{G_s w_b}{(1-w_b)} \right)^{\frac{1}{3}} \right]^2 \frac{\gamma}{\mu} \qquad (4.14)$$
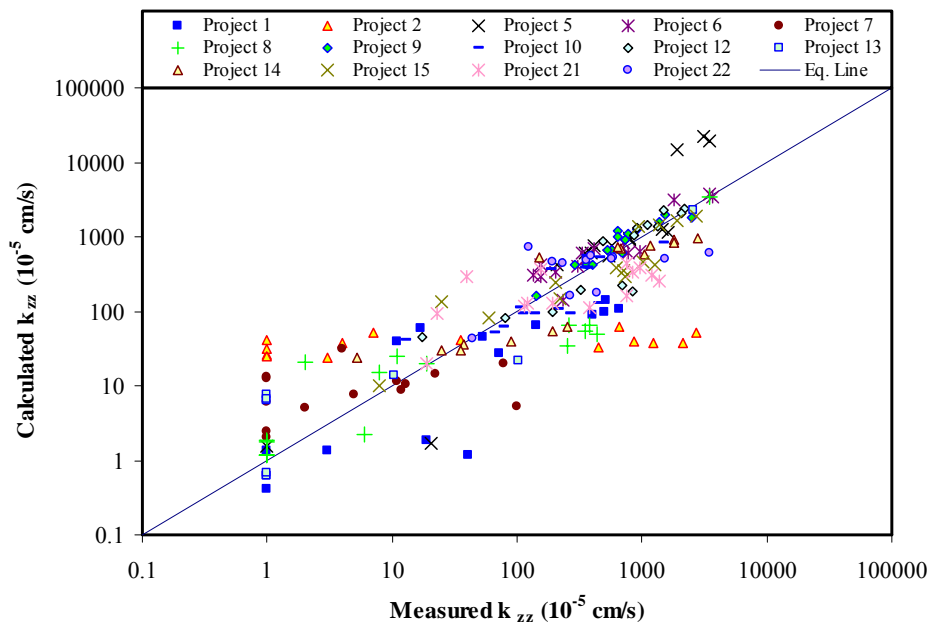
Fig. 4.21. Calculated permeability, Eq. (4.14), vs. laboratory measurements for the data from Cooley et al. (2002a)
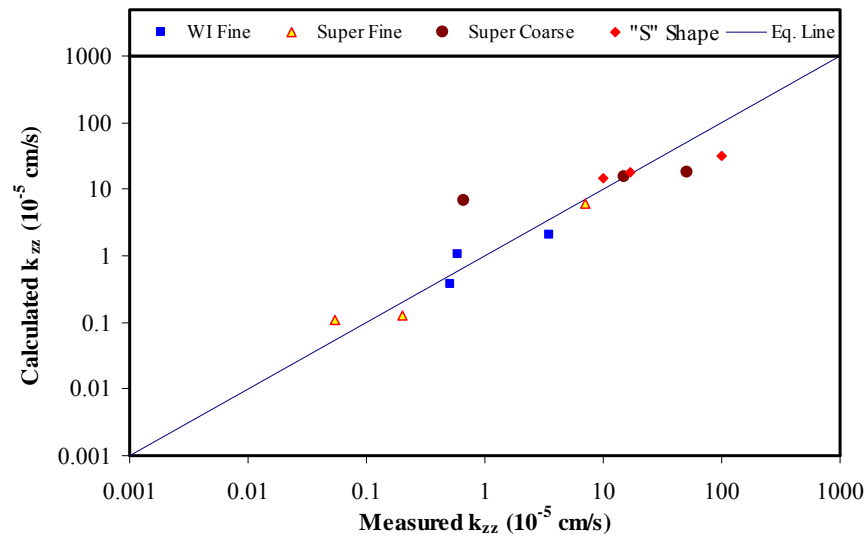
Fig. 4.22. Calculated permeability, Eq. (4.14), vs. laboratory measurements for the data from Kanitpong et al. (2001)
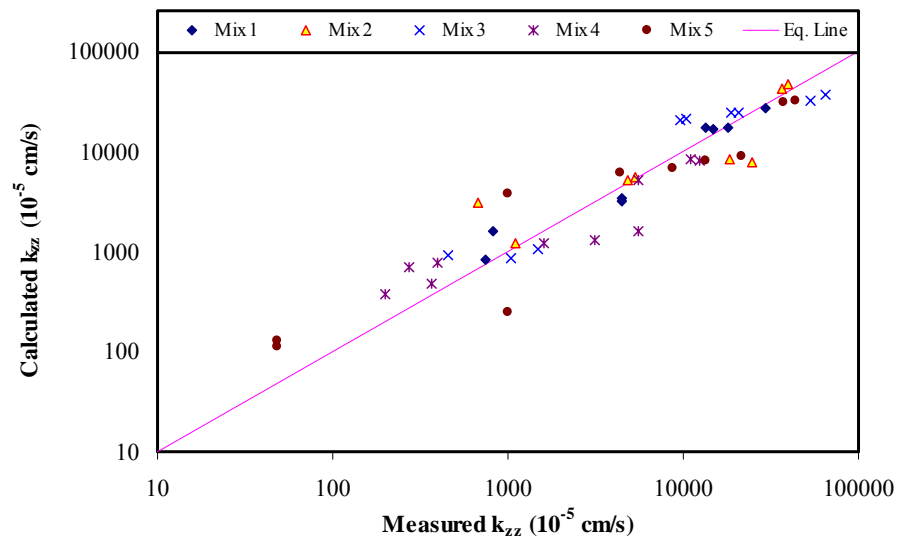
Fig. 4.23. Calculated permeability, Eq. (4.14), vs. laboratory measurements for the data from Maupin (2000)

Figs. 4.21, 4.22, and 4.23 show Eq. (4.14) fitted for the laboratory data from Cooley et al. (2002a), Kanitpong et al. (2001), and Maupin (2000), respectively. The gradation of the mixes from Choubane et al. (1998) were not available, which prevented fitting Eq. (4.14) for these mixes. Figs. 4.24 and 4.25, on the other hand, show Eq. (4.14) fitted for the field data from Cooley et al. (2002a) and Mallick et al. (2001), respectively.

The parameter $\overline{C}$ was fitted for each of the data sets. It was noted that better results can be obtained if different $\overline{C}$ values were used for different percent air void categories. Therefore, the $\overline{C}$ values were chosen such that each permeability device has $\overline{C}$ values depending of the percent air voids. This is an interesting finding given that the different devices were also found to have different m-values in Eq. (4.3). In other words, there is an interaction effect between the measuring device and the percent air voids. This can be due to the effect of percent of air voids on the level of saturation that can be achieved using a certain test method. This interaction is shown in the m-value in Eq. (4.3) and $\overline{C}$ in Eq. (4.14). Previous studies have shown that air voids around 6 to 7% are mostly not connected, and the rate of moisture entry is low. However, complete saturation could happen at percent air voids between 7 and 13% (Pavement Work Tips 1999). The average values for $\overline{C}$ at different percent air voids are shown in Table 4.4.
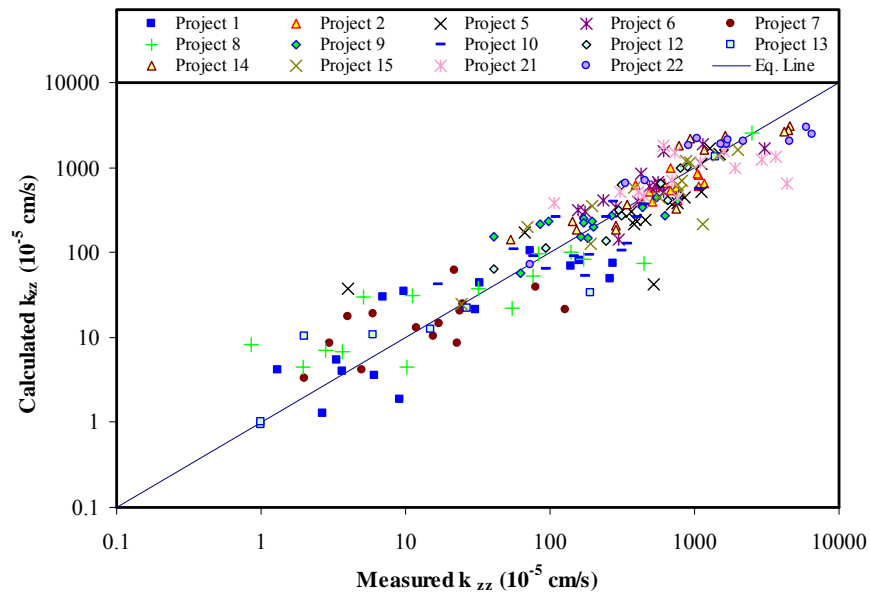
Fig. 4.24. Calculated permeability, Eq. (4.14), vs. field measurements for the data from

Cooley et al. (2002a)
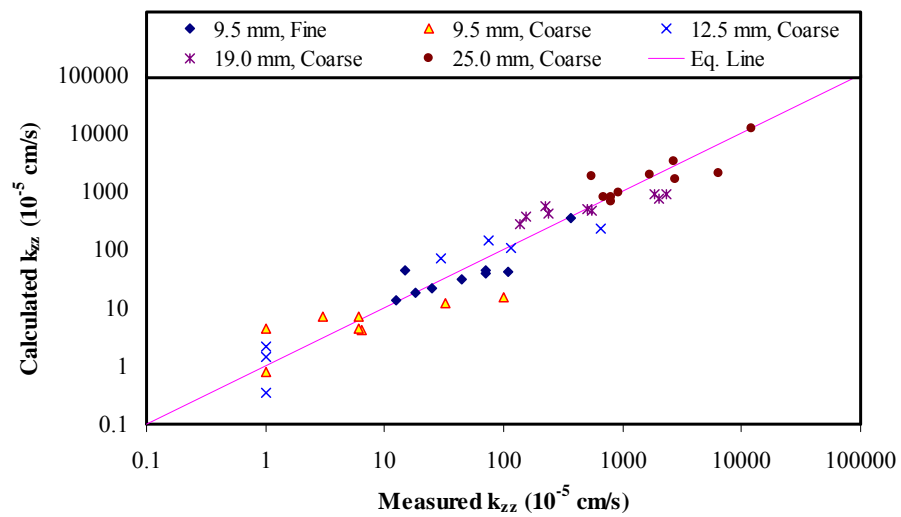
Fig. 4.25. Calculated permeability, Eq. (4.14), vs. field measurements for the data from

Mallick et al. (2001)

Table 4.4. Average Values and Standard Deviation of $\overline{C}$ in Eq. (4.14) for Different Permeability Measurements and Devices

	Device	Reference	% AV Category	$\overline{C}$ Average
Laboratory Measurements	ASTM D5084	Kanitpong et al. (2001)	$n \leq 5$	1.11E-06
			$5 < n \leq 9$	7.25E-06
	Florida DOT	Cooley et al. (2002a)	$n \leq 5$	1.80E-05
			$5 < n \leq 9$	7.86E-05
			$n > 9$	2.41E-04
		Maupin (2000)	$5 < n \leq 9$	2.87E-04
			$9 < n \leq 13$	7.76E-04
			$n > 13$	1.94E-03
Field Measurements	NCAT	Cooley et al. (2002a)	$n \leq 5$	5.02E-05
			$5 < n \leq 9$	9.91E-05
			$n > 9$	1.29E-04
		Mallick et al. (2001)	$n \leq 5$	2.41E-04
			$5 < n \leq 9$	1.55E-04
			$n > 9$	7.02E-04

Similar to the analysis that was done on the factors affecting the *m*-value in Eq. (4.3), the effect of measurement types (laboratory vs. field measurements) and permeability devices on the value of $\overline{C}$ was investigated. For the laboratory measurements, and at the same percent air void level, the average $\overline{C}$ values for the ASTM D5084 constant-head and Florida DOT falling-head laboratory devices were different. This can be attributed to the different procedures used in these devices in which different ways to control the lateral leakage and to ensure the specimen saturation during the test are presented. Even for the same device, $\overline{C}$ values fitted for the data from Cooley et al. (2002a) differed from

the values for the data from Maupin (2000). This can be attributed to the use of field cores in the study by Cooley et al. (2002a), while SGC mixes were used in the study by Maupin (2000).

The constant-head permeameter has a lower average $\overline{C}$ value than the Florida DOT falling-head permeameter at the same porosity range. The constant-head permeameter used by Kanitpong et al. (2001) has better control on the level and consistency of the degree of saturation during testing compared to the Florida DOT falling-head permeameter used in the studies by Maupin (2000) and Cooley et al. (2002a) (Kanitpong et al. 2001). Therefore, the effect of the degree of saturation in the constant-head permeameter is less than in the falling-head permeameter. So, it is expected for the constant-head permeameter to have a lower $\overline{C}$ value. The $\overline{C}$ values for the measurements by Cooley et al. (2002a) and Mallick et al. (2001) were different. This can be due to the modification done by Mallick et al. (2001) on the field permeameter used by Cooley et al. (2002a). For the same permeability device, Table 4.4 shows a general trend of an increase in the $\overline{C}$ value with an increase in percent air void.

Summary

This chapter presented the development of equations for predicting HMA permeability using the HMA mixes presented in Chapter III. Reasonable correlation was obtained between HMA permeability and HMA microstructure characteristics quantified using X-ray CT and image analysis techniques. This encouraged efforts to develop two

equations, based on the Kozeny-Carman equation, to relate HMA permeability to mix properties that can be measured in the laboratory (percent air voids and aggregate size distribution). Both equations included an empirical fitting coefficient to account for the deviation of the experimental conditions from the assumptions used in deriving the Kozeny-Carman equation. The Kozeny-Carman equation assumes all air voids to be cylindrical tubes, fully saturated, and connected. However, air voids in HMA specimens have irregular shapes, most test methods do not check for the saturation level, and only some air voids are connected.

In both of the developed equations, it was found that the fitting coefficient varies with the test method and has an interaction effect with percent air voids. This can be attributed to differences in test methods in controlling the saturation of HMA specimens and the influence of percent air voids on the level of saturation that can be achieved using a certain permeability testing device. One of the developed equations accounted for the asphalt content through using an equivalent particle size in the Kozeny-Carman equation. The developed equations can be calibrated for each test method and the range of percent voids encountered in HMA specimens to predict permeability based on mix volumetrics.

CHAPTER V

NUMERICAL SIMULATION OF FLUID FLOW IN 3-D MICROSTRUCTURES[*]

Introduction

A numerical scheme is developed in this chapter to simulate fluid flow in 3-D microstructures. The governing equations for steady incompressible fluid flow are solved using the Semi-Implicit Method for Pressure-Linked Equations (SIMPLE) finite difference scheme within a non-staggered grid system that represents the 3-D microstructure. This system allows solving of the governing equations using only one computational cell. The numerical scheme is verified through simulating fluid flow in some idealized 3-D microstructures with known closed-form solutions for permeability.

Formulation and Boundary Conditions of Finite Difference Model

A finite difference program is developed to simulate incompressible fluid flow in 3-D porous microstructures. The velocity fields within the microstructure is assumed to be driven only by pressure difference ($\Delta P = P_{inlet} - P_{outlet}$) between the inlet ($P_{inlet}$) and outlet ($P_{outlet}$) of this microstructure. The governing equations for the 3-D steady incompressible fluid flow are:

a) The continuity equation:

---

[*] Part of this chapter is reprinted with permission from "Three dimensional simulation of fluid flow in X-ray CT images of porous media." by Al-Omari, A., and Masad, E. (2004). *International Journal for Numerical and Analytical Methods in Geomechanics*, 28(13), 1327-1360. © 2004 John Wiley & Sons, Ltd.

$$\frac{\partial \rho u}{\partial x} + \frac{\partial \rho v}{\partial y} + \frac{\partial \rho w}{\partial z} = 0 \tag{5.1}$$

b) The momentum equations in conservative form:

$$\frac{\partial}{\partial x}\left(\rho uu - \mu \frac{\partial u}{\partial x}\right) + \frac{\partial}{\partial y}\left(\rho uv - \mu \frac{\partial u}{\partial y}\right) + \frac{\partial}{\partial z}\left(\rho uw - \mu \frac{\partial u}{\partial z}\right)$$

$$= -\frac{\partial P}{\partial x} + \frac{\partial}{\partial x}\left(\mu \frac{\partial u}{\partial x}\right) + \frac{\partial}{\partial y}\left(\mu \frac{\partial v}{\partial x}\right) + \frac{\partial}{\partial z}\left(\mu \frac{\partial w}{\partial x}\right) \tag{5.2}$$

$$\frac{\partial}{\partial y}\left(\rho vv - \mu \frac{\partial v}{\partial y}\right) + \frac{\partial}{\partial x}\left(\rho vu - \mu \frac{\partial v}{\partial x}\right) + \frac{\partial}{\partial z}\left(\rho vw - \mu \frac{\partial v}{\partial z}\right)$$

$$= -\frac{\partial P}{\partial y} + \frac{\partial}{\partial y}\left(\mu \frac{\partial v}{\partial y}\right) + \frac{\partial}{\partial x}\left(\mu \frac{\partial u}{\partial y}\right) + \frac{\partial}{\partial z}\left(\mu \frac{\partial w}{\partial y}\right) \tag{5.3}$$

$$\frac{\partial}{\partial z}\left(\rho ww - \mu \frac{\partial w}{\partial z}\right) + \frac{\partial}{\partial x}\left(\rho wu - \mu \frac{\partial w}{\partial x}\right) + \frac{\partial}{\partial y}\left(\rho wv - \mu \frac{\partial w}{\partial y}\right)$$

$$= -\frac{\partial P}{\partial z} + \frac{\partial}{\partial z}\left(\mu \frac{\partial w}{\partial z}\right) + \frac{\partial}{\partial x}\left(\mu \frac{\partial u}{\partial z}\right) + \frac{\partial}{\partial y}\left(\mu \frac{\partial v}{\partial z}\right) \tag{5.4}$$

Eqs. (5.2), (5.3), and (5.4) represent the momentum equations in the x-, y-, and z-directions, respectively.

In the continuity and momentum equations, u, v, and w are velocity components in the x-, y-, and z-directions, respectively. P represents the applied pressure, ρ and μ represent fluid density and viscosity, respectively.

The finite difference model is based on the non-staggered numerical scheme that uses only one cell to solve the governing equations: the continuity and momentum equations.

This is achieved by integrating the governing equations over the control volume. An illustration of the non-staggered cell arrangement, which includes the control volume that will be used in developing this finite difference solution as well as the corresponding adopted coordinate system, are shown in Fig. 5.1.
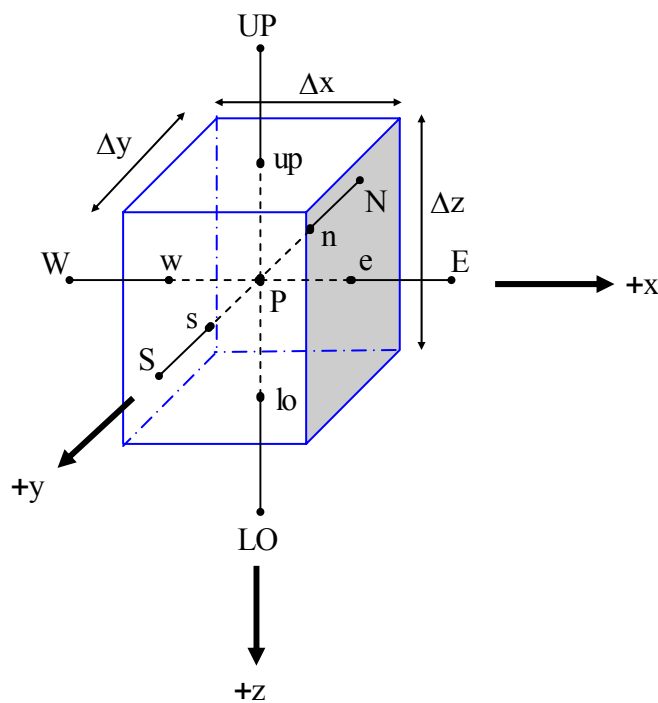
Fig. 5.1. Illustration of the non-staggered cell arrangement; control volume and the adopted coordinate system

In Fig. 5.1, the points in capital letters (P, E, W, S, N, LO, and UP) are the nodal points for the current, eastern, western, southern, northern, lower, and upper cells, respectively.

The edges of the current cell are presented by the lowercase letters. The eastern, western, southern, northern, lower, and upper edges are presented by e, w, s, n, lo, and up, respectively. Cell dimensions Δx, Δy, and Δz are in the x-, y-, and z-directions, respectively. These dimensions are shown in Fig. 5.1, where the positive x-, y-, and z-directions are defined in the directions of eastern, southern, and lower directions, respectively.

The continuity equation, Eq. (5.1), is integrated over the control volume to get:

$$\rho u_e \Delta y \Delta z - \rho u_w \Delta y \Delta z + \rho v_s \Delta x \Delta z - \rho v_n \Delta x \Delta z + \rho w_{lo} \Delta x \Delta y - \rho w_{up} \Delta x \Delta y = 0 \qquad (5.5)$$

The mass flux G_i for the edge i of the current cell is defined in Eq. (5.6) as follows:

$$\begin{aligned}
G_e &= \rho u_e \Delta y \Delta z,\, G_w = \rho u_w \Delta y \Delta z,\, G_s = \rho v_s \Delta x \Delta z, \\
G_n &= \rho v_n \Delta x \Delta z,\, G_{lo} = \rho w_{lo} \Delta x \Delta y,\, G_{up} = \rho w_{up} \Delta x \Delta y
\end{aligned} \qquad (5.6)$$

Then, the continuity equation becomes:

$$G_e - G_w + G_s - G_n + G_{lo} - G_{up} = 0 \qquad (5.7)$$

The momentum equations are also integrated over the same control volume. Integrating the momentum equation in the x-direction, for example, will result in the following equation:

$$\begin{aligned}
&\left(\rho uu - \mu \frac{\partial u}{\partial x} \right)_e \Delta y\, \Delta z - \left(\rho uu - \mu \frac{\partial u}{\partial x} \right)_w \Delta y\, \Delta z \\
&+ \left(\rho uv - \mu \frac{\partial u}{\partial y} \right)_s \Delta x\, \Delta z - \left(\rho uv - \mu \frac{\partial u}{\partial y} \right)_n \Delta x\, \Delta z \\
&+ \left(\rho uw - \mu \frac{\partial u}{\partial z} \right)_{lo} \Delta x\, \Delta y - \left(\rho uw - \mu \frac{\partial u}{\partial z} \right)_{up} \Delta x\, \Delta y
\end{aligned}$$

$$= (P_w - P_e)\Delta y\,\Delta z + \left(\mu\frac{\partial u}{\partial x}\bigg|_e - \mu\frac{\partial u}{\partial x}\bigg|_w \right)\Delta y\,\Delta z$$

$$+ \left(\mu\frac{\partial v}{\partial x}\bigg|_s - \mu\frac{\partial v}{\partial x}\bigg|_n \right)\Delta x\,\Delta z + \left(\mu\frac{\partial w}{\partial x}\bigg|_{lo} - \mu\frac{\partial w}{\partial x}\bigg|_{up} \right)\Delta x\,\Delta y \qquad (5.8)$$

Let the interpolated pressures on the cell faces, P_e and P_w, be defined as follows:

$$P_e = \frac{P_E + P_P}{2}, P_w = \frac{P_W + P_P}{2} \qquad (5.9)$$

then:

$$P_w - P_e = \frac{P_W - P_E}{2} \qquad (5.10)$$

A method for solving the momentum equations for laminar flow problems has been developed by Patankar and Spalding (1970). They introduced an algorithm to iteratively solve the momentum equations. This algorithm is called the SIMPLE. Using this algorithm, expressions for the velocities in x-, y-, and z-directions (u, v, and w, respectively) can be obtained as described below.

Define the momentum flux in the x-direction on the eastern edge M_e^x as follows:

$$M_e^x = G_e u - \mu\frac{\partial u}{\partial x}\bigg|_e \Delta y\Delta z \qquad (5.11)$$

and since u is a function of x only, then the partial derivative is converted to the total derivative as follows:

$$M_e^x = G_e u - \mu \frac{du}{dx} \Delta y \Delta z \tag{5.12}$$

or:

$$\frac{du}{dx} = \left(\frac{G_e u}{\mu \Delta y \Delta z} \right) - \frac{M_e^x}{\mu \Delta y \Delta z} \quad = \frac{u - \dfrac{M_e^x}{G_e}}{\mu \Delta y \Delta z / G_e} \tag{5.13}$$

rearranging Eq. (5.13):

$$\frac{du / dx}{\left[u - \dfrac{M_e^x}{G_e} \right]} = \frac{G_e}{\mu \Delta y \Delta z} \tag{5.14}$$

the left hand side of Eq. (5.14) is the derivative of $\left\{ \ln \left| u - \dfrac{M_e^x}{G_e} \right| \right\}$ with respect to x.

Therefore, Eq. (5.14) can be written as follows:

$$\frac{d}{dx} \ln \left| u - \frac{M_e^x}{G_e} \right| = \frac{G_e}{\mu \Delta y \Delta z} \tag{5.15}$$

Integrating both sides of Eq. (5.15), we get:

$$\ln \left| u - \frac{M_e^x}{G_e} \right| = \frac{G_e x}{\mu \Delta y \Delta z} + C_1 \tag{5.16}$$

Taking the natural exponential of both sides of Eq. (5.16):

$$u - \frac{M_e^x}{G_e} = \exp \left[\frac{G_e x}{\mu \Delta y \Delta z} + C_1 \right] = \exp \left[\frac{G_e x}{\mu \Delta y \Delta z} \right] \exp [C_1] \tag{5.17}$$

where C_1 is constant. Also, exp $[C_1]$ is constant and can be replaced by another constant, C. Eq. (5.17) can be reduced to:

$$u - \frac{M_e^x}{G_e} = C \exp\left[\frac{G_e x}{\mu \Delta y \Delta z}\right] \tag{5.18}$$

or:
$$u = \frac{M_e^x}{G_e} + C \exp\left[\frac{G_e x}{\mu \Delta y \Delta z}\right] \tag{5.19}$$

in order to calculate the value of the integration constant C; it is known that at $x = 0$ the velocity u is equal to u_P. Applying this condition to Eq. (5.19), we get:

$$u = \frac{M_e^x}{G_e} + C = u_P \tag{5.20}$$

or:
$$C = u_P - \frac{M_e^x}{G_e} \tag{5.21}$$

and by substituting the value of the integration constant C from Eq. (5.21) into Eq. (5.19), the following expression for u will be reached:

$$u = \frac{M_e^x}{G_e} + u_P \exp\left[\frac{G_e x}{\mu \Delta y \Delta z}\right] - \frac{M_e^x}{G_e} \exp\left[\frac{G_e x}{\mu \Delta y \Delta z}\right] \tag{5.22}$$

or:
$$u = \frac{M_e^x}{G_e}\left[1 - \exp\left(\frac{G_e x}{\mu \Delta y \Delta z}\right)\right] + u_P \exp\left(\frac{G_e x}{\mu \Delta y \Delta z}\right) \tag{5.23}$$

Eq. (5.23) can be written in the following form:

$$M_e^x = G_e \frac{u - u_P \exp\left(\dfrac{G_e x}{\mu \Delta y \Delta z}\right)}{1 - \exp\left(\dfrac{G_e x}{\mu \Delta y \Delta z}\right)} \tag{5.24}$$

The velocity value at a distance Δx is equal to u_E; therefore, Eq. (5.24) can be written as follows:

$$M_e^x = G_e \frac{u_E - u_P \exp\left(\dfrac{G_e \Delta x}{\mu \Delta y \Delta z}\right)}{1 - \exp\left(\dfrac{G_e \Delta x}{\mu \Delta y \Delta z}\right)} \tag{5.25}$$

or:
$$M_e^x = G_e \frac{u_E - u_P e^{\text{Re}_c}}{1 - e^{\text{Re}_c}} \tag{5.26}$$

where Re_c is the cell Reynolds number, which can be defined as follows:

$$\text{Re}_c = \frac{G_e \Delta x}{\mu \Delta y \Delta z} = \frac{\rho u_e \Delta x \Delta y \Delta z}{\mu \Delta y \Delta z} = \frac{\rho u_e \Delta x}{\mu} \tag{5.27}$$

If $\left|\text{Re}_c\right|$ is much greater than unity, then the viscous forces are insignificant, and all momentum is transferred by convectional (inertial) forces. From Eq. (5.26), if $\text{Re}_c \gg 1.0$, then the following approximation for M_e^x is valid, $M_e^x = G_e u_P$. If $\text{Re}_c \ll -1.0$, then M_e^x can be approximated as follows: $M_e^x = u_E G_e$. This formulation is upwind differencing (Crowe 1997).

On the other hand, if Re_c is much less than unity, $\left|\text{Re}_c\right| \ll 1.0$, then the viscous forces overcome the inertial forces, and the momentum flux M_e^x becomes:

$$M_e^x = G_e \left[\frac{u_P + u_E}{2}\right] - \frac{\mu \Delta y \Delta z}{\Delta x}(u_E - u_P) \tag{5.28}$$

where Eq. (5.28) is the central difference formulation (Crowe 1997). Rearranging the different terms of Eq. (5.28):

$$M_e^x = G_e \left[\frac{u_E}{2} - \frac{\mu u_E \Delta y \Delta z}{G_e \Delta x} + \frac{u_P}{2} + \frac{\mu u_P \Delta y \Delta z}{G_e \Delta x} \right] \qquad (5.29)$$

and simplifying Eq. (5.29) we get:

$$M_e^x = G_e \left[\left(\frac{1}{2} - \frac{\mu \Delta y \Delta z}{G_e \Delta x} \right) u_E + \left(\frac{1}{2} + \frac{\mu \Delta y \Delta z}{G_e \Delta x} \right) u_P \right] \qquad (5.30)$$

or:
$$M_e^x = G_e \left[\left(\frac{1}{2} - \frac{\mu \Delta y \Delta z}{G_e \Delta x} \right) u_E + \left(1 - \left\{ \frac{1}{2} - \frac{\mu \Delta y \Delta z}{G_e \Delta x} \right\} \right) u_P \right] \qquad (5.31)$$

Now, define f_e as follows:

$$f_e = \frac{1}{2} - \frac{\mu \Delta y \Delta z}{G_e \Delta x} \qquad (5.32)$$

and then, Eq. (5.28) can be expressed as:

$$M_e^x = G_e \left[f_e u_E + (1 - f_e) u_P \right] \qquad (5.33)$$

The hybrid difference formulation suggests the use of the central and upwind differencing formulations as follows. For $|R_e| \ll 2.0$, Eq. (5.33) can be used as the central difference formulation, and the values for f_e will be:

$$f_e = \frac{1}{2} - \frac{\mu \Delta y \Delta z}{G_e \Delta x} = \frac{1}{2} - \frac{\mu}{\rho u_e \Delta x} = \frac{1}{2} - \frac{1}{\text{Re}_c} \qquad (5.34)$$

whereas for $|\text{Re}_c| \gg 2.0$, Eq. (5.33) can be used as the upwind difference formulation where $f_e=0$ for $G_e \geq 0$ or $f_e=1$ for $G_e<0$.

The momentum Eq. (5.8) can then be expressed using the definition of momentum flux as follows:

$$M_e^x - M_w^x + M_s^x - M_n^x + M_{lo}^x - M_{up}^x = \left(\frac{P_W - P_E}{2}\right)\Delta y\,\Delta z +$$

$$\left(\mu\frac{\partial u}{\partial x}\bigg|_e - \mu\frac{\partial u}{\partial x}\bigg|_w\right)\Delta y\Delta z + \left(\mu\frac{\partial v}{\partial x}\bigg|_s - \mu\frac{\partial v}{\partial x}\bigg|_n\right)\Delta x\Delta z + \left(\mu\frac{\partial w}{\partial x}\bigg|_{lo} - \mu\frac{\partial w}{\partial x}\bigg|_{up}\right)\Delta x\Delta y \quad (5.35)$$

and it can be simplified furthermore using the mass flux definition and adding a term that accounts for the non-uniformity of the viscosity, S_{visc}. If the viscosity is uniform and the flow is incompressible, then this term is zero.

$$G_e\left[f_e u_E + (1 - f_e)u_P\right] - G_w\left[f_w u_W + (1 - f_w)u_P\right]$$
$$+ G_s\left[f_s u_S + (1 - f_s)u_P\right] - G_n\left[f_n u_N + (1 - f_n)u_P\right]$$
$$+ G_{lo}\left[f_{lo} u_{LO} + (1 - f_{lo})u_P\right] - G_{up}\left[f_{up} u_{UP} + (1 - f_{up})u_P\right]$$

$$= \left(\frac{P_W - P_E}{2}\right)\Delta y\Delta z + S_{visc} \quad (5.36)$$

and rearranging the terms, Eq. (5.36) becomes:

$$(G_e - G_w + G_s - G_n + G_{lo} - G_{up})u_P +$$
$$(-G_e f_e + G_w f_w - G_s f_s + G_n f_n - G_{lo} f_{lo} + G_{up} f_{up})u_P$$
$$+ f_e G_e u_E - f_w G_w u_W + f_s G_s u_S - f_n G_n u_N + f_{lo} G_{lo} u_{LO} - f_{up} G_{up} U_{UP}$$

$$= \left(\frac{P_W - P_E}{2}\right)\Delta y\Delta z + S_{visc} \quad (5.37)$$

Note that $(G_e-G_w+G_s-G_n+G_{lo}-G_{up})$ is identically zero complying with the continuity equation; also, define the coefficients of velocities a_i for each face i of the control volume as follows:

$$a_e = -G_e f_e, \, a_w = +G_w f_w,$$

$$a_s = -G_s f_s, \, a_n = +G_n f_n, \quad (5.38)$$

$$a_{lo} = -G_{lo} f_{lo}, \, a_{up} = +G_{up} f_{up}$$

Eq. (5.37) can then be written in the following form:

$$(a_e + a_w + a_s + a_n + a_{lo} + a_{up})u_p - a_e u_E - a_w u_W - a_s u_S - a_n u_N - a_{lo} u_{LO} - a_{up} u_{UP}$$

$$= \left(\frac{P_W - P_E}{2}\right)\Delta y \Delta z + S_{visc} \quad (5.39)$$

or:
$$u_P \left(\sum_{i=n,s,e,w,lo,up} a_i\right) = \sum_{\substack{i=n,s,e,w,lo,up \\ j=N,S,E,W,LO,UP}} a_i u_j + \left(\frac{P_W - P_E}{2}\right)\Delta y \Delta z + S_{visc} \quad (5.40)$$

An additional term, $S_P u_P$, is added to Eq. (5.40), which is a function of the boundary conditions. Eq. (5.39) can be written as:

$$u_P \left(\sum_{i=n,s,e,w,lo,up} a_i\right) = \sum_{\substack{i=n,s,e,w,lo,up \\ j=N,S,E,W,LO,UP}} a_i u_j + S_P u_P + \left(\frac{P_W - P_E}{2}\right)\Delta y \Delta z + S_{visc} \quad (5.41)$$

arranging the terms:

$$u_P \left(\sum_{i=n,s,e,w,lo,up} a_i - S_P\right) = \sum_{\substack{i=n,s,e,w,lo,up \\ j=N,S,E,W,LO,UP}} a_i u_j + \left(\frac{P_W - P_E}{2}\right)\Delta y \Delta z + S_{visc} \quad (5.42)$$

and finally, u_P can be expressed as follows:

$$u_P = \frac{\displaystyle\sum_{\substack{i=n,s,e,w,lo,up \\ j=N,S,E,W,LO,UP}} a_i u_j + \left(\frac{P_W - P_E}{2}\right)\Delta y \Delta z + S_{visc}}{\left(\displaystyle\sum_{i=n,s,e,w,lo,up} a_i - S_P\right)} \quad (5.43)$$

let:
$$a_P = (\sum_{i=n,s,e,w,lo,up} a_i - S_P) \tag{5.44}$$

and then, the nodal velocity in the x-direction u_P can be calculated as follows:

$$u_P = \frac{\sum\limits_{\substack{i=n,s,e,w,lo,up \\ j=N,S,E,W,LO,UP}} a_i u_j + \left(\dfrac{P_W - P_E}{2}\right)\Delta y \Delta z + S_{visc}}{a_P} \tag{5.45}$$

Similar expressions for the other two nodal velocities, v_P and w_P, in the y- and z-directions, respectively, can be derived from integrating the momentum equations in the y- and z-directions. These expressions are:

$$v_P = \frac{\sum\limits_{\substack{i=n,s,e,w,lo,up \\ j=N,S,E,W,LO,UP}} a_i v_j + \left(\dfrac{P_N - P_S}{2}\right)\Delta x \Delta z + S_{visc}}{a_P} \tag{5.46}$$

$$w_P = \frac{\sum\limits_{\substack{i=n,s,e,w,lo,up \\ j=N,S,E,W,LO,UP}} a_i w_j + \left(\dfrac{P_{UP} - P_{LO}}{2}\right)\Delta x \Delta y + S_{visc}}{a_P} \tag{5.47}$$

Define the relaxation factor ω as the factor used such that only part of the value calculated in the previous iteration is carried to the next iteration. Eqs. (5.45) through (5.47) can be presented as follows:

$$u_P = (1-\omega)u_P^\circ + \omega \frac{\sum\limits_{\substack{i=n,s,e,w,lo,up \\ j=N,S,E,W,LO,UP}} a_i u_j + \left(\dfrac{P_W - P_E}{2}\right)\Delta y \Delta z + S_{visc}}{a_P} \tag{5.48}$$

$$v_P = (1-\omega)v_P^\circ + \omega \frac{\displaystyle\sum_{\substack{i=n,s,e,w,lo,up \\ j=N,S,E,W,LO,UP}} a_i v_j + \left(\dfrac{P_N - P_S}{2}\right)\Delta x \Delta z + S_{visc}}{a_P} \tag{5.49}$$

$$w_P = (1-\omega)w_P^\circ + \omega \frac{\displaystyle\sum_{\substack{i=n,s,e,w,lo,up \\ j=N,S,E,W,LO,UP}} a_i w_j + \left(\dfrac{P_{UP} - P_{LO}}{2}\right)\Delta x \Delta y + S_{visc}}{a_P} \tag{5.50}$$

where the ($^\circ$) indicates the value obtained from the previous iteration and ω is defined as the relaxation factor, which is the factor used such that only part of the value calculated in the previous iteration is carried to the next iteration. The results of the iterative scheme are sensitive to the value of relaxation factor, especially when the difference between the velocity values in two consecutive iterations is large. A_i's are the coefficients of velocities for each edge i and will be defined subsequently. S_{visc} is an additional term that accounts for the non-uniformity of the viscosity. It has a value of zero for a uniform viscosity and incompressible flow. A_P is defined in Eq. (5.51).

$$a_P = (\sum_{i=n,s,e,w,lo,up} a_i - S_P) \tag{5.51}$$

where the term S_P is a function of the boundary condition. If the computational cell coincides with solid phase, then the value of this function is assigned to a very large negative number. The corresponding a_P will have a very large positive value. This will lead, as will be seen later, to a value of zero for the velocity of the center of this computational cell. Then, the convergence rate of the simulation process is accelerated.

Re_c can be used to determine whether the convective flow or the viscous flow is dominant in the fluid flow. The values of the Re_c are found to be small in this study

($|Re_c| \leq 2$). Therefore, the viscous effect controls fluid flow, and the a_i are calculated as follows:

$$a_e = \mu \frac{\Delta y \Delta z}{\Delta x} - \frac{\rho u_e \Delta y \Delta z}{2} \qquad (5.52)$$

$$a_w = \mu \frac{\Delta y \Delta z}{\Delta x} + \frac{\rho u_w \Delta y \Delta z}{2} \qquad (5.53)$$

$$a_s = \mu \frac{\Delta x \Delta z}{\Delta y} - \frac{\rho v_s \Delta x \Delta z}{2} \qquad (5.54)$$

$$a_n = \mu \frac{\Delta x \Delta z}{\Delta y} + \frac{\rho v_n \Delta x \Delta z}{2} \qquad (5.55)$$

$$a_{lo} = \mu \frac{\Delta x \Delta y}{\Delta z} - \frac{\rho w_{lo} \Delta x \Delta y}{2} \qquad (5.56)$$

$$a_{up} = \mu \frac{\Delta x \Delta y}{\Delta z} + \frac{\rho w_{up} \Delta x \Delta y}{2} \qquad (5.57)$$

As mentioned earlier, the velocity coefficients shown in Eqs. (5.52) through (5.57) were derived using the central difference formulation. As mentioned by Patankar (1980), one of the basic rules that the discretization equation should match up is that all of the velocity coefficients should be positive. This rule is crucial in order to have a realistic and stable solution. This rule restricts these coefficients with a small range of Re_c ($|Re_c| \leq 2$) that keeps all of them positive. The exponential formulation will be used in deriving these coefficients such that they are not restricted by the small value of Re_c.
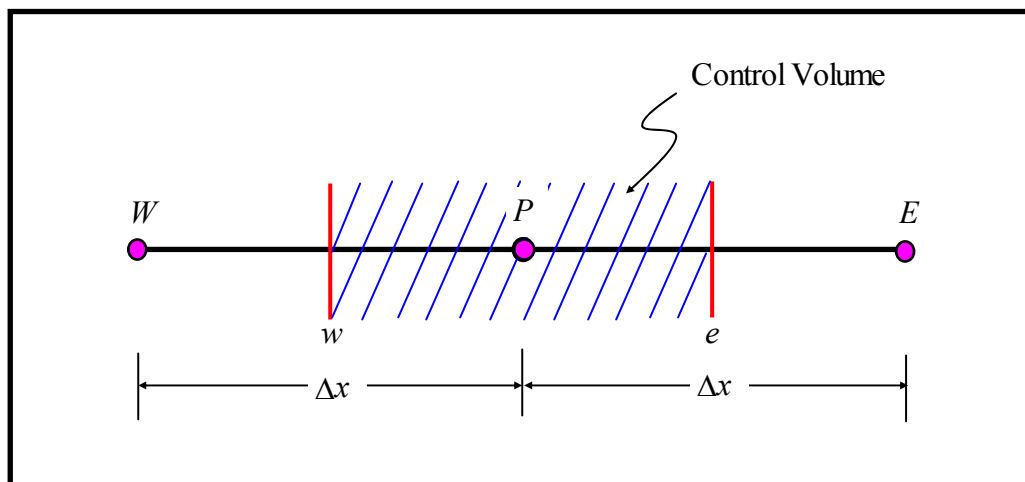
Fig. 5.2. Grid point system for the steady one-dimensional conventional and diffusion problem

Patankar (1980) showed that the governing equation, Eq. (5.58), for steady one-dimensional convection and diffusion with constant viscosity (μ) and constant density (ρ) (Fig. 5.2) can be solved exactly. In Eq. (5.58), u and Δx are the velocity and grid spacing, respectively. If the domain used for this equation is $0 \leq x \leq \Delta x$ where points P and E are at $x = 0$ and $x = \Delta x$, respectively, and the boundary conditions are $u(x = 0) = u_P$ and $u(x = \Delta x) = u_E$, then, the solution for Eq. (5.58) is presented in Eqs. (5.59) and (5.60).

$$\frac{d}{dx}(\rho uu) = \frac{d}{dx}\left(\mu \frac{du}{dx}\right) \tag{5.58}$$

$$u_e = u_P + (u_E - u_P)\frac{exp(\rho u_e x/\mu) - 1}{exp(\rho u_e \Delta x/\mu)} \tag{5.59}$$

$$u_w = u_P + \left(u_P - u_W\right)\frac{exp\left(\rho u_w\, x/\mu\right) - 1}{exp\left(\rho u_w\, \Delta x/\mu\right)} \tag{5.60}$$

Based on Eqs. (5.59) and (5.60), Patankar (1980) derived the velocity coefficients, a_e, a_w, and a_P as shown in Eqs. (5.61), (5.62), and (5.63).

$$a_e = \left(\rho u_e\right)\Big/\left[exp\left(\rho u_e \Delta x/\mu\right) - 1\right] \tag{5.61}$$

$$a_w = \left(\rho u_w\right)exp\left(\rho u_w \Delta x/\mu\right)\Big/\left[exp\left(\rho u_w \Delta x/\mu\right) - 1\right] \tag{5.62}$$

$$a_P = a_e + a_w + \left(\rho u_e - \rho u_w\right) \tag{5.63}$$

For the exponential formulation, as shown in Fig. 5.3, the rule mentioned by Patankar (1980) is always satisfied, and the velocity coefficients are positive for any value of Re_c. Although the exponential formulation has a highly desirable behavior, it has not been widely used. This is due to the fact that it has been regarded as expensive to compute. However, this is not considered a limitation given the high computing power available nowadays. The main advantage of this exponential formulation is in its stability during the solution without the need to check for the value of Re_c. Other stable formulations, such as the hybrid and power-law formulations, require a check to be performed on the Re_c value before choosing an appropriate formula to be used. Therefore, it was decided to use this formulation in deriving the velocity coefficients.
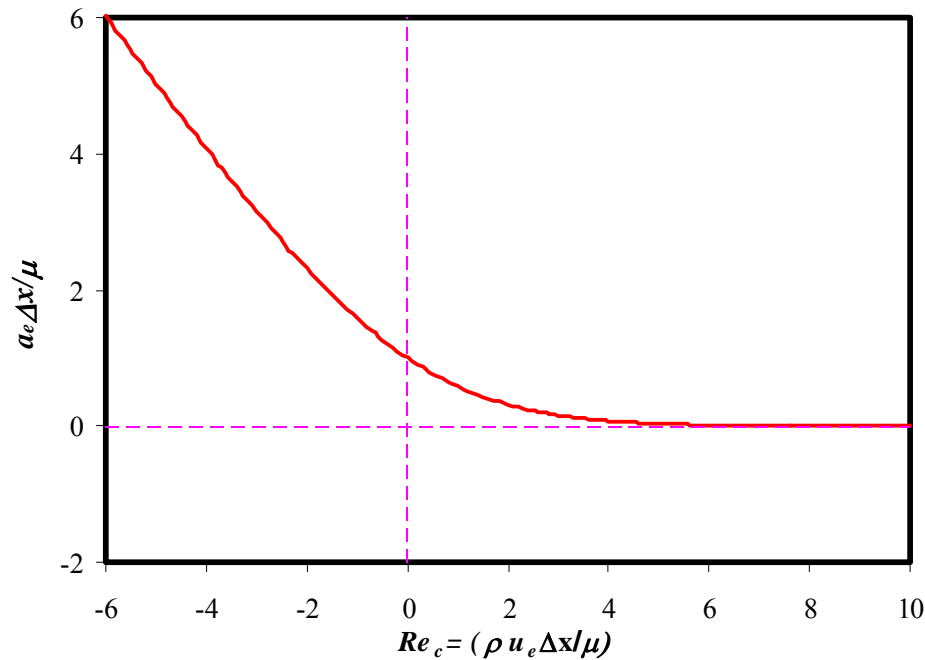
Fig. 5.3. Variation of the coefficient a_e for different values for Re_c in the *x*-direction ($\rho u_e \Delta x/\mu$) using the exponential formulation

Patankar (1980) had used the exponential scheme to derive the velocity coefficients for the 3-D problem. The new velocity coefficients derived by (Patankar 1980) are shown in Eqs. (5.64) through (5.69) where the function *Max (a,b)* denotes the maximum value between *a* and *b*. These equations will replace the velocity coefficients presented by Eqs. (5.52) through (5.57).

$$
a_e = \left(\frac{\left(\dfrac{\mu \Delta y\, \Delta z}{\Delta x} \right) \left| \dfrac{\rho u_e \Delta x}{\mu} \right|}{\exp\left| \dfrac{\rho u_e \Delta x}{\mu} \right| - 1} \right) + Max\ \{-\rho u_e \Delta y\, \Delta z\ , 0\} \tag{5.64}
$$

$$a_w = \left(\frac{\left(\frac{\mu \Delta y\, \Delta z}{\Delta x} \right) \left| \frac{\rho u_w\, \Delta x}{\mu} \right|}{\exp \left| \frac{\rho u_w\, \Delta x}{\mu} \right| - 1} \right) + Max \left\{ + \rho u_w\, \Delta y\, \Delta z\, , 0 \right\} \qquad (5.65)$$

$$a_s = \left(\frac{\left(\frac{\mu \Delta x\, \Delta z}{\Delta y} \right) \left| \frac{\rho v_s\, \Delta y}{\mu} \right|}{\exp \left| \frac{\rho v_s\, \Delta y}{\mu} \right| - 1} \right) + Max \left\{ - \rho v_s\, \Delta x\, \Delta z\, , 0 \right\} \qquad (5.66)$$

$$a_n = \left(\frac{\left(\frac{\mu \Delta x\, \Delta z}{\Delta y} \right) \left| \frac{\rho v_n\, \Delta y}{\mu} \right|}{\exp \left| \frac{\rho v_n\, \Delta y}{\mu} \right| - 1} \right) + Max \left\{ + \rho v_n\, \Delta x\, \Delta z\, , 0 \right\} \qquad (5.67)$$

$$a_{lo} = \left(\frac{\left(\frac{\mu \Delta x\, \Delta y}{\Delta z} \right) \left| \frac{\rho w_{lo}\, \Delta z}{\mu} \right|}{\exp \left| \frac{\rho w_{lo}\, \Delta z}{\mu} \right| - 1} \right) + Max \left\{ - \rho w_{lo}\, \Delta x\, \Delta y\, , 0 \right\} \qquad (5.68)$$

$$a_{up} = \left(\frac{\left(\frac{\mu \Delta x\, \Delta y}{\Delta z} \right) \left| \frac{\rho w_{up}\, \Delta z}{\mu} \right|}{\exp \left| \frac{\rho w_{up}\, \Delta z}{\mu} \right| - 1} \right) + Max \left\{ + \rho w_{up}\, \Delta x\, \Delta y\, , 0 \right\} \qquad (5.69)$$

Using the velocity coefficients shown in Eqs. (5.64) through (5.69) will ensure the stability of the solution for any Re_c value.

For the first iteration of the numerical solution, the initial values for nodal velocities and pressures are assumed. A linear interpolation is used to calculate the velocities at the cell faces as follows:

$$u_e = \left(\frac{u_P + u_E}{2}\right) \quad, \quad u_w = \left(\frac{u_P + u_W}{2}\right) \quad, \quad u_s = \left(\frac{u_P + u_S}{2}\right) \quad,$$

$$u_n = \left(\frac{u_P + u_N}{2}\right) \quad, \quad u_{lo} = \left(\frac{u_P + u_{LO}}{2}\right) \quad, \quad u_{up} = \left(\frac{u_P + u_{UP}}{2}\right) \tag{5.70}$$

Eq. (5.70) is used for the initial velocity values at the cell faces in the first iteration only. For the next iterations, Eq. (5.70) is replaced by another set of equations as will be discussed later in this section.

The velocity at the eastern face can be obtained as follows:

$$u_e = \frac{\overline{\sum a_i u_j}}{a_P^e} + \frac{\Delta y \Delta z}{\overline{a_P^e}}(P_P - P_E) \tag{5.71}$$

where:

$$\frac{\overline{\sum a_i u_j}}{a_P^e} = \frac{1}{2}\left[\frac{\left(\sum a_i u_j\right)_P}{a_P^P} + \frac{\left(\sum a_i u_j\right)_E}{a_P^E}\right] \tag{5.72}$$

$$\frac{1}{\overline{a_P^e}} = \frac{1}{2}\left[\frac{1}{a_P^P} + \frac{1}{a_P^E}\right] \tag{5.73}$$

The bar in Eqs. (5.71), (5.72), and (5.73) indicates the interpolation between the values of the two nodes P and E. Taylor series is used to expand u_e as follows:

$$u_e = u_e^{\circ} + \frac{\partial u_e}{\partial P_P}\Delta P_P + \frac{\partial u_e}{\partial P_E}\Delta P_E \tag{5.74}$$

ΔP in Eq. (5.74) represents the pressure difference and is defined as follows:

$$\Delta P = P - P^{\circ} \tag{5.75}$$

In Eqs. (5.74) and (5.75), u_e° and P° are velocity and pressure values obtained from the previous iteration, respectively. Differentiating Eq. (5.71) with respect to the pressure at node P and node E, respectively, we get:

$$\frac{\partial u_e}{\partial P_P} = \frac{\Delta y \Delta z}{\overline{a_P^e}} \tag{5.76}$$

$$\frac{\partial u_e}{\partial P_E} = -\frac{\Delta y \Delta z}{\overline{a_P^e}} \tag{5.77}$$

Substituting the partial derivatives of u_e, Eqs. (5.76) and (5.77), in Eq. (5.74), the following expression for u_e is obtained:

$$u_e = u_e^{\circ} + \frac{\Delta y \Delta z}{\overline{a_P^e}} (\Delta P_P - \Delta P_E) \tag{5.78}$$

Similar expressions can be found for the other velocities on the other different faces as follows:

$$u_w = u_w^{\circ} + \frac{\Delta y \Delta z}{\overline{a_P^w}} (\Delta P_W - \Delta P_P) \tag{5.79}$$

$$v_s = v_s^{\circ} + \frac{\Delta x \Delta z}{\overline{a_P^s}} (\Delta P_P - \Delta P_S) \tag{5.80}$$

$$v_n = v_n^{\circ} + \frac{\Delta x \Delta z}{\overline{a_P^n}} (\Delta P_N - \Delta P_P) \tag{5.81}$$

$$w_{lo} = w_{lo}^{\circ} + \frac{\Delta y \Delta x}{\overline{a_P^{lo}}} (\Delta P_P - \Delta P_{LO}) \tag{5.82}$$

$$w_{up} = \overset{\circ}{w}_{up} + \frac{\Delta y \Delta x}{\overline{a_P^{up}}}(\Delta P_{UP} - \Delta P_P)$$

(5.83)

By substituting u_e, u_w, v_s, v_n, w_{lo}, and w_{up} into the continuity equation, Eq. (5.5), the following result will be reached:

$$\left[-\rho\frac{\Delta y^2 \Delta z^2}{\overline{a_P^w}}\Delta P_W\right] + \rho\left[\frac{\Delta y^2 \Delta z^2}{\overline{a_P^e}} + \frac{\Delta y^2 \Delta z^2}{\overline{a_P^w}} + \frac{\Delta x^2 \Delta z^2}{\overline{a_P^s}} + \frac{\Delta x^2 \Delta z^2}{\overline{a_P^n}} + \frac{\Delta x^2 \Delta y^2}{\overline{a_P^{lo}}} + \frac{\Delta x^2 \Delta y^2}{\overline{a_P^{up}}}\right]\Delta P_P$$

$$+\left[-\rho\frac{\Delta y^2 \Delta z^2}{\overline{a_P^e}}\Delta P_E\right] = \rho\frac{\Delta x^2 \Delta z^2}{\overline{a_P^s}}\Delta P_S + \rho\frac{\Delta x^2 \Delta z^2}{\overline{a_P^n}}\Delta P_N + \rho\frac{\Delta x^2 \Delta y^2}{\overline{a_P^{lo}}}\Delta P_{LO} + \rho\frac{\Delta x^2 \Delta y^2}{\overline{a_P^{up}}}\Delta P_{UP}$$

$$+\rho\Delta y\Delta z(\overset{\circ}{u}_w - \overset{\circ}{u}_e) + \rho\Delta x\Delta z(\overset{\circ}{v}_n - \overset{\circ}{v}_s) + \rho\Delta x\Delta y(\overset{\circ}{w}_{up} - \overset{\circ}{w}_{lo})$$

(5.84)

Eq. (5.84) can be written in the following reduced form:

$$\overline{a_P}\Delta P_P = \sum_{\substack{i=e,w,s,n,lo,up \\ j=E,W,S,N,LO,UP}} \overline{a_i}\Delta P_j - \sum_{i=e,w,s,n,lo,up} G_i^{\circ}$$

(5.85)

where:

$$\overline{a_P} = \rho\left[\frac{\Delta y^2 \Delta z^2}{\overline{a_P^e}} + \frac{\Delta y^2 \Delta z^2}{\overline{a_P^w}} + \frac{\Delta x^2 \Delta z^2}{\overline{a_P^s}} + \frac{\Delta x^2 \Delta z^2}{\overline{a_P^n}} + \frac{\Delta x^2 \Delta y^2}{\overline{a_P^{lo}}} + \frac{\Delta x^2 \Delta y^2}{\overline{a_P^{up}}}\right]$$

(5.86)

$$\overline{a_e} = \rho\frac{\Delta y^2 \Delta z^2}{\overline{a_P^e}}$$

(5.87)

$$\overline{a_w} = \rho\frac{\Delta y^2 \Delta z^2}{\overline{a_P^w}}$$

(5.88)

$$\overline{a_s} = \rho\frac{\Delta x^2 \Delta z^2}{\overline{a_P^s}}$$

(5.89)

$$\overline{a_n} = \rho \frac{\Delta x^2 \Delta z^2}{\overline{a_P^n}} \tag{5.90}$$

$$\overline{a_{lo}} = \rho \frac{\Delta x^2 \Delta y^2}{\overline{a_P^{lo}}} \tag{5.91}$$

$$\overline{a_{up}} = \rho \frac{\Delta x^2 \Delta y^2}{\overline{a_P^{up}}} \tag{5.92}$$

and:

$$\sum_{i=e,w,s,n,lo,up} G_i^\circ = \rho \Delta y \Delta z (u_e^\circ - u_w^\circ) + \rho \Delta x \Delta z (v_s^\circ - v_n^\circ) + \rho \Delta x \Delta y (w_{lo}^\circ - w_{up}^\circ) \tag{5.93}$$

Eqs. (5.48), (5.49), (5.50), and (5.85) are solved using the tridiagonal matrix algorithm (TDMA) (Roberson and Crowe 1997) to obtain the velocity and pressure difference at each node.

For the next iteration, velocity and pressure values at the nodal points (*P*) are corrected using the calculated pressure difference. This correction is shown in Eqs. (5.94) through (5.97).

$$u_P = u_P^\circ + \frac{\Delta y \Delta z}{a_P} \left(\frac{\Delta P_W - \Delta P_E}{2} \right) \tag{5.94}$$

$$v_P = v_P^\circ + \frac{\Delta x \Delta z}{a_P} \left(\frac{\Delta P_N - \Delta P_S}{2} \right) \tag{5.95}$$

$$w_P = w_P^\circ + \frac{\Delta x \Delta y}{a_P} \left(\frac{\Delta P_{UP} - \Delta P_{LO}}{2} \right) \tag{5.96}$$

$$P_P = P_P^\circ + \omega_1 \Delta P \tag{5.97}$$

where ω_l is the relaxation factor for the pressure.

The following formula is used to correct the velocity at the east face:

$$\frac{u_P + u_E}{2} = \left[\frac{\sum a_i u_j}{2a_P^P} + \frac{\Delta y \, \Delta z}{2a_P^P} \frac{(P_W - P_E)}{2} \right] + \left[\frac{\sum a_i u_j}{2a_P^E} + \frac{\Delta y \, \Delta z}{2a_P^E} \frac{(P_P - P_{EE})}{2} \right] \tag{5.98}$$

and rearranging the different terms, we get:

$$\frac{u_P + u_E}{2} = \frac{1}{2}\left[\frac{\sum a_i u_j}{a_P^P} + \frac{\sum a_i u_j}{a_P^E} \right] + \frac{1}{2}\left[\frac{(P_W - P_E)}{2a_P^P} + \frac{(P_P - P_{EE})}{2a_P^E} \right]\Delta y \Delta z \tag{5.99}$$

where P_{EE} is the pressure at node located two cells to the east of nodal point P.

Assuming that $\left(\Delta y \Delta z / a_P^P \right) = \left(\Delta y \Delta z / a_P^E \right) = \left(\overline{\Delta y \Delta z / a_P^e} \right)$ and noting that

$$\frac{1}{2}\left[\frac{\sum a_i u_j}{a_P^P} + \frac{\sum a_i u_j}{a_P^E} \right] = \overline{\frac{\sum a_i u_j}{a_P^e}} \; , \text{ and } \; \frac{1}{2}\left[\frac{1}{a_P^P} + \frac{1}{a_P^E} \right] = \frac{1}{\overline{a_P^e}} \tag{5.100}$$

we get:

$$\frac{u_P + u_E}{2} = \overline{\frac{\sum a_i u_j}{a_P^e}} + \frac{1}{2\overline{a_P^e}}\left[\frac{P_W - P_E}{2} + \frac{P_P - P_{EE}}{2} \right]\Delta y \Delta z \tag{5.101}$$

The velocity at the eastern face of the control volume, u_e, can be approximated using Eq. (5.102), which can be obtained by subtracting Eq. (5.89) from Eq. (5.59).

$$u_e = \left[\frac{u_P + u_E}{2} \right] + \frac{\Delta y \Delta z}{4\overline{a_P^e}}\left[-P_W + 3P_P - 3P_E + P_{EE} \right] \tag{5.102}$$

Similar results can be approximated for the velocities of the other faces of the control volume as follows:

$$u_w = \left[\frac{u_P + u_W}{2}\right] + \frac{\Delta y \Delta z}{4\overline{a_P^w}}\left[-P_{WW} + 3P_W - 3P_P + P_E\right] \tag{5.103}$$

$$v_s = \left[\frac{v_P + v_S}{2}\right] + \frac{\Delta x \Delta z}{4\overline{a_P^s}}\left[-P_N + 3P_P - 3P_S + P_{SS}\right] \tag{5.104}$$

$$v_n = \left[\frac{v_P + v_N}{2}\right] + \frac{\Delta x \Delta z}{4\overline{a_P^n}}\left[-P_{NN} + 3P_N - 3P_P + P_S\right] \tag{5.105}$$

$$w_{lo} = \left[\frac{w_P + w_{LO}}{2}\right] + \frac{\Delta x \Delta y}{4\overline{a_P^{lo}}}\left[-P_{UP} + 3P_P - 3P_{LO} + P_{LOLO}\right] \tag{5.106}$$

$$w_{up} = \left[\frac{w_P + w_{UP}}{2}\right] + \frac{\Delta x \Delta y}{4\overline{a_P^{up}}}\left[-P_{UPUP} + 3P_{UP} - 3P_P + P_{LO}\right] \tag{5.107}$$

As mentioned earlier, Eq. (5.70) is used to calculate the different velocities at the different faces of the control volume in the first iteration only. For the next iterations, Eqs. (5.102) through (5.107) replace Equation (5.70).

The convergence criterion for the numerical solution is chosen to be the continuity residual as follows:

$$\sum \left|G_i\right| < \varepsilon_{\circ} \tag{5.108}$$

where, the summation is carried out for all the computational cells in each iteration, and $\varepsilon_{\circ}$ is the maximum permissible error in the continuity residual. Another additional, but

not necessary, criterion that can be used is the stabilization of the maximum Re_c through the iterative simulation process.

The 3-D microstructure has the dimensions h_x, h_y, and h_z in the x-, y-, and z-directions respectively. h_x and h_y are the horizontal dimensions, while h_z is the vertical thickness of the microstructure. Periodic boundary conditions are applied in the analysis of the idealized microstructures. However, for the actual microstructures of asphalt mixes, no flow is allowed in the horizontal direction at the sides of the model, and periodic boundary conditions are applied in the vertical direction. Applying the "no slip" boundary condition, the different velocity components at the solid phase will be identically zero as indicated by Eq. (5.109).

$$u = v = w = 0 \tag{5.109}$$

Determination of Permeability Tensor

Darcy's law, Eq. (5.110), can be used in determining the elements of the fluid absolute permeability tensor (K_{ij}).

$$\vec{V} = -\frac{1}{\mu} \mathrm{K} \cdot \vec{\nabla} P \tag{5.110}$$

The pressure gradient $\vec{\nabla} P$ can be written in the following vector form:

$$\vec{\nabla} P = \frac{\partial P}{\partial x} \hat{i} + \frac{\partial P}{\partial y} \hat{j} + \frac{\partial P}{\partial z} \hat{k} \tag{5.111}$$

where $\hat{i}$, $\hat{j}$, and $\hat{k}$ are unit vectors in the x-, y-, and z-directions, respectively. In a matrix

form, Eq. (5.110) can be written as follows:

$$\begin{bmatrix} \overline{u} \\ \overline{v} \\ \overline{w} \end{bmatrix} = -\frac{1}{\mu} \begin{bmatrix} K_{xx} & K_{xy} & K_{xz} \\ K_{yx} & K_{yy} & K_{yz} \\ K_{zx} & K_{zy} & K_{zz} \end{bmatrix} \begin{bmatrix} \partial P/\partial x \\ \partial P/\partial y \\ \partial P/\partial z \end{bmatrix} \qquad (5.112)$$

where $\overline{u}, \overline{v},$ and $\overline{w}$ are the average velocities of all points within the microstructure in the

x-, y- and z-directions, respectively.

The elements of the permeability tensor (K_{ij}) are calculated through three independent

steps. In the first step, a pressure gradient is applied in the x-direction only, and in this

case, K_{xx}, K_{yx} and K_{zx} are determined. In the second and third steps, the pressure gradient

is applied in the y- and z-directions, respectively, and the other six elements of the

absolute permeability tensor are calculated. The following is an illustration of the first

step.

Define the pressure as a function of x only, as follows:

$$P = P_{inlet} + \left(\frac{P_{outlet} - P_{inlet}}{h_x} \right) x \qquad (5.113)$$

where P_{inlet} and P_{outlet} are the pressure values at the inlet and outlet of the microstructure,

respectively; h_x is the dimension in the x-direction, which is the distance on which the

pressure had changed from P_{inlet} to P_{outlet}, and x is the distance measured from the point

where P_{inlet} is applied.

From Eq. (5.112), $\bar{u}$ can be calculated as follows:

$$\bar{u} = -\frac{1}{\mu}\left(K_{xx}\frac{\partial P}{\partial x} + K_{xy}\frac{\partial P}{\partial y} + K_{xz}\frac{\partial P}{\partial z}\right) \tag{5.114}$$

$$= -\frac{1}{\mu}\left(K_{xx}\frac{P_{outlet} - P_{inlet}}{h_x}\right) \tag{5.115}$$

$$= -\frac{1}{\mu h_x}K_{xx}\Delta P_x \tag{5.116}$$

where:

$$\Delta P_x = P_{outlet} - P_{inlet} \tag{5.117}$$

The other two velocities, $\bar{v}$ and $\bar{w}$, can be found using the same steps:

$$\bar{v} = -\frac{1}{\mu h_x}K_{yx}\Delta P_x \tag{5.118}$$

$$\bar{w} = -\frac{1}{\mu h_x}K_{zx}\Delta P_x \tag{5.119}$$

Rearranging Eqs. (5.116), (5.118), and (5.119) for K_{xx}, K_{yx}, and K_{zx}, respectively, we get:

$$K_{xx} = \frac{-(\mu h_x)\bar{u}}{\Delta P_x}, K_{yx} = \frac{-(\mu h_x)\bar{v}}{\Delta P_x}, K_{zx} = \frac{-(\mu h_x)\bar{w}}{\Delta P_x} \tag{5.120}$$

From the second and third steps, the other six components of the absolute permeability tensor will have the following forms:

$$K_{xy} = \frac{-(\mu h_y)\bar{u}}{\Delta P_y}, K_{yy} = \frac{-(\mu h_y)\bar{v}}{\Delta P_y}, K_{zy} = \frac{-(\mu h_y)\bar{w}}{\Delta P_y},$$

$$K_{xz} = \frac{-(\mu h_z)\bar{u}}{\Delta P_z}, K_{yz} = \frac{-(\mu h_z)\bar{v}}{\Delta P_z}, K_{zz} = \frac{-(\mu h_z)\bar{w}}{\Delta P_z}$$

(5.121)

In general, the absolute permeability tensor, K_{ij}, has the units of (m^2). To convert K_{ij} to Darcy's permeability tensor k_{ij} with units of (m/s), it is multiplied by the unit weight of the fluid, γ, and divided by the fluid viscosity, μ, as indicated in Eq. (5.122) below. For water at 20°C, γ=9.79 kN/m^3 and μ=0.001 kg/(m.sec.):

$$k = K\frac{\gamma}{\mu}$$

(5.122)

Verification of Numerical Model and its Ability in Simulating Fluid Flow of Idealized 3-D Microstructures

For the purpose of model verification, the model is used to simulate fluid flow in some idealized microstructures, and the numerical results are compared to analytical solutions. These idealized microstructures include a medium of small fissures, a medium of packed cubes, and a medium of spheroids that is used to investigate the permeability anisotropy.

Bear (1972) discussed the flow within porous media of parallel fissures. He pointed out that this type of flow is similar to the flow between two parallel stationary plates. The flow between these two stationary plates is driven only by pressure which is applied in the x-direction (Fig. 5.4). This flow has a velocity distribution, $V_x(y)$, which is in the x-

direction and a function of the *y*-direction only. At the same *y* value, the velocity V_x is constant for different *x* and *z* values. The maximum value for V_x is at the mid height of the fissure. There is no flow in the *y*- or *z*-directions. $V_x(y)$ has the following form (Panton 1984):

$$V_x(y) = \frac{-1}{2\mu} \frac{dP}{dx} \left(\frac{b^2}{4} - y^2 \right) \tag{5.123}$$

where *P* is the pressure applied in the x-direction, *b* is the distance between the two plates or pore size, and μ is the fluid viscosity.
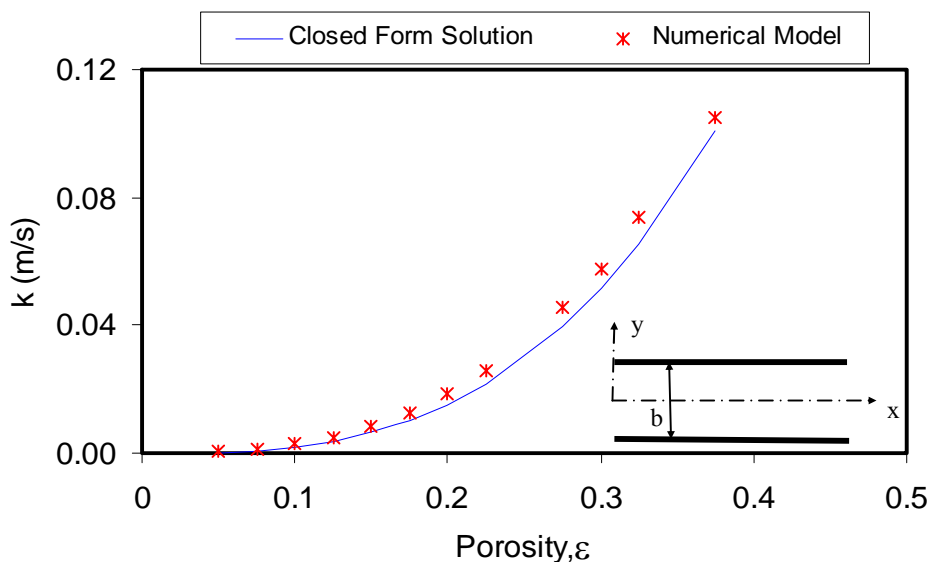
Fig. 5.4. Comparison of numerical model results to closed-form solution for fluid flow in a medium of parallel fissures

Bear (1972) pointed out that the average velocity (V_{avg}) can be obtained using the following formula:

$$V_{avg} = \left(\frac{b^2}{12}\right)\left(\frac{1}{\mu}\right)\frac{dP}{dx}$$

(5.124)

For fissures that have a pore size of b and are separated by a grain size a, Bear (1972) had shown that the absolute permeability, K, can be calculated as follows:

$$K = \frac{\varepsilon b^2}{12}$$

(5.125)

where ε is the porosity and equal to $b/(a+b)$.
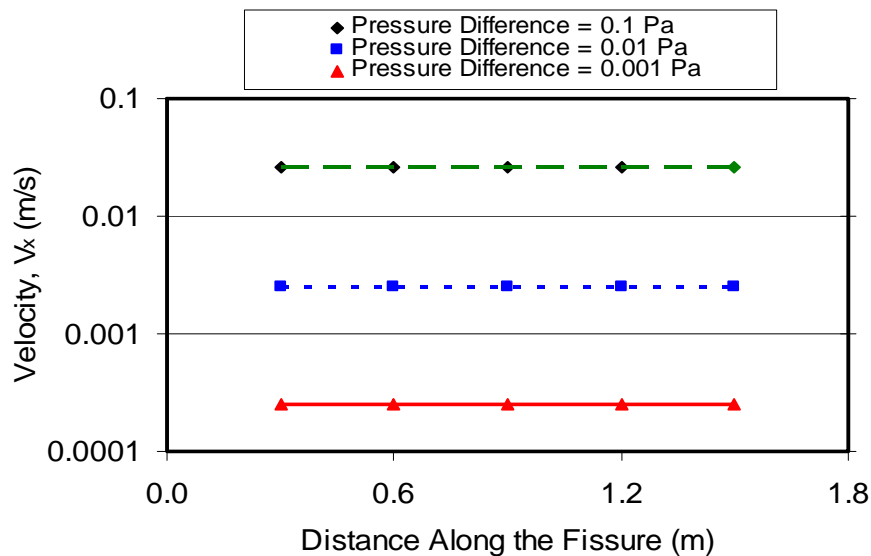
Fig. 5.5. Velocity distribution of fluid flow in a medium of parallel fissures at different pressure difference values

Fluid flow through porous media of parallel fissures is simulated using different ε values. The numerical model complied with Eq. (5.123) in terms of the velocity distribution of the fluid flow in porous media of parallel fissures. Fig. 5.5 shows that for a given applied pressure gradient, the velocity $V_x(y)$ is constant along the fissure length. It also shows that this value of $V_x(y)$ is higher for higher pressure gradients. Fig. 5.6 shows a comparison of the velocity profiles from Eq. (5.123) and the numerical model. Fig. 5.4 shows the permeability coefficient k for different porosities obtained by the numerical model and fissure model, Eq. (5.125). It can be seen that the numerical model simulates the closed-form solution very well.
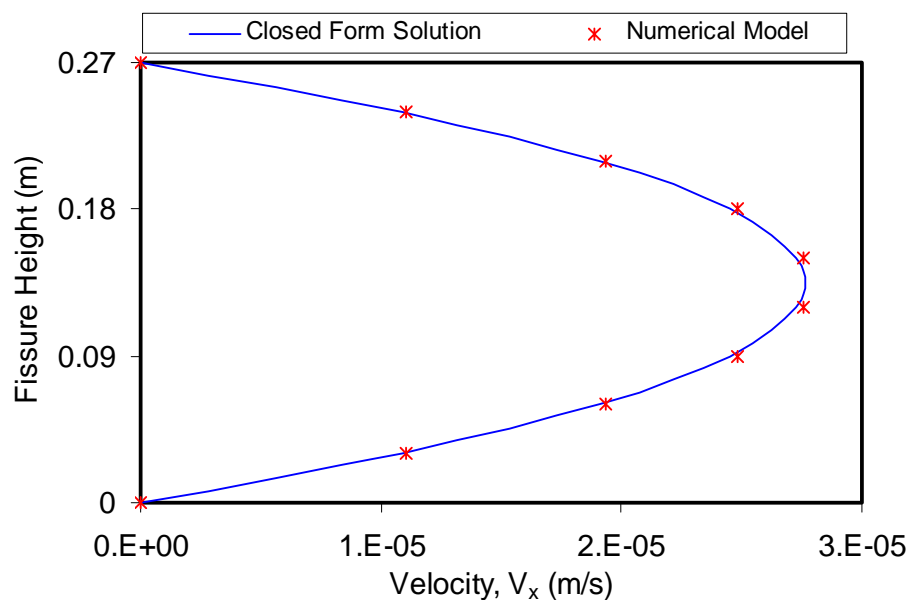
Fig. 5.6. Velocity distribution of porous media of parallel fissures at different height levels

Fluid flow in porous media of packed cubes is also investigated. The closed-form solution by Ergun (1952) shows that the absolute permeability of porous media of packed spheres with the same radii can be calculated as follows:

$$K = \frac{\varepsilon^3}{150(1-\varepsilon)^2} d_p^2 \qquad (5.126)$$

where ε is the porosity of the porous media, and d_p is the diameter of the sphere.
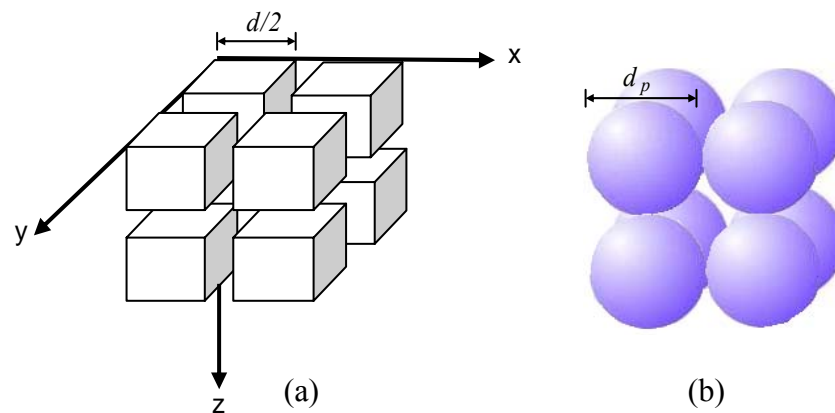
Fig. 5.7. (a) Medium of cubes with side length, d, and separated by a fixed distance (b) Medium of Packed Spheres with Diameter, d_p

In the simulation model, cubes of side d are used to replace spheres with equivalent diameters of d_p (Fig. 5.7) to simplify creating the model geometry. Therefore, the packed spheres porous media are represented by porous media of cubes of side d separated by a

fixed distance. It is assumed that the volume of a cube of side d is equivalent to that of a sphere of diameter d_p; therefore the relation between d and d_p is:

$$d_p = \left(\frac{6}{\pi}\right)^{\frac{1}{3}} d \qquad (5.127)$$

Fluid flow in the porous media of packed cubes is driven only by the pressure difference applied in the x-direction. The permeability values for both the numerical simulation and Ergun's solution are shown in Fig. 5.8. This figure shows that the numerical simulation approximates very well the Ergun's solution, especially for low porosity values.
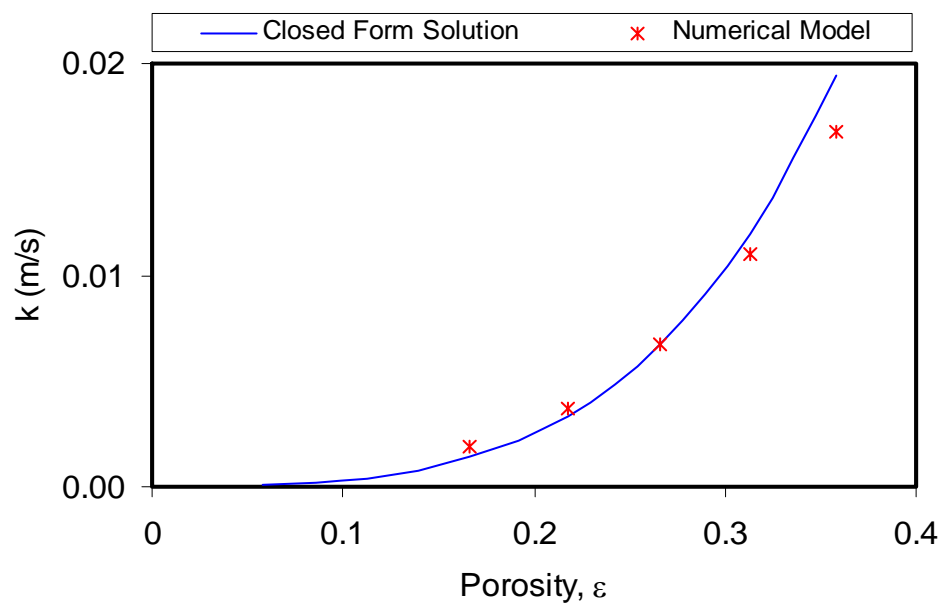
Fig. 5.8. Comparison of numerical model results to closed-form solution for fluid flow in a medium of packed spheres

Fig. 5.9 shows the velocity vector distribution for a section in the medium of packed cubes. Each vector represents the magnitude and direction of the velocity at a given point of the microstructure. As can be seen from Fig. 5.9, the velocity vectors are mainly in the direction of the pressure difference (x-direction). Its direction differs slightly from the x-direction at the intersection of the x-direction with the other two directions.
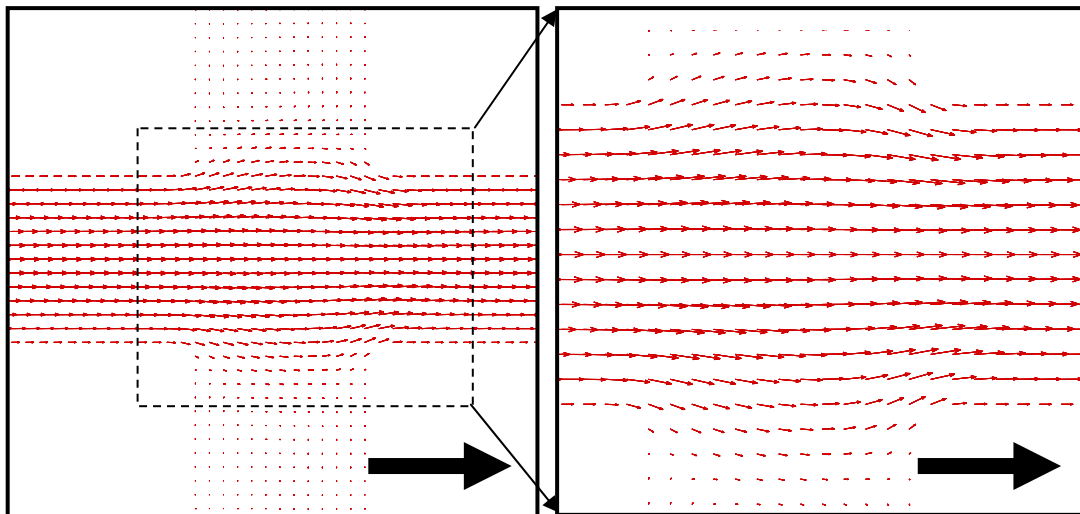
Fig. 5.9. Fluid velocity distribution in a section of a medium of packed cubes (the arrow presents the direction of the applied pressure difference)

The parallel fissures medium (Fig. 5.4) and the medium of packed cubes (Figs. 5.7 and 5.8) have the same microstructure size. At the same porosity level, permeability of the parallel fissures medium is higher than permeability of the medium of packed cubes. The

ratio between the permeability of both media ($k_{Parallel\ fissures}/k_{Packed\ cubes}$) ranges from a value that is slightly higher than 8.0 at very low porosity level to a value of 4.1 at a porosity of 0.4 (Fig. 5.10). This is due to the fact that the void connectivity in the fissure model is higher than that of the packed cubes.
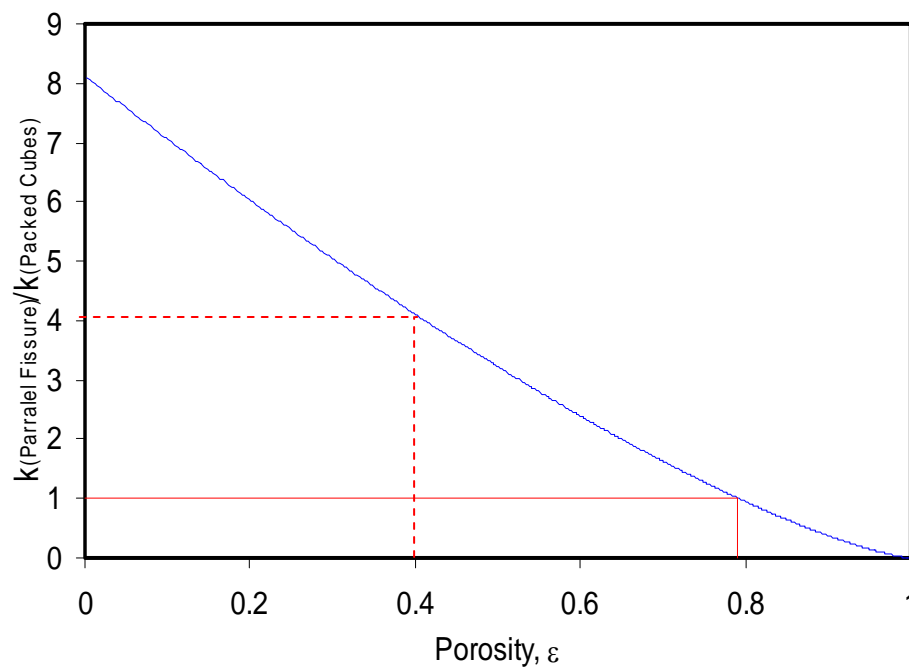
Fig. 5.10. Ratio of permeability of medium of small fissures to permeability of medium of cubes

The anisotropy of the permeability coefficient is investigated using a medium of dilute beds of spheroids. The anisotropy of the permeability coefficient is presented here as the ratio of the permeability in the x-direction to the permeability in y- or z-direction. The

spheroid is a special case from the ellipsoid in which two of the three axes are equal. Fig. 5.11 shows a typical spheroid with its center is at the origin. The equation for the spheroid is shown in Eq. (5.128) where $b=a/c$.

$$b^2x^2 + y^2 + z^2 = a^2 \qquad (5.128)$$
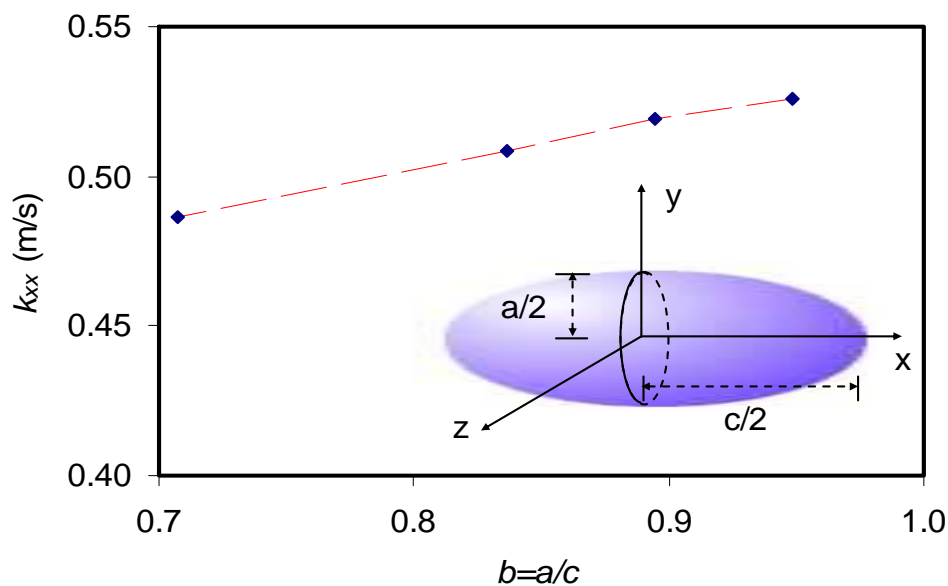
Fig. 5.11. Permeability, k_{xx}, of medium of diluted spheroids at different values of b

Torquato (2001) stated that the permeability coefficient is isotropic in the case of spheres ($b=1$). For needle-shaped spheroids with a value of b less than unity, k_{xx} decreases with decreasing b. The ratio k_{xx}/k_{yy} (or k_{xx}/k_{zz}), on the contrary, will increase with decreasing b. This ratio represents the anisotropy of the permeability coefficient. These are consistent with the results from the numerical model depicted in Figs. 5.11 and 5.12.
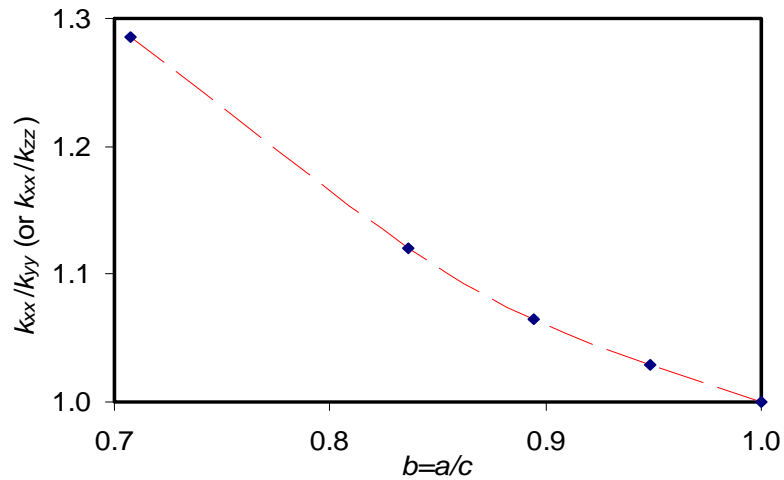
Fig. 5.12. Permeability anisotropy, k_{xx}/k_{yy} or (k_{xx}/k_{zz}), for a medium of diluted spheroids at different values of b

Numerical Stability of the Simulation Model

The sensitivity of the numerical solution to the change in the pressure gradient and the initial velocity values is investigated. The cell Reynolds number for the flow in the analyzed standard 3-D microstructures was found to be very small; that is $|R_e| << 1.0$. Then, the flow in these microstructures is laminar where the permeability coefficient is a material property that should not change with changing the pressure gradient. This is clearly shown in Fig. 5.13.

Using different initial velocity values, Fig. 5.14 shows that the permeability is constant testifying to the stability of the solution.
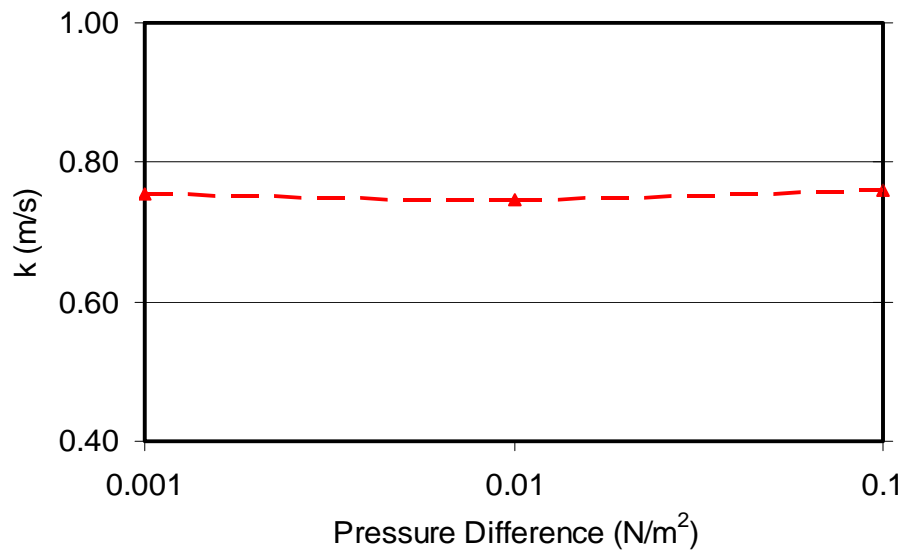
Fig. 5.13. Permeability, k, at different pressure difference values
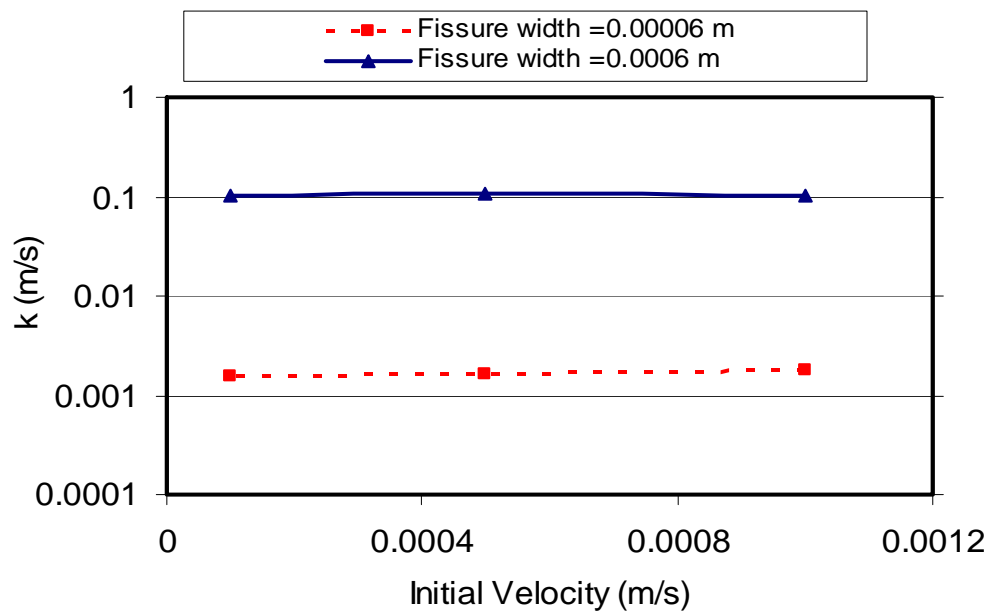
Fig. 5.14. Permeability, k, at different initial velocity values and two different fissure widths

Fig. 5.15 shows an example of the progress of the continuity residual, $\sum|G_i|$, shown in Eq. (5.108) during the simulation of fluid flow. It can be seen that the residual is decreasing with increasing the iteration number, which is another indication of convergence. Moreover, Fig. 5.16 shows the convergence of the maximum Re_c during the simulation of fluid flow.
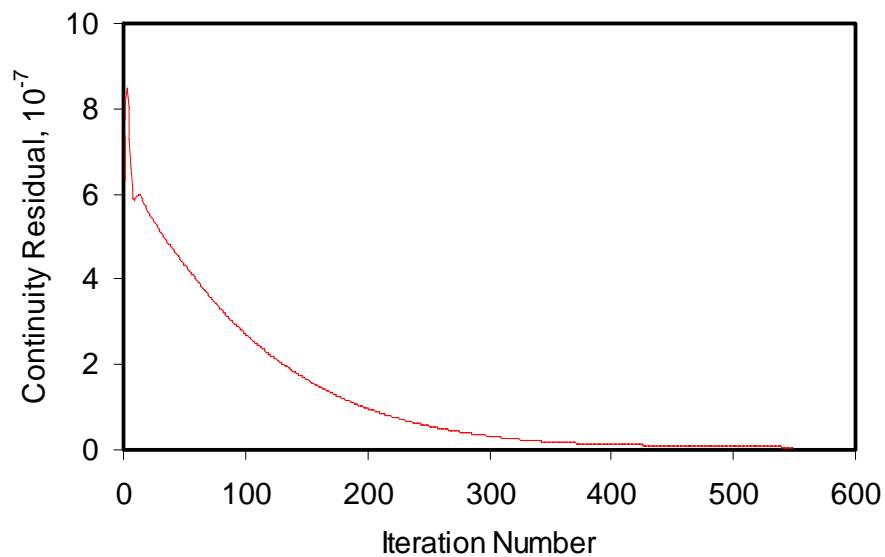
Fig. 5.15. An example of the value for continuity residual changing during the simulation of fluid flow

Summary

Chapter V presented the development of the finite difference simulation model using the flow governing equations: continuity equation and the momentum (Navier-Stokes)

equations. The model simulates the 3-D steady incompressible fluid flow in porous materials such as HMA mixes. It used the non-staggered grid system formulation, and it converges for values of Re_c that are not restricted by $|Re_c| \leq 2$. The model was then verified using some standard 3-D microstructures including medium of packed spheres and medium of small fissures. Each medium has a derived closed-form solution for its permeability. The stability of the numerical solution was also verified in this chapter through observing the change in the continuity equation residual and investigating the influence of the assumed initial velocities on permeability.
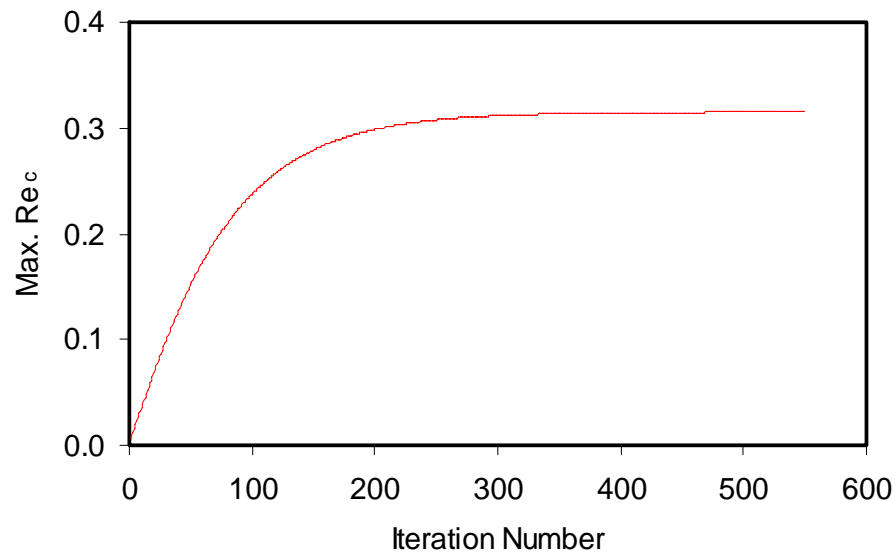
Fig. 5.16. An example of the stabilization of maximum Re_c during the simulation of fluid flow

CHAPTER VI

ANALYSIS OF PERMEABILITY TENSOR AND ANISOTROPY

Introduction

Chapter V discussed the development of the numerical finite difference fluid flow simulation model and the determination of permeability tensor. In this chapter, the influence of some numerical and experimental factors on the simulation results is discussed. These factors include the simulation truncation criterion, spatial resolution of the microstructure, and aspect ratio of computational cells.

This chapter also presents the results of calculating the components of the 3-D permeability tensor. The permeability eigen vectors and the anisotropy coefficient, defined as the ratio of the horizontal permeability to the vertical permeability, are calculated from the permeability tensor.

Numerical and Experimental Factors Affecting Model Predictions

HMA specimens are cylindrical in shape. The result of scanning of these HMA specimens is a group of 2-D circular images. Figs. 3.2, 3.4, and 3.5 show examples of these 2-D circular images. Each specimen consists of a different number of 2-D images depending on its thickness (Table 3.1). The simulation program works with a parallelogram-shaped microstructure. Therefore, square sections were extracted from the circular images (Fig. 6.1).

In order to include the largest volume of the microstructure in the simulation, it was decided to choose the largest square (Fig. 6.1) that can be included inside the horizontal circular image. It was also decided to use the whole thickness of the specimen. The result was a 3-D microstructure that was about 63.7% of the total volume of the analyzed specimen. The difference between the original microstructures and the microstructures used in the simulation model may result in some discrepancy between the calculated and measured permeability results.
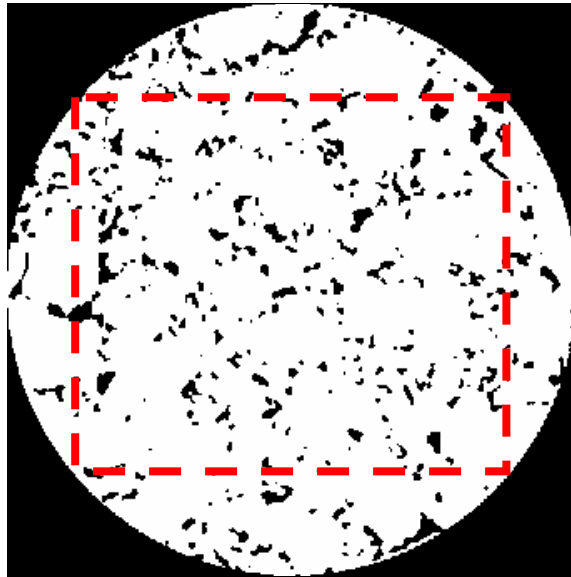
Fig. 6.1. The square portion (dashed line) of the X-ray CT image shown in Fig. 3.5

The first step in the numerical analysis was to determine the criterion for the termination of the simulation. To this end, fluid flow simulations were conducted for a number of HMA specimens using different numbers of iterations. It was found that the residual of the continuity equation, $\sum|G_i|$, reached a plateau at a minimum value after about 1000 iterations. This was also the same for the permeability value as shown in Fig. 6.2.
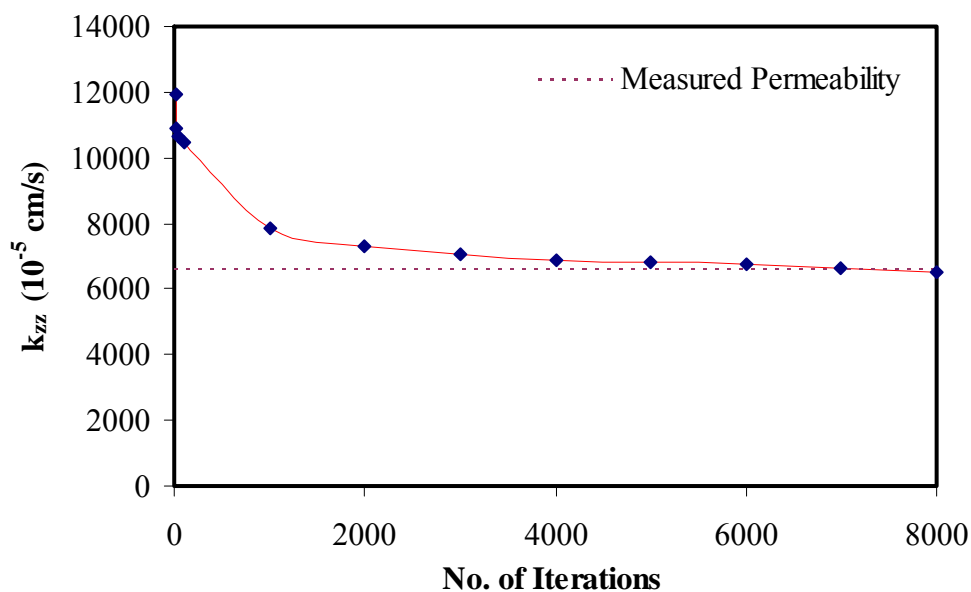
Fig. 6.2. Permeability, k_{zz}, of an asphalt mix specimen at different number of iterations

The second step in the analysis was to determine the sensitivity of the numerical solution to the number of computational cells (microstructure resolution) and microstructure aspect ratio. Ideally speaking and to have high microstructure resolutions, it is preferred to have as many computational cells as possible in all three directions. However, this is

not feasible for two main reasons. First, the size of a specimen imposes a limitation on the horizontal resolution, while the thickness of the X-ray beam limits the vertical resolution. In general, the vertical resolution was about four to five times the horizontal resolution. The second reason is that increasing image resolution comes with the penalty of increasing the simulation time, which should be kept within reasonable limits.

A sensitivity analysis was conducted to determine the influence of number of factors on the numerical results such that the objective of determining the 3-D resolution that gives accurate results within reasonable analysis time is satisfied. These factors are the number of computational cells in the direction of the pressure gradient (flow direction), the number of computational cells perpendicular to the direction of the pressure gradient, and the assumed initial velocity values.

A number of specimens were selected and analyzed using different image resolutions both in the direction of the pressure gradient and perpendicular to this direction. The resolution was reduced by combining a certain number of adjacent pixels into one pixel. The resulting pixel can be solid or void depending on the average intensity of the combined pixels.

The influence of image resolution and number of pixels per image on the microstructure is illustrated by calculating the percent air voids and air void specific surface area using Eqs. (3.1) and (3.2), respectively. Two different image resolutions were chosen: the

original image resolution of 0.146 mm/pixel and a rougher resolution of 0.584 mm/pixel.

Table 6.1 shows the different values of percent air voids and air void specific surface

area of the LKC laboratory specimens for the two different image resolutions.

Table 6.1. Percent of Air Voids and Specific Surface Area Parameter for the LKC

Laboratory Specimens at Two Different Image Resolutions

Specimen	100×100 pixels/image Resolution of 0.584 (mm/pixel)		400×400 pixels/image Resolution of 0.146 (mm/pixel)		Ratio (S_2/S_1)
	% AV	Specific Surface Area Parameter, S_1 (mm^{-1})	% AV	Specific Surface Area Parameter, S_2 (mm^{-1})	
LKC-01	11.3	0.10	12.3	0.24	2.4
LKC-02	11.2	0.10	10.7	0.20	2.0
LKC-03	12.5	0.11	11.9	0.26	2.4
LKC-04	13.9	0.12	12.5	0.30	2.5
LKC-05	06.0	0.05	07.1	0.15	3.0
LKC-06	08.4	0.07	09.0	0.12	1.7
LKC-07	12.0	0.11	12.5	0.32	2.9
LKC-08	10.0	0.09	09.2	0.23	2.6
LKC-09	11.1	0.10	11.0	0.24	2.4
LKC-10	16.8	0.14	16.5	0.28	2.0
LKC-11	10.1	0.09	10.4	0.21	2.3
LKC-12	11.3	0.10	11.4	0.29	2.9
LKC-13	12.1	0.11	12.0	0.25	2.3
LKC-14	12.2	0.11	11.1	0.32	2.9

It can be seen from Table 6.1 that although the value of percent air voids was slightly

affected with change in resolution, air void specific surface area increased by more than

two times on average with an increase in resolution. Permeability is inversely

proportional to air void specific surface area, and consequently, it was found to decrease as the image resolution increased.

It is desirable to refine the mesh and increase the number of computational cells in the direction of the pressure gradient. Given that the vertical resolution was captured using X-ray CT at 0.8 mm/pixel, the resolution was achieved using two approaches. The first approach was to duplicate each of the images a number of times until the desired resolution is achieved. However, this approach might induce a numerical error. Consider, for example, a pixel of void connected to a pixel of solid in the image above. The velocity will change from a certain value in the void pixel to zero in the solid pixel within one computational cell. However, if each of these two images is duplicated three times, then the velocity gradient between these six images will be different than the velocity gradient between the original two images.

In order to determine whether image duplication would influence the results or not, a second approach was adopted in which the "pixel intensity averaging technique" was used in order to obtain a number of images between each pair of consecutive images. This technique can be envisioned as the opposite of the process involved in X-ray CT. In other words, it reverses the averaging involved in obtaining images with a resolution of 0.8 mm/pixel. In X-ray CT, pixel intensity is an indication of the average material density within a certain thickness that is equal to the vertical resolution. One can assume that the density changes linearly between each two consecutive images, and the intensity

of each pixel in an intermediate image can be obtained by averaging the intensities of the pixels above and below this intermediate image.

The averaging process was applied to the original gray scale images using the toolbox of the Image-Pro Plus (Image-Pro Plus 1999). In the original image, each pixel has a value between 0 for materials with the lowest density and 255 for materials with the highest density. In the averaging process, the value of each pixel is averaged with the value of the pixel in the same location on the image underneath. Fig. 6.3 illustrates the averaging process of two simple idealized images. The ovals in Fig. 6.3 (a) and (b) are intentionally chosen black so that the averaging process for the extreme case, black (void) pixels being averaged with white (solid) pixels, is clearly illustrated. This case occurs when the microstructure suddenly changes from one image to the one underneath.
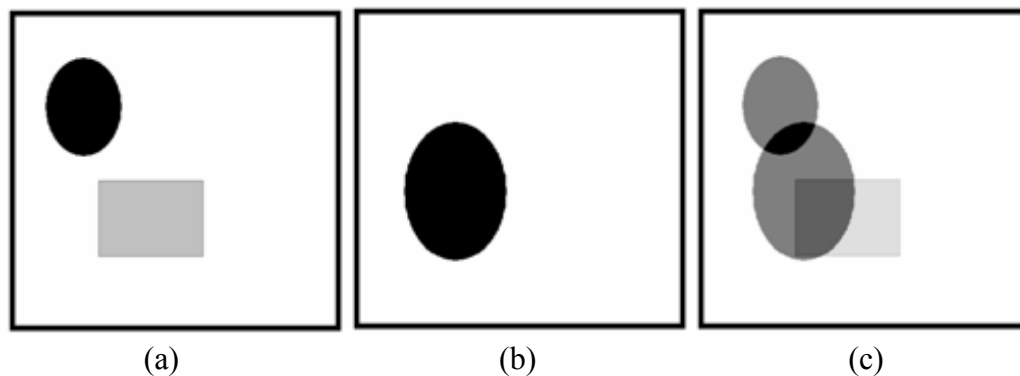
Fig. 6.3. Image (c) is the average of the simple idealized images (a) and (b)

By averaging the images once, the number of computational cells in the vertical direction will be doubled with the vertical resolution being reduced from 0.8 to 0.4 mm/image. This process can be repeated two or three times to have more vertical computational cells with finer resolutions. It was found that both the duplication of images and the "pixel averaging technique" give similar permeability results at fine vertical resolutions around 0.3 mm/image.
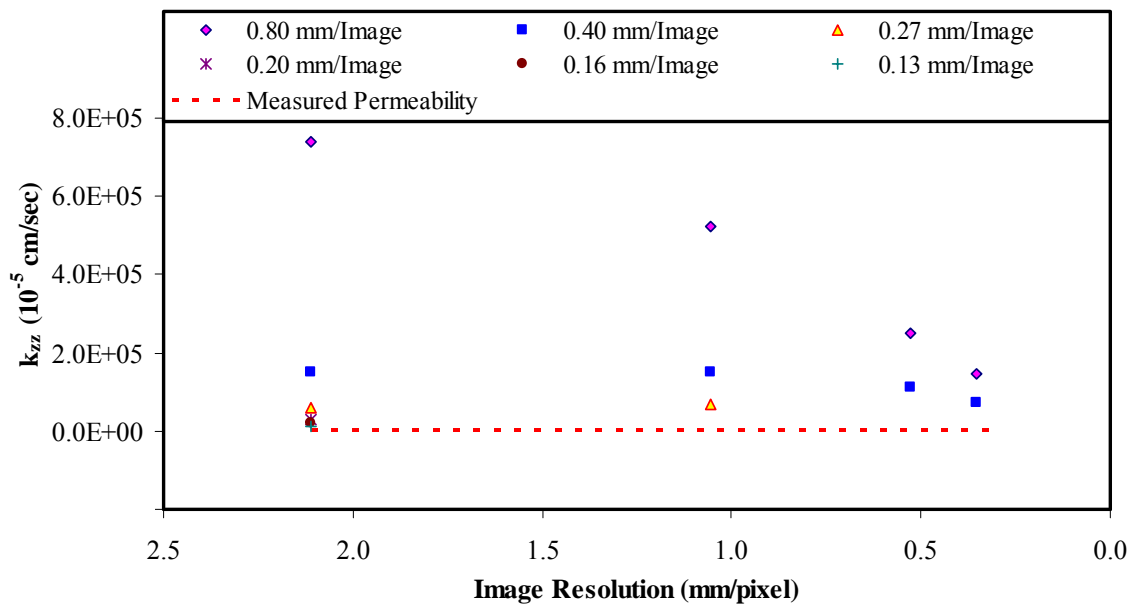
Fig. 6.4. Permeability, k_{zz}, of an asphalt mix specimen for different image and thickness resolutions (pressure gradient is applied in the vertical direction)

The influence of image resolution in the direction perpendicular to the direction of the flow that is driven by the pressure gradient was also investigated. As shown in Fig. 6.4, the influence of image resolution that is perpendicular to the flow direction decreased significantly as the resolution in the flow direction became finer. In other words, one can use relatively coarse resolution in the direction perpendicular to the flow direction provided that a resolution that is fine enough is used in the flow direction. The simulations presented in this study are based on a vertical resolution around 0.13 mm/pixel and a horizontal resolution around 2.1 mm/pixel when pressure gradient is applied in the vertical direction.
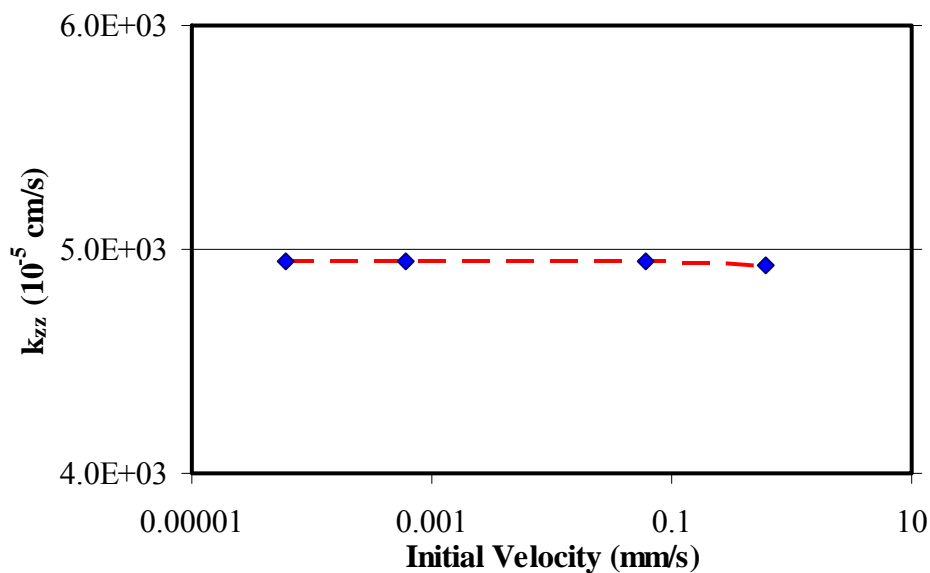
Fig. 6.5. Permeability, k_{zz}, at different initial velocity values

Similar to the analysis done for the idealized microstructures (Fig. 5.14), it was found that permeability of HMA mixes was constant and did not depend on the assumed initial velocity (Fig. 6.5).

Simulation of Fluid Flow Using Connected Air Voids

Air voids in the idealized 3-D microstructures discussed in Chapter V are all connected and involved in the fluid flow process. Unlike these standard microstructures, not all of the air voids in the actual 3-D porous microstructures are connected. In this study, X-ray CT images were processed according to the procedure described in Chapter III to identify the connected voids and eliminate the isolated voids. This preprocessing step improved the efficiency of the program since the program does not have to solve for fluid flow in isolated voids that are known a priori not to have flow in them.

Most of the LKC specimens from Romero (2000) showed connectivity in their air voids, while most of field cores from Cooley et al. (2002a) showed no connectivity. The field permeability measured on these cores is mainly due to flow in the top 25 mm of the pavement (Masad et al. 2004). For the open-graded specimens from Watson et al. (2004), 95% to 99% of all the air voids were found to be connected. Fig. 6.6 shows the relation between the total and connected percent air voids for the LKC and open-graded specimens.

Fig. 6.6. Relation between total and connected % of AV for the LKC and OG specimens

The SGC specimens from Birgisson et al. (2003) showed no connectivity. This can be attributed to the highly non-uniform distribution of air voids in these specimens, where most of the voids were concentrated around the circumference of a specimen. Recall that square parts of the images were used in the simulation. These square images had no connectivity. This point is further illustrated by comparing one of the SGC specimens with another LKC specimen. Although the overall volume distributions of air voids in LKC and SGC specimens seem to be similar as shown in the example in Fig. 6.7, the air void distributions in the horizontal directions are totally different.

Fig. 6.7. Air void volume distribution for LKC-12 and SGC-11 specimens

(a) LKC-12   (b) SGC-11
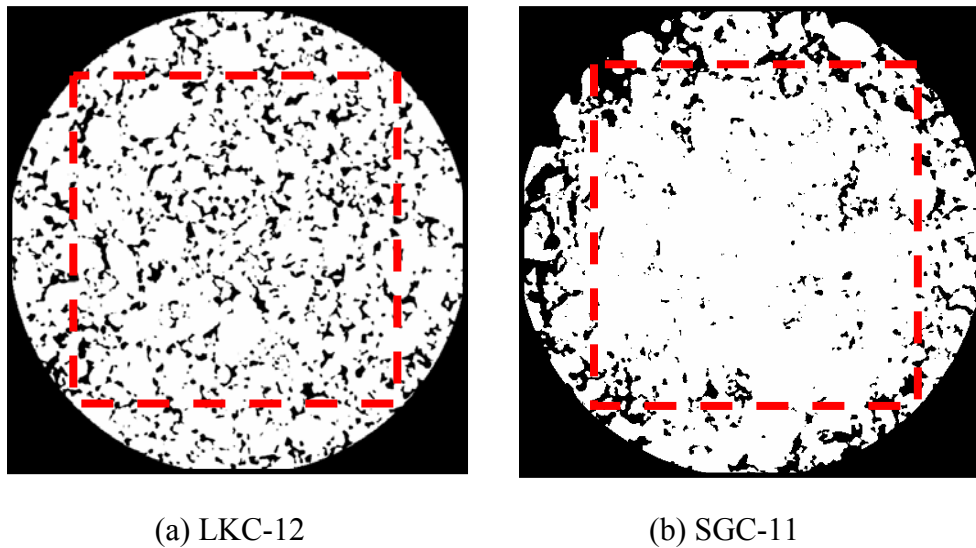
Fig. 6.8. Examples of typical air void distribution in horizontal plain of LKC and SGC specimens

Fig. 6.8 shows an example of air void distribution in the horizontal plane for the two specimens that are used in Fig. 6.7. Air voids were more uniformly distributed in the LKC specimens while air voids were concentrated at the circumference of the SGC specimens. Therefore, most of the connectivity in the SGC specimens is lost when only the square part of the image is used in simulating fluid flow in these SGC specimens.

Fluid Flow Simulation Output

The model simulates steady-state fluid flow in 3-D microstructures of HMA mixes. The main output of the model is the permeability of HMA mixes calculated using Darcy's law. The components of the permeability tensors can be evaluated using this numerical model. In addition to permeability, the simulation model provides the distribution of the velocity and pressure within the analyzed HMA 3-D microstructures.

Fig. 6.9 shows an example of the velocity distribution in a vertical section of an HMA specimen. The simulated fluid flow in this specimen is driven by pressure gradient applied from the top to the bottom of the specimen. In this figure, most of the velocity vectors point downward, that is the flow direction. An example of pressure distribution in a horizontal image is shown in Fig. 6.10. This figure shows that the pressure gradient appears only in the air voids while the solid parts have zero pressure gradients. Pressure value in the void changes either steeply (as shown in the exaggerated part of Fig 6.10) or gently as shown in other parts of Fig 6.10 indicating the simulated flow pattern.
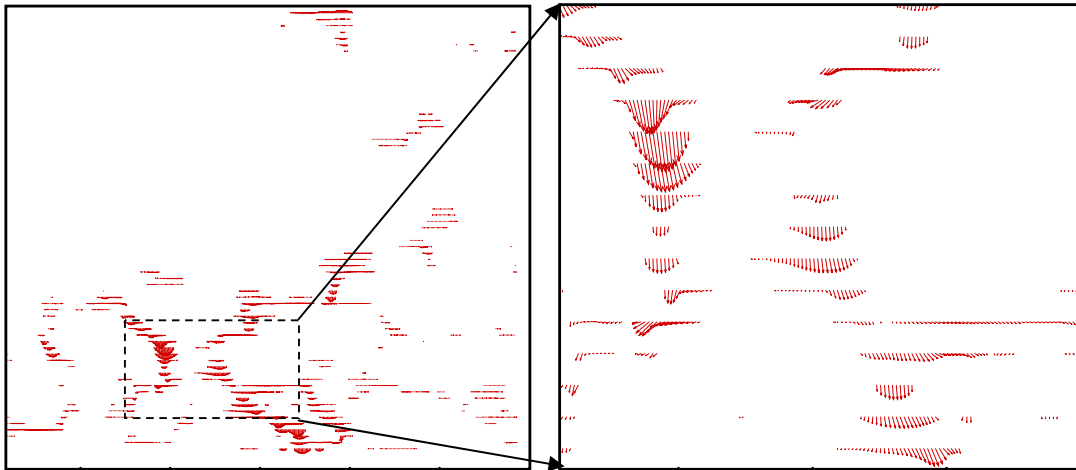
Fig. 6.9. Velocity distribution for a vertical section in an LKC-09 asphalt specimen
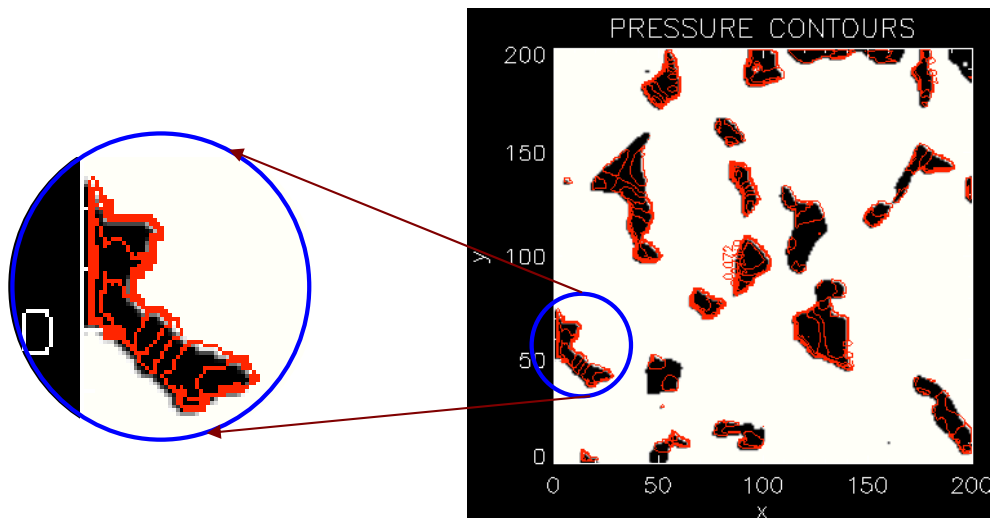
Fig. 6.10. Pressure distribution in a horizontal section of an HMA specimen
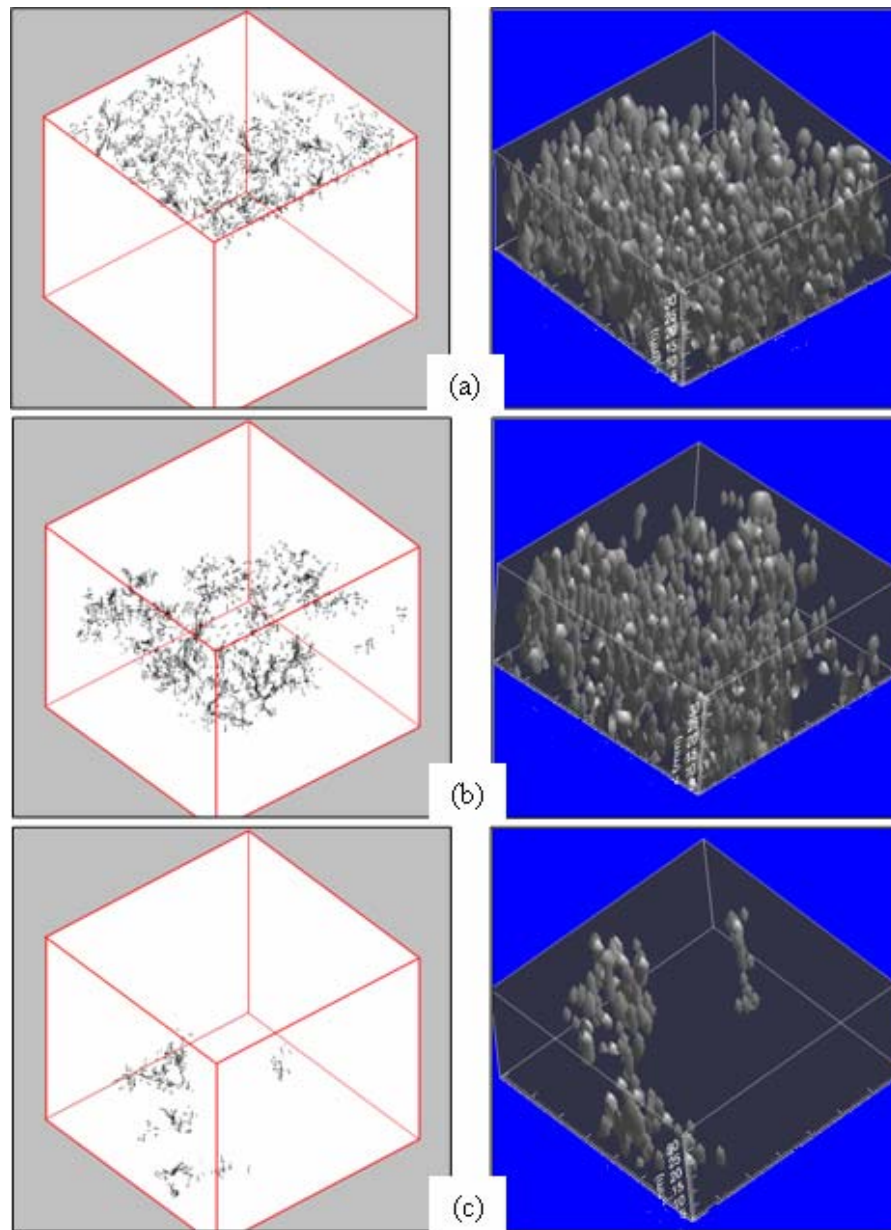
Fig. 6.11. Flow patterns (left) and the corresponding air void structures (right) for the
(a) Top, (b) Middle, and (c) Bottom part of HMA specimen

3-D simulation of fluid flow in an HMA microstructure is shown in Fig. 6.11 along with the air void structures. The simulation shows fluid flow in the top, middle, and bottom regions. It can be seen that flow is definitely non-uniform. Large portions of specimens have no connected voids, and consequently, no flow exists in these regions. Also, velocity vectors vary in their length indicating the influence of bottlenecks and air void structure on fluid flow within the connected voids.

Table 6.2. Calculated Permeability (k_{zz}) of the LKC and OG Specimens

Sample	% n_{eff}	Calculated k_{zz} (10^{-5} cm/sec)
LKC-01	7.25	4948.05
LKC-02	5.84	4944.00
LKC-03	9.04	9116.66
LKC-04	11.40	9837.21
LKC-05	3.32	1916.93
LKC-06	0.00	0.00
LKC-07	8.50	8269.83
LKC-08	0.00	0.00
LKC-09	0.00	0.00
LKC-10	15.17	29798.75
LKC-11	0.00	0.00
LKC-12	8.30	11688.31
LKC-13	8.55	7847.51
LKC-14	8.98	7126.73
OG-SGC-01	18.75	125911.2
OG-SGC-02	22.03	142465.5
OG-SGC-03	21.30	84908.3
OG-SGC-04	20.67	95561.0
OG-SGC-05	21.89	209002.6
OG-SGC-06	22.98	253226.2
OG-SGC-07	18.47	70323.2
OG-MAR-08	20.18	103159.0
OG-MAR-09	14.08	39625.0
OG-MAR-10	12.40	15123.4

Comparing Simulation Results to Laboratory Permeability Measurements

The fluid flow simulation was performed using connected air voids only. The permeability measurements reported for the LKC specimens (Table 3.1) were compared with model permeability results in the vertical direction, which are reported in Table 6.2. As shown in Fig. 6.12, the model results have reasonable correlation with the experimental measurements with R^2=0.65. It was found that cutting square sections from the X-ray CT images for the numerical simulation resulted in specimens with no connected air voids and zero calculated permeability. This was the case for specimens LKC-08, LKC-09, and LKC-11, which had small measured permeability values as indicated in Table 3.1. Both the experimental measurements and numerical analysis gave zero permeability for LKC-06.
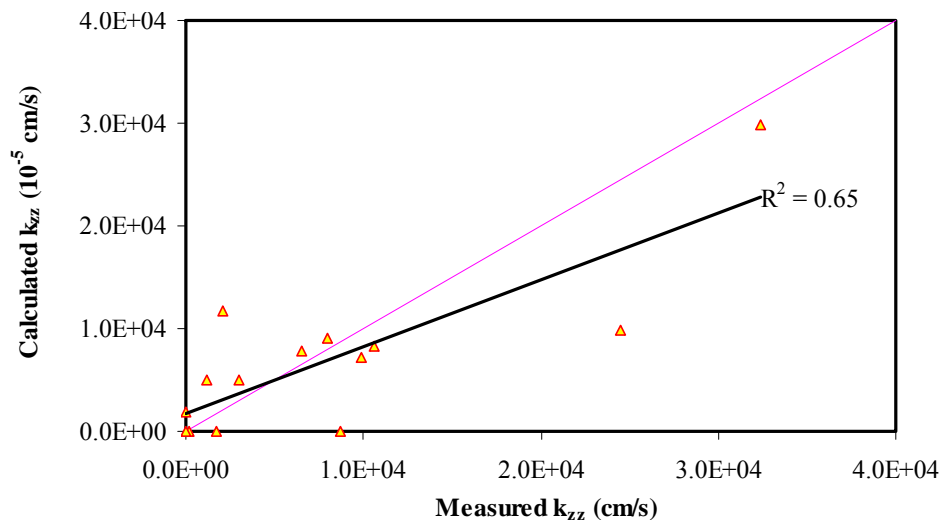
Fig. 6.12. Comparison of calculated to measured permeability for the LKC specimens

Fig. 6.13 shows that excellent correlation exists between numerical results of permeability and connected percent air voids (% n_{eff}). The relationship between applied pressure and calculated permeability was investigated to determine the flow characteristics in LKC specimens. It was found that calculated permeability is independent of the applied pressure. In other words, a linear relationship exists between pressure gradient and velocity indicating that the flow can be described as creeping flow at the macroscopic level. However, this does not mean that creeping flow exists at all points in the microstructure. In fact, the fluid flow simulations, as evident in Fig. 6.11, indicate the non-uniform distribution of fluid velocity in the microstructure, which causes some parts of the microstructure to experience inertial flow as well.
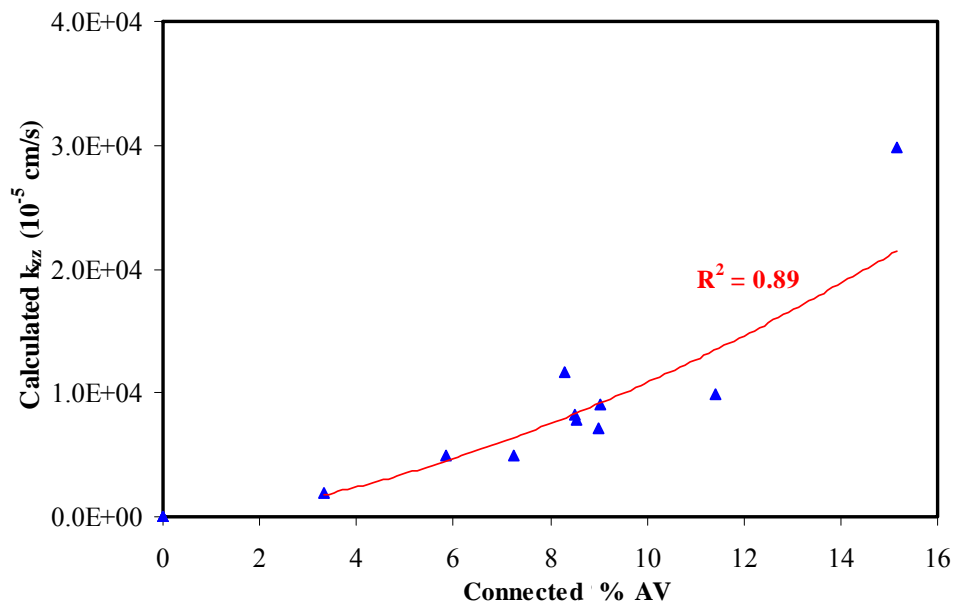
Fig. 6.13. Calculated permeability vs. connected % AV of the LKC specimens

Fluid flow simulations were also conducted for the OG specimens, and the results are shown in Table 6.2 for very small pressure gradients; the hydraulic gradients (i) are around 10^{-4}. The OG specimens labeled with SGC where compacted using the Superpave gyratory compactor up to the number of gyrations included in their labels. The OG specimens labeled with MAR were, on the other hand, compacted using the Marshall compactor up to the number of blows included in their labels.
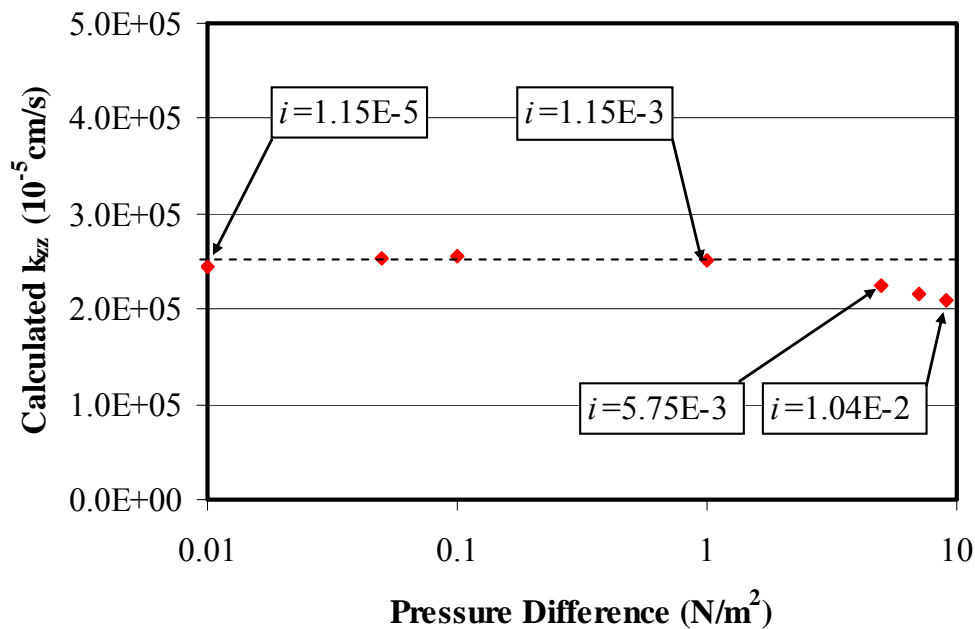
Fig. 6.14. Permeability, k_{zz}, at different pressure difference (and corresponding hydraulic gradient) values for the OG specimens

For these OG specimens, the simulation was conducted at different pressure gradients, and it was found that the permeability decreased after a certain pressure gradient was

applied as shown in Fig. 6.14. This indicates that the pressure gradient-velocity relationship deviates from the linear behavior due to inertial flow in these OG specimens. The Reynolds cell number was calculated in the OG specimens and found to be in the range of 0.003 and to reach as high as 4.823. Recall that the developed numerical simulation program can handle inertial flow due to the presence of the nonlinear terms in the Navier-Stokes equations. Also, the exponential scheme was implemented to be able to accommodate the change in the type of flow from creeping flow to inertial flow.
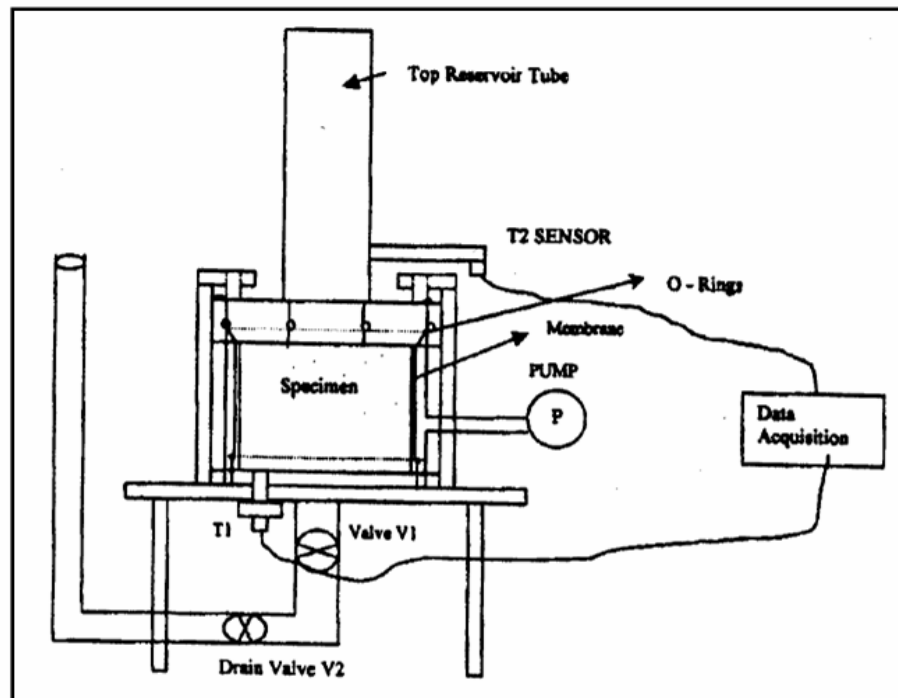
Fig. 6.15. Dual mode permeameter (after Huang et al. 1999)

This finding about the nonlinear pressure gradient-velocity relationship is consistent with experimental findings reported by Huang et al. (1999) using the experimental setup shown in Fig. 6.15. They indicated that the linear relationship exists only for a hydraulic gradient less than 0.01, and Darcy's law will not be valid if the permeability test is performed using larger hydraulic gradients.
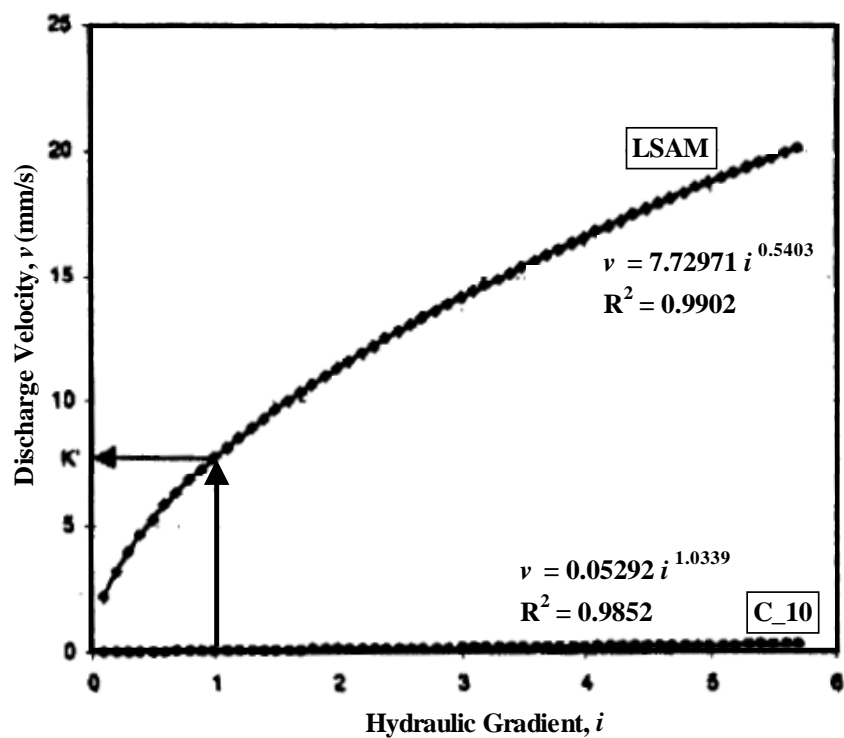
Fig. 6.16. Discharge velocity vs. hydraulic gradient (after Huang et al. 1999)

Fig. 6.16 shows an example of the results reported by Huang et al. (1999). The curve labeled (LSAM) refers to gap-graded specimens such as the Open-Graded Friction Course specimens, while the curve labeled (C-10) is typical for dense-graded specimens that obey Darcy's law at a wide range of pressure gradients. Huang et al. (1999) supported the recommendation by Tan et al. (1997) to use the pseudo-coefficient of permeability (k') measured at a hydraulic gradient of 1.0 to compare the permeability values of different OG specimens.

The numerical results for OG permeability reported in Table 6.2 are within the range of permeability measurements reported by Huang et al. (1999). It is interesting to note that specimens with almost the same percent air voids had very different permeability values. For example, OG-SGC-02 and OG-SGC-06 had approximately the same percent air voids, but OG-SGC-06 had about twice the permeability of OG-SGC-02. However, as evident in Fig. 6.17, there is still very good correlation between effective percent air voids and permeability.

Comparison of Permeability Results with Closed Form Solutions and Limits

Calculated permeability values are compared to the analytically derived permeability limits or closed-form solutions by Ergun (1952) and Berryman and Blair (1986). Ergun's model and Berryman-Blair's permeability upper limit calculate permeability assuming that the material consists of spherical particles. The permeability is then calculated using two parameters: the porosity and the average radius of the particles. Ergun's model is

shown in Eq. (5.126) while Berryman-Blair's permeability upper limit is shown in Eq. (6.1) that gives an upper limit for the permeability. In Eq. (6.1), R is the average radius of spherical particles, and ε is the porosity.

$$K \leq \frac{16}{81} \frac{\varepsilon^3 R^2}{(1-\varepsilon)^2} \qquad (6.1)$$
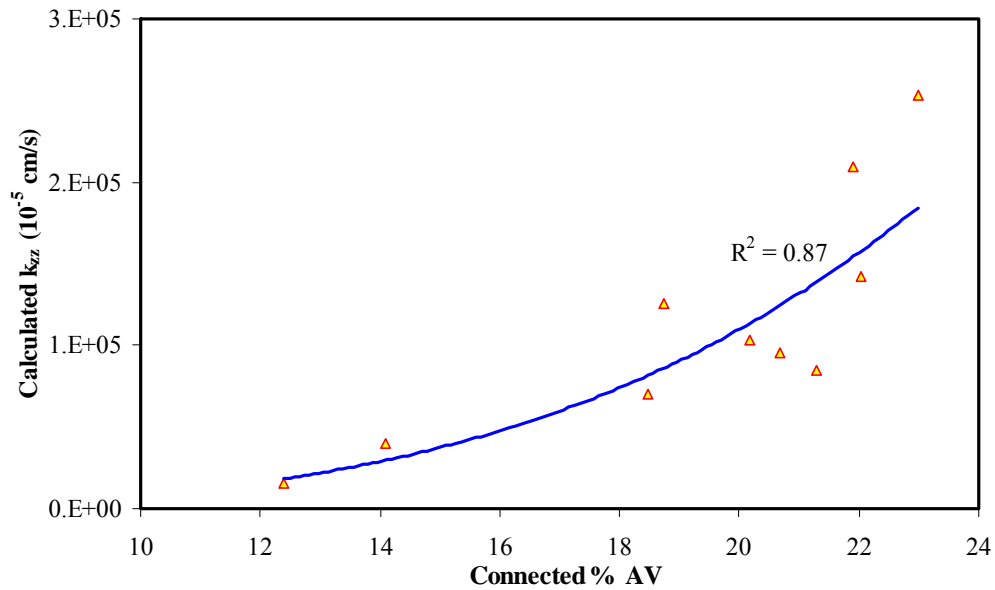
Fig. 6.17. Calculated permeability vs. connected % AV of the OG specimens

Permeability estimated using the closed-form solution and the permeability upper limit depends on the radius of the spheres; therefore, the average particle sizes for the different mixes were used. A maximum value for particle size of 8.70 mm (R=4.35 mm)

and a minimum of 3.70 mm (R=1.85 mm) were chosen based on the gradations of the LKC and OG HMA mixes. These maximum and minimum particle sizes were corrected for the effect of asphalt content using Eq. (4.09). The new maximum and minimum mix particle sizes are 10.25 mm (R=5.13 mm) and 4.33 mm (R=2.17 mm), respectively.
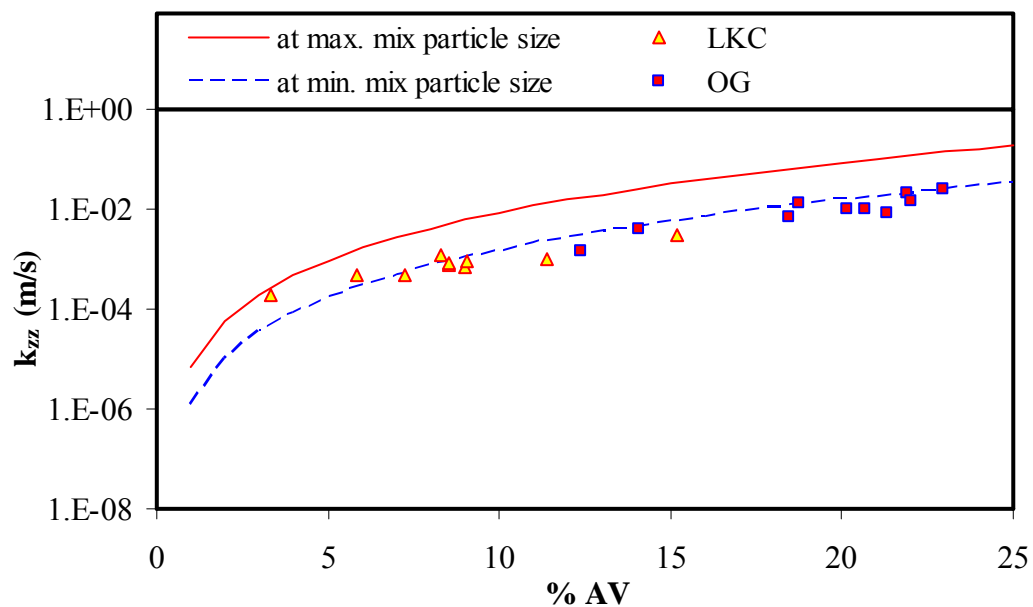
Fig. 6.18. Comparison of Ergun's model to the numerical permeability results

Figs. 6.18 and 6.19 show the comparisons of the results of the analyzed LKC and OG HMA specimens to the results from Ergun's closed-form solution and Berryman-Blair's permeability upper limit, respectively. These two figures show that most of the numerical results are less than the maximum and minimum limits of Ergun's

closed-form solution. It is shown also that all of the numerical results are less than Berryman-Blair's upper limit for the maximum or the minimum particle sizes. This is attributed to the non-uniform distribution of air voids as the HMA microstructure does not comply with the assumption of being composed of spherical particles with all air voids connected.
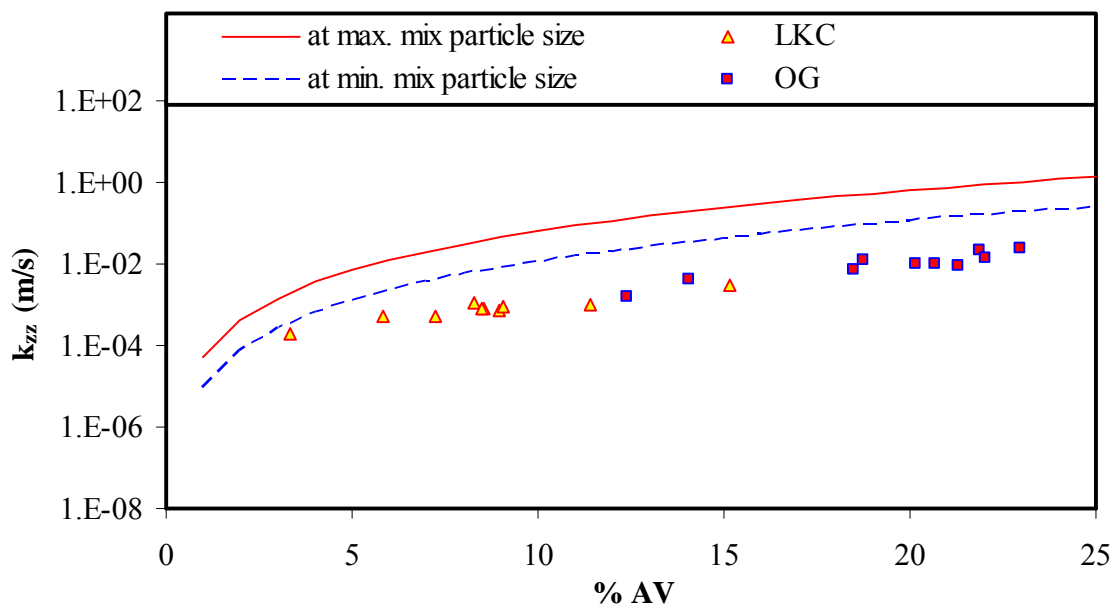
Fig. 6.19. Comparison of Berryman-Blair's limit with numerical permeability results

Calculation of Permeability Tensor Components and Anisotropy

As described in Chapter V, the components of the permeability tensor can be calculated through simulating fluid flow in three perpendicular directions (the vertical z-direction

and the horizontal x- and y-directions). The driving force of the simulated fluid flow in each direction is the pressure difference applied in that direction only. Three components of the permeability tensor are evaluated at the end of the fluid flow simulation in each of the three directions. All nine components are calculated after the three simulations are accomplished using Eqs. (5.120) and (5.121). In this part of the study, fluid flow simulation in the three directions was performed using comparable number of computational cells in all three dimensions.

Table 6.3 shows the numerically calculated results for some of the LKC and OG HMA specimens. The calculated results showed some discrepancy as the tensor was not symmetric. The heterogeneous distribution of air voids contributed to this discrepancy. For example, more air voids can be present at the microstructure boundary next to where the pressure is applied in the x-axis, while mostly solid material can be present at the boundary where the pressure is applied in the y-direction. Therefore, the solutions for these two cases are not expected to give the same exact values for k_{xy} and k_{yx} due to numerical errors. However, it was found that the differences between the off-diagonal components are very small, and they were deemed insignificant especially that they were less than 15% of the permeability in the vertical direction and less than 5% of the permeability in the horizontal direction. Therefore, it was decided to average the off-diagonal components to obtain a symmetric tensor. This is the off-diagonal elements; k_{xy}, k_{xz}, and k_{yz} were averaged with k_{yx}, k_{zx}, and k_{zy}, respectively. It can be seen from Table 6.3, that the horizontal permeability (k_{xx} or k_{yy}) is higher than the vertical

permeability (k_{zz}). Also, permeability values in the horizontal directions (k_{xx} and k_{yy}) are almost equal.

Table 6.3. Permeability Tensor for Some LKC and Open-Graded HMA Specimens

Sample	Permeability (cm/sec)		
	k_{xx}	k_{xy}	k_{xz}
	k_{yx}	k_{yy}	k_{yz}
	k_{zx}	k_{zy}	k_{zz}
LKC-01	0.794	-0.004	0.018
	-0.004	0.755	-0.005
	0.018	-0.005	0.070
LKC-12	0.900	0.001	0.005
	0.001	0.969	0.014
	0.005	0.014	0.108
LKC-13	0.947	0.004	-0.009
	0.004	0.910	-0.005
	-0.009	-0.005	0.088
LKC-14	1.059	-0.001	0.002
	-0.001	1.028	-0.020
	0.002	-0.020	0.096
OG-SGC-04	8.655	0.066	-0.020
	0.066	9.187	0.019
	-0.020	0.019	2.769
OG-SGC-07	9.081	-0.032	-0.017
	-0.032	8.905	0.029
	-0.017	0.029	2.259
OG-MAR-08	8.458	-0.028	-0.014
	-0.028	10.106	0.270
	-0.014	0.270	4.319
OG-MAR-10	1.771	-0.003	0.012
	-0.003	1.723	-0.007
	0.012	-0.007	1.044

The principal directions or eigen vectors of the permeability tensor were also determined and reported in Table 6.4. The corresponding principal angles (θ and ϕ) were calculated using the unit vector shown in Fig. 6.20. This unit vector can be written as three Cartesian components ($\hat{i}, \hat{j}, \hat{k}$) in the x-, y- and z-directions, respectively, where $\hat{i} = \sin\theta \cos\phi$, $\hat{j} = \sin\theta \sin\phi$, and $\hat{k} = \cos\theta$. The results of k_{xx}/k_{zz}, k_{yy}/k_{zz}, k_{yy}/k_{xx} are shown in Table 6.5.
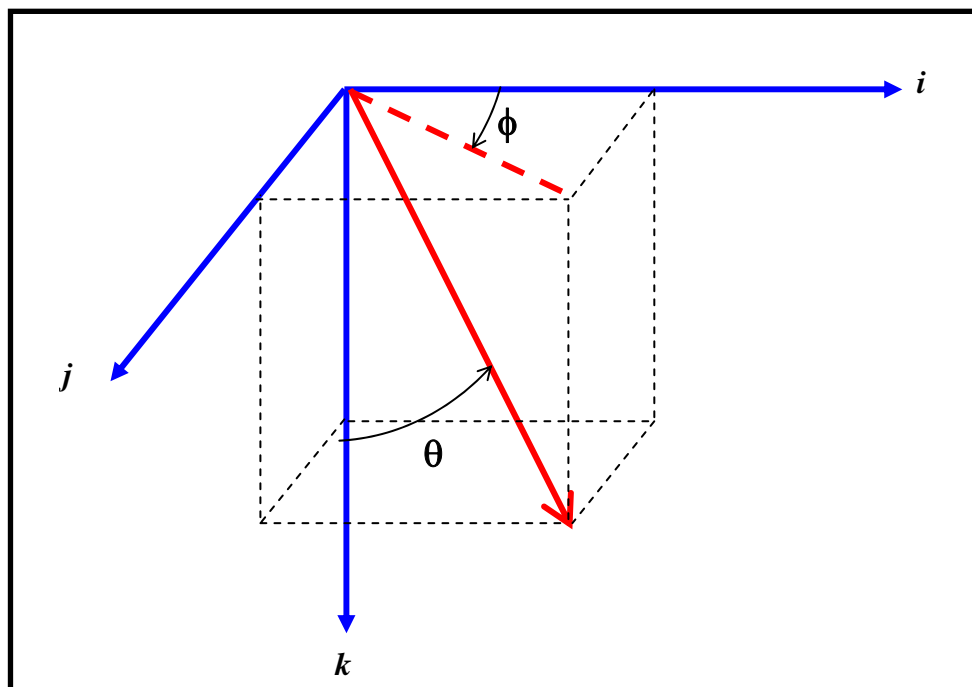
Fig. 6.20. Unit vector that is used in calculating the principal angles θ and ϕ

Table 6.4. Principal Permeability and Principal Directions for the LKC and Open-Graded HMA Specimens Shown in Table 6.3

Sample	Principal Permeability (cm/sec)		Principal Directions				
			$\hat{i}$	$\hat{j}$	$\hat{k}$	θ (°)	ϕ (°)
LKC-01	k_{11}	0.795	0.993681	-0.109247	0.025754	88.5	-6.3
	k_{22}	0.755	0.109392	0.993989	-0.004310	90.2	83.7
	k_{33}	0.069	-0.025129	0.007100	0.999659	1.5	-15.8
LKC-12	k_{11}	0.969	0.015184	0.999759	0.015833	89.1	89.1
	k_{22}	0.900	0.999866	-0.015279	0.005945	89.7	-0.9
	k_{33}	0.108	-0.006185	-0.015740	0.999857	1.0	68.5
LKC-13	k_{11}	0.948	0.993590	0.112532	-0.010717	90.6	6.5
	k_{22}	0.910	-0.112587	0.993631	-0.004673	90.3	-83.5
	k_{33}	0.088	0.010123	0.005849	0.999932	0.7	30.0
LKC-14	k_{11}	1.059	0.998909	-0.046612	0.002699	89.8	-2.7
	k_{22}	1.029	0.046658	0.998693	-0.020845	91.2	87.3
	k_{33}	0.096	-0.001724	0.020948	0.999779	1.2	-85.3
OG-SGC-04	k_{11}	9.195	0.121343	0.992607	0.002558	89.9	83.0
	k_{22}	8.647	0.992605	-0.121334	-0.003706	90.2	-7.0
	k_{33}	2.768	0.003368	-0.002989	0.999990	0.3	-41.6
OG-SGC-07	k_{11}	9.086	0.984951	-0.172804	-0.003211	90.2	-10.0
	k_{22}	8.899	0.172816	0.984947	0.003803	89.8	80.0
	k_{33}	2.259	0.002506	-0.004300	0.999988	0.3	-59.8
OG-MAR-08	k_{11}	10.120	-0.017480	0.998762	0.046568	87.3	-89.0
	k_{22}	8.458	0.999843	0.017603	-0.002223	90.1	1.0
	k_{33}	4.306	0.003040	-0.046522	0.998913	2.7	-86.3
OG-MAR-10	k_{11}	1.771	0.997972	-0.061291	0.017170	89.0	-3.5
	k_{22}	1.723	0.061458	0.998066	-0.009386	90.5	86.5
	k_{33}	1.044	-0.016561	0.010422	0.999809	1.1	-32.2

Useful observations can be obtained from the results shown in Tables 6.3, 6.4, and 6.5. It can be noticed that the k_{yy}/k_{xx} is around one and the off-diagonal matrix components very small compared with the diagonal values. The other observation is that the major

principal direction is always less than 5 degrees from the horizontal direction
($85°<\theta<90°$). The minor principal direction, on the other hand, is always less than 5
degrees from the vertical direction ($0°<\theta<5°$).

Table 6.5. Permeability Anisotropy for the LKC and Open-Graded HMA Specimens
Shown in Table 6.3

Sample	Permeability Anisotropy		
	k_{xx}/k_{zz}	k_{yy}/k_{zz}	k_{yy}/k_{xx}
LKC-01	11.40	10.84	0.95
LKC-12	8.35	8.99	1.08
LKC-13	10.71	10.29	0.96
LKC-14	11.00	10.68	0.97
OG-SGC-04	4.02	3.94	0.98
OG-SGC-07	1.96	2.34	1.20
OG-MAR-08	3.13	3.32	1.06
OG-MAR-10	1.70	1.65	0.97

Based on the previous observations, the permeability can be considered to have
transverse anisotropic distribution with the horizontal direction being the major
direction, and the vertical direction is the minor direction. This is consistent with
previous findings based on the analysis of preferred orientation of aggregates in HMA.

Masad et al. (1999a) and (1999b) have shown the aggregate orientation to exhibit anisotropic distribution where the major axis is inclined very close to the horizontal. It is expected that the orientation of the long dimensions of particles is associated with the direction of long dimensions of air voids, which would lead to more connected air voids in the horizontal direction compared with the vertical direction.

The ratios of k_{xx}/k_{zz} and k_{yy}/k_{zz} were found to be between 8.35 and 11.40 for LKC and between 1.65 and 4.02 for OG specimens. Experimental measurements by Tan et al. (1999) showed that the ratio of the horizontal permeability to the vertical permeability in typical mixes in Singapore was between 1.05 and 2.49. Masad et al. (2002b) had studied the anisotropy of permeability in 2-D porous microstructures of glass beads, Ottawa sand, and silica sand. They found that these materials exhibited transverse anisotropy in terms of the particle directional distribution. Also, the ratio between the permeability of the two horizontal directions (k_{xx} and k_{yy}) was between 1.02 and 1.20.

Using the permeability tensor from Table 6.3, the directional distribution of the permeability, $k\ (\theta, \phi)$, of the HMA specimens can be estimated using Eq. (6.2) where $k_{Average}$ is the average of the diagonal elements of the permeability tensor; k_{xx}, k_{yy}, and k_{zz}. In Eq. (6.2), k'_{ij} are the elements of the deviatoric tensor $[k']$ that is defined in Eq. (6.3) with the i or j subscripts taking the values of x, y, or z. In Eq. (6.2), $l_x = \sin\theta \cos\phi$, $l_y = \sin\theta \sin\phi$, and $l_z = \cos\theta$.

$$k\left(\theta,\phi\right) = k_{Average} + k'_{ij} l_i l_j \tag{6.2}$$

$$[k'] = \begin{bmatrix} k_{xx} - k_{Average} & k_{xy} & k_{xz} \\ k_{yx} & k_{yy} - k_{Average} & k_{yz} \\ k_{yx} & k_{yz} & k_{zz} - k_{Average} \end{bmatrix} \tag{6.3}$$

Fig. 6.21 shows an example of the directional distribution of the permeability for the OG-SGC-07 specimen in two planes: the horizontal plane with θ=90° in Fig. 6.21 (a) and the vertical plane with φ=0° in Fig. 6.21 (b).

Summary

This chapter discussed the results from the numerical simulation of fluid flow in the material microstructure. The output obtained from the simulation includes the pressure distribution and the velocity distribution in the microstructure, and the permeability tensor components. It was found the fluid flow in the dense-graded specimens compacted using LKC can be considered as creeping flow at the macroscopic level. However, the inertial flow can play a role in certain regions within the microstructure due to the highly heterogeneous and non-uniform flow velocity distribution. The OG specimens were shown to exhibit inertial flow at certain values of pressure gradient.
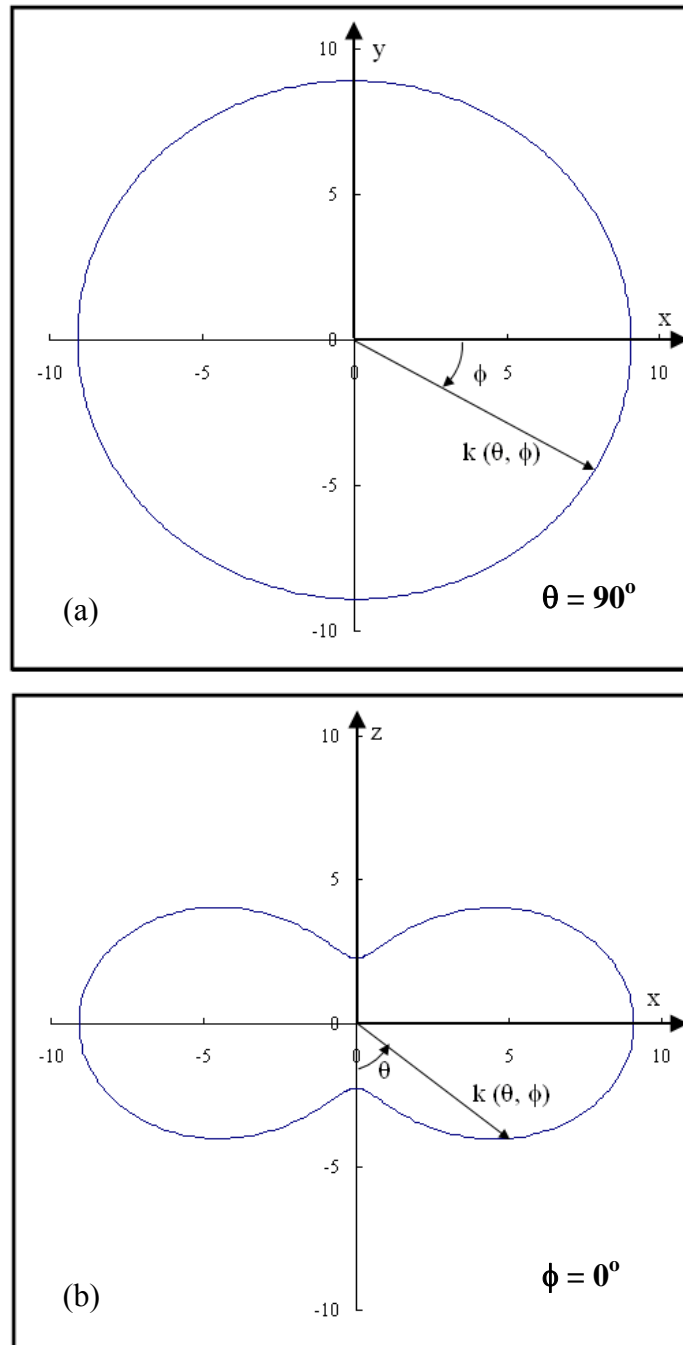
Fig. 6.21. Polar diagram of directional distribution of permeability on (a) A horizontal

plane ($\theta = 90°$) and (b) A vertical plane ($\phi = 0°$)

The calculated permeability values had very good correlation with experimental measurements and with the percentage of connected air voids. The permeability directional distribution was found to exhibit transverse anisotropy with the major principal direction oriented toward the horizontal. The ratio of horizontal permeability to vertical permeability was between 8.35 and 11.40 for dense-graded specimens and between 1.65 and 4.02 for OG specimens.

CHAPTER VII

SUMMARY, CONCLUSIONS, AND RECOMMENDATIONS

The first section of this chapter presents a summary of the tasks and the main conclusions of this dissertation. The other section presents some recommendations for further research on the analysis of fluid flow in porous media in general and asphalt mixes in particular.

Summary and Conclusions

The presence of free water within asphalt pavements is known to reduce their load carrying capacity through promoting distresses such as moisture cohesive and adhesive damage, fatigue cracking, and permanent deformation. The literature review focused on the basic principles of fluid flow in porous media in general and asphalt mixes in particular. It also discussed the different models that have been proposed to predict permeability of porous materials.

The different permeability models discussed in the literature were developed based on various approaches. The analytical approach relies on assuming certain shapes and connectivity for the pores and quantifying the pore structure using average quantities such as porosity, tortuosity, cross-sectional area, and specific surface area. The numerical approach is based on simulating fluid flow in the material microstructure and using Darcy's law to calculate permeability given the fluid velocity distribution and

pressure gradient. Most of the work on HMA permeability has focused on developing relationships between the measured permeability and the average percent air voids without giving enough considerations to the differences in air void distributions among HMA mixtures.

The first objective of this study was to develop an analytical-empirical approach for the analysis of HMA permeability through the characterization of the microstructure using X-ray CT and image analysis techniques. The 3-D microstructure of HMA mixes that were prepared using a wide range of materials and compacted using different methods and different percent of air voids were captured using X-ray CT. Image analysis techniques were developed to quantify the size distribution of air voids, the percentage of connected air voids (effective porosity), tortuosity of flow paths, and specific surface area of air voids. These parameters were used in the Kozeny-Carman equation, which was found to provide reasonable predictions of HMA permeability. Consequently, efforts were directed at developing modified versions of the Kozeny-Carman equation such that permeability can be predicted using quantities that can be easily measured in the laboratory as part of the routine characterization of HMA rather than those measured using X-ray CT.

The first modified version of the Kozeny-Carman equation, Eq. (4.5), was developed based on expressing effective percent air voids and tortuosity as power functions of total percent air voids. These functions were established based on the analysis of X-ray CT

images. In addition, the specific surface area of air voids was found to be a function of the specific surface area of aggregates, which was determined based on aggregate gradations.

The second modified version of the Kozeny-Carman equation, Eq. (4.14), was based on the work of Dr. Lytton at Texas A&M University, where an equivalent particle diameter is used in the Kozeny-Carman equation to reflect the average particle size and the amount of asphalt. The modified versions of the Kozeny-Carman equation were used to match a comprehensive database of permeability measurements of a wide range of HMA mixes from previous studies. A calibration coefficient was needed in each of the equations in order to improve the predictions of the permeability measurements. The calibration coefficients were found to depend primarily on the method used to measure permeability and on percent air voids. It is known that the methods available for measuring HMA permeability differ in their ability to verify specimen saturation prior to permeability measurements, their control over water leakage around the circumference of a specimen, and their precision in recording pressure gradient and flow speed. All these factors made it necessary to include a calibration coefficient to better predict permeability. It is envisioned that the calibrated equations can be used by pavement engineers to give reasonable predictions of HMA permeability.

The other major objective of this study was to develop a program for numerical simulation of fluid flow in 3-D microstructures of porous materials. The program solves

the governing fluid flow equations; the continuity equation and the Navier-Stokes equations, for steady and incompressible flow. This solution has several advantages over the available programs for the simulation of fluid flow in the microstructure of porous materials. Primarily, the model solves the full Navier-Stokes equations within the boundary conditions of the material microstructure by taking into account both the creeping and inertial forces. Previous studies, however, have assumed the flow to be governed by creeping forces and solved the Stokes equations only. The model uses the non-staggered grid system that utilizes only one computational cell to solve the governing equations, which simplifies the numerical implementation. Most of the previous studies used the staggered grid system, which uses two staggered computational cells in solving the governing equations; one is for solving the continuity equation while the other one is used for the Navier-Stokes equations. The outputs of the numerical solution are the components of the permeability tensor, the velocity distribution within the microstructure, and pressure distribution within the microstructure.

The numerical model was used to analyze fluid flow characteristics in a wide range of HMA mixes. The 3-D microstructure was captured using X-ray CT. Image voxels were treated as the computational cells used to solve the governing equations. The efficiency of the numerical solution was enhanced by processing the 3-D X-ray CT images in order to retain the connected air voids only and eliminate the nonconnected voids prior to the simulation. It was found that all the HMA mixes investigated in this study had

microscopic regions where inertial flow took place at the pressure gradients used in this study. However, the dense-graded mixes exhibited an overall constant permeability with an increase in pressure gradient, while the open-graded mixes exhibited a reduction in permeability with an increase in pressure gradient. This means that creeping flow was dominant at the macroscopic level in the dense-graded mixes, while the inertial flow dominated the flow in the open-graded mixes.

The permeability results calculated using the numerical model correlated very well with permeability measurements. The permeability calculations were found to be at least an order of magnitude less than those predicted by closed-form solutions for idealized microstructure. The ratio of the horizontal permeability to vertical permeability was found to range from 8.35 to 11.40 for the dense-graded mixes while it ranged from 1.65 to 4.02 for the open-graded HMA specimens. In general, the permeability directional distribution can be described as axisymmetric with the major and minor principal directions coinciding with the horizontal and vertical directions, respectively.

Recommendations

The following recommendations are for future studies related to this dissertation:

- Use the developed empirical-analytical equations and numerical solution to analyze the permeability of a wide range of HMA mixes with different aggregate sources, aggregate size distribution, and compaction methods.

- The current X-ray CT capabilities and the need to scan specimens with representative volumes imposed limitations on the resolution of X-ray CT used in this study. Given the rapid advancement of X-ray CT, it is recommended that future studies use X-ray CT images with equal resolutions in all three directions and higher than the ones used in this study.

- Improve the experimental methods used to measure HMA permeability to have better control on specimen saturation, and eliminate leakage at the specimen boundary. These factors can have significant impact on the measured permeability. Once this is accomplished, the effect of saturation level can be separated from the effect of shape factor in Eq. (4.14), and consequently, enhance the predictions of this equation.

- Compare the numerical predictions of horizontal permeability to experimental measurements.

REFERENCES

AASHTO T-166, (2000). "Specifications for Superpave volumetric mix design." *Standard Specifications for Transportation Materials and Methods of Sampling and Testing, AASHTO Provisional Standards*, Washington, D.C.

Adler, P. M., Jacquin, C. G., and Quiblier, J. A. (1990). "Flow in simulated porous media." *Internat. J. Multiphase Flow*, 16(4), 691-712.

Allen, D. L., Schultz, Jr., D. B., and Fleckenstein, L. J. (2001). "Development and proposed implementation of a field permeability test for asphalt concrete." *Research Report: KTC-01-19/SPR216-00-1F*, Kentucky Transportation Center, Lexington, KY.

Al-Omari, A., and Masad, E. (2004). "Three dimensional simulation of fluid flow in X-ray CT images of porous media." *International Journal for Numerical and Analytical Methods in Geomechanics*, 28(13), 1327-1360.

Al-Omari, A., Tashman, L., Masad, E., Cooley, A., and Harman, T. (2002). "Proposed methodology for predicting HMA permeability." *Journal of the Association of Asphalt Paving Technologists*, 71, 30-58.

Arns, C. H., Knackstedt, M. A., Pinezzewski, W. V., and Lindquist, W. B. (2001). "Accurate estimation of transport properties from microtomographic images." *Geophys. Res. Lett.*, 28, 3361-3364.

ASTM D2434-68, (2000). "Standard test method for permeability of granular soils (constant-head)." *Annual Book of ASTM Standards, American Society for Testing and Materials,* 04.08, West Conshohocken, PA.

ASTM D5084-90, (1999). "Standard test method for measurement of hydraulic conductivity of saturated porous materials using a flexible wall permeameter." *Annual Book of ASTM Standards*, *American Society for Testing and Materials*, 04.09, West Conshohocken, PA.

ASTM E1441-00, (2003). "Standard guide for computed tomography (CT) imaging." *Annual Book of ASTM Standards*, *American Society for Testing and Materials*, 03.03, West Conshohocken, PA.

ASTM PS129-01, (2001). "Standard provision test method for measurement of permeability of bituminous paving mixtures using a flexible wall permeameter." *Annual Book of ASTM Standards*, *American Society for Testing and Materials*, D04.23, West Conshohocken, PA.

Auzerais, F. M., Dunsmuir, J., Ferreol, B., Martys, N., Olson, J., Ramakrishnan, T. S., Rothman, D. H., and Schwartz, L. M. (1995). "Transport in sandstone: a study based on three-dimensional mircotomography." *Report No. ISD-004-95-20*, Schlumberger-Doll Research, Ridgefield, CT.

Bear, J. (1972). *Dynamics of fluids in porous media*, American Elsevier Publishing Co., Inc., New York.

Berryman, J. G. and Blair, S. C. (1986). "Use of digital image analysis to estimate fluid permeability of porous materials: application of two-point correlation functions." *Journal of Applied Physics*, 60(6), 1930-1938.

Birgisson, B., Roque, R., and Page, G. C. (2003). "Evaluation of water damage using hot mix asphalt fracture mechanics." *Journal of the Association of Asphalt Paving Technologists*, 72, 450-482.

Blair, S. C., Berge, P. A., and Berryman, J. G. (1996). "Using two-point correlation functions to characterize microgeometry and estimate permeabilities of sandstones and porous glass." *Journal of Geophysical Research*, 101, 20359-20375.

Braz, D., Lopes, R. T., and da Motta, L. M. G. (1999), "Analysis of the percentage voids of test and field specimens using computerized tomography." *Nuclear Instruments and Methods in Physics Research A*, 422, 942-948.

Brown, E. R., Collins, R., and Brownfield, J. A. (1989). "Investigation of segregation of asphalt mixtures in the state of Georgia." *Transportation Research Record 1217*, Transportation Research Board, Washington, D. C., 1-8.

Buchanan, M. S. and Brown, R. E. (January 2001). "Effect of Superpave gyratory compactor type on compacted hot mix asphalt (HMA) density." *Transportation Research Record 1761*, Transportation Research Board, Washington, D. C., 50-60.

Carman, P. C. (1956). *Flow of gases through porous media*, Academic Press, New York.

Castelblanco, A., Masad, E., and Birgisson, B. "HMA moisture damage as a function of air void size distribution, pore pressure and bond energy." *Submitted for Review to the 84th Annual Meeting of the Transportation Research Board*.

Cecheitini, J. A. (1974). "Vibratory compaction of asphalt concrete pavements." *Journal of the Association of Asphalt Paving Technologists*, 43, 384-416.

Cedergren, H. R. (1974). *Drainage of highway and airfield pavements*, John Wiley & Sons, Inc., New York.

Chapuis, R. P., Gill, D. E., and Baass, K. (1989). "Laboratory permeability tests on sand: influence of the compaction method on anisotropy." *Can. Geotech. J.*, 26, 614-622.

Childs, E. C., and Collis-George, N. (1950). "The permeability of porous materials." *Proc. Roy. Soc. Lond*, A201, 392-405.

Choubane, B., Page, G., and Musselman, J. (1998). "Investigation of water permeability of coarse graded Superpave pavements." *Journal of the Association of Asphalt Paving Technologists*, 67, 254-276.

Christensen, D. W. (2001). "Requirements for voids in mineral aggregate for Superpave mixtures." *Quarterly Report to the National Cooperative Highway Research Program, Project 9-25,* Washington D.C.

Christensen, Jr., D. W. and Bonaquist, R. F. (2003). "Ternary property maps for asphalt concrete." *Asphalt Paving Technologists-Proceedings of Technical Sessions*, 72 Baton Rouge, Louisiana, 27-55.

Cooley, A. L. (1999). "Permeability of Superpave mixtures: evaluation of field permeameters." *National Center for Asphalt Technology Report 99-1,* Auburn University, Auburn, AL.

Cooley, Jr., A. L., and Brown, E. R. (2000). "Selection and evaluation of a field permeability device for asphalt pavements." *Transportation Research Record, TRB,* National Research Council, Washington, D.C., 1723, 73-82.

Cooley, Jr., A. L., Brown, R. E., and Maghsoodloo, S. (January 2001). "Development of critical field permeability and pavement density values for coarse-graded Superpave pavements." *National Center for Asphalt Technology Report 01-3,* Auburn University, Auburn, AL.

Cooley, Jr., A. L., Prowell, B. D., Brown, E. R., Hall, K., Button, J., and Davis, R. (2002a). "Issues pertaining to the permeability characteristics of coarse-graded Superpave mixes." *Association of Asphalt Paving Technologists-Proceedings of the Technical Sessions*, 71, Colorado Springs, CO, 1-29.

Cooley, Jr., A. L., Prowell, B. D., Hainin, M. R., Buchanan, M. S., and Harrington, J. (2002b). "Bulk specific gravity round-robin using the Corelok vacuum sealing device." *National Center for Asphalt Technology Report 02-11,* Auburn University, Auburn, AL.

Crowe, C. T. (1997). *Numerical methods in fluid mechanics*, CE 556 Class Notes. Washington State University, Pullman, Washington.

Darcy, H. (1856). *Les fontaines publiques de la Ville de Dijon*, Dalmont, Paris.

Dennis, M. J. (1989). "Industrial computed tomography." *Metal Handbook 9th Edition: Nondestructive Evaluation and Quality Control*, 17, 71-88.

Dullien, F. A. L. (1979). *Porous media: fluid transport and pore structure*, Academic Press, Inc., New York.

Ergun, S. (1952). "Fluid flow through packed columns." *Chemical Engineering Process*, 48, 89-94.

Flannery, B. P., Deckman, H. W., Roberge, W. G., and Amico, K. L. (1987). "Three-dimensional X-ray microtomography." *Science*, 237, 1439-1444.

Ford, M. C., and McWilliams, C. E. (1988). "Asphalt mix permeability." University of Arkansas, Fayetteville, Arkansas.

Fredlund, D. G., and Rahardjo, H. (1993). *Soil mechanics for unsaturated soils*, John Wiley & Sons, Inc., New York.

Fwa, T. F., Tan, S. A., and Chuai, C. T. (1998). "Laboratory permeability measurement of base materials using falling-head test apparatus." *Transportation Research Record, TRB*, National Research Council, Washington, D.C., 1615, 94-99.

Garcia-Bengochea, I. (1978). The relation between permeability and pore size distribution of compacted clayey silts." M.S. thesis, Purdue University, West Lafayette, IN.

Gogula, A., Hossain, M., Romanoschi, S., and Fager, G. A. (2003). "Correlation between the laboratory and field permeability values for the Superpave

pavements." *Proceedings of the 2003 Mid-Continent Transportation Research Symposium*, Ames, IA.

Grangeat, P. (1991). "Mathematical framework for cone beam 3D reconstruction via the first derivative of the Radon transform," *Mathematical Methods in Tomography*, 1497, 66-97.

Hainsworth, J. M., and Aylmore, L. A. (1983). "The use of computer assisted tomography to determine spatial distribution of soil water content," *Aust. J. Soil Res*. 21, 435-443.

Holtz, R. D., and Kovacs, W. D. (1981). *Introduction to geotechnical engineering*, Prentice-Hall, Inc., New Jersey.

Huang, B., Mohammad, L., Raghavendra, A., and Abadie, C. (1999). "Fundamentals of permeability in asphalt mixtures." *Journal of the Association of Asphalt Paving Technologists*, 68, 479-500.

Hudson, S. B., and Davis, R. L. (1965). "Relationship of aggregate voidager to gradation." *Journal of the Association of Asphalt Paving Technologists*, 34, 574-593.

Image-Pro Plus, (1999). Version 4.1, Media Cybernetics, L.P, Georgia, MD.

Irmay, S. (1954). "On the hydraulic conductivity of unsaturated soils." *Transactions, American Geophysical Union*, 35(3), 463-467.

Juang, C. H., and Holtz, R. D. (1986). "A probabilistic permeability model and the pore size density function." *International Journal for Numerical and Analytical Methods in Geomaterials*, 10, 543-553.

Kandhal, P. S., and Mallick, R. B. (January 2001). "Effect of mix gradation on rutting potential of dense graded asphalt mixtures." *Transportation Research Record 1767*, Transportation Research Board, Washington, D. C., 146-151.

Kanitpong, K., Benson, C. H., and Bahia, H. U. (January 2001). "Hydraulic conductivity (permeability) of laboratory compacted asphalt mixtures." *Transportation Research Record 1767*, Transportation Research Board, Washington, D. C., 25-33.

Kim, Y. R, Little, D. N., and Lytton, R. L. (2004). "Effect of moisture damage on material properties and fatigue resistance of asphalt mixtures." *Annual Meeting of Transportation Research Board*, Washington, D.C.

Koplic, J., Lin, C., and Vermette, M. (1984). "Conductivity and permeability from microgeometry." *J. Appl. Phys.*, 56, 3127-3131.

Kozeny, J. (1927). "Ueber kapillare leitung des wassers im boden." Wiener, Akad., Wiss., 136(2A), 271-306.

Latini, R. G. (1967). "Measurement of directional permeabilities." M.S. thesis, Department of Chemical Engineering and Metallurgy, Syracuse University, Syracuse, NY.

Lindly, J. K., and Elsayed, A. S. (1995). "Estimating permeability of asphalt-treated bases." *Transportation Research Record, TRB,* National Research Council, Washington, D.C., 1492, 103-111.

Little, D. N. (2003). "Assessing damage in the mastic and fine aggregate phase." Aging of Pavement Asphalts Symposium, Western Research Institute, Laramie, WY.

Lytton, R. L. (2004). "Adhesive fracture in asphalt concrete mixtures." in *Asphalt Technology Handbook*, J. Youtcheff, ed., Marcel Dekker, Monticello, New York, In Press.

Lock, P. A., Jing, X. D., Zimmerman, R. W., and Schlueter, E. M. (2002). "Predicting the permeability of sandstone from image analysis of pore structure." *J. Appl. Phys.*, 92, 6311-6319.

Mallick, R. B., Cooley, Jr., L. A., Teto, M. R., Bradbury, R. L., and Peabody, D. (2001). "An evaluation of factors affecting permeability of Superpave designed pavements." *Presented at the 80th Annual Meeting of the Transportation Research Board,* Washington, D.C.

Marshall, T. J. (1958). "A relation between permeability and size distribution of pores." *J. Soil Sci.*, 9(1), 1-8.

Martys, N. S., Torquato, S., and Bentz, D. P. (1994). "Universal scaling of fluid permeability for sphere packings." *Physical Review E*, 50, 403-408.

Masad, E. (1998). "Permeability simulation of anisotropic reconstructed soil medium." Ph.D. dissertation, Washington State University, Pullman, WA.

Masad, E. (2004). "X-ray computed tomography of aggregates and asphalt mixes," *Materials Evaluation Journal, American Society for Nondestructive Testing.* 62(7), 775-783.

Masad, E., Birgisson, B., Al-Omari, A., and Cooley, A. (2004). "Analytical derivation of permeability and numerical simulation of fluid flow in hot-mix asphalt." *Journal of Materials in Civil Engineering*, ASCE, 16(5), 487-496.

Masad, E., Jandhyala, V. K., Dasgupta, J., Somadevan, N., and Shashidhar, N. (2002a). "Characterization of air void distribution in asphalt mixes using X-ray CT." *Journal of Materials in Civil Engineering, ASCE*, 14(2), 122-129.

Masad, E., Muhunthan, B., and Crowe, C. (2002b). "Numerical modeling of fluid flow in microscopic images of granular materials." *International Journal for Numerical and Analytical Methods in Geomechanics*, 26, 53-74.

Masad, E. A., Muhunthan, B., and Martys, N. (2000). "Simulation of fluid flow and permeability in cohesionless soils." *Water Resources Research*, 36(4), 851–864.

Masad, E., Muhunthan, B., Shashidhar, N., and Harman Th. (1999a). "Internal structure characterization of asphalt concrete using image analysis." *ASCE Journal of Computing in Civil Engineering (Special Issue on Image Processing),* 13(2), 88-99.

Masad, E., Muhunthan, B., Shashidhar, N., and Harman, Th. (1999b). "Quantifying laboratory compaction effects on the internal structure of asphalt concrete."

Transportation Research Record 1681, Transportation Research Board, Washington, D. C., 179-185.

Maupin, Jr., G. W. (2000). "Asphalt permeability testing in Virginia." *Journal of the Transportation Research Record 1723*, Transportation Research Board, Washington, D. C., 83-91.

Maupin, Jr., G. W. (January 2001). "Asphalt permeability testing: specimen preparation and testing variability." *Transportation Research Record 1767*, Transportation Research Board, Washington, D. C., 33-39.

Millington, R. J., and Quirk, J. P. (1959). "Permeability of porous media." *Nature*, 183, 387-388.

Mohammad, L. N., Herath, A., and Huang, B. (2003). "Evaluation of permeability of Superpave [registered trademark] asphalt mixtures." *Transportation Research Record 1832*, Transportation Research Board, Washington, D. C., 50-58.

Moore, P. J. (1979). "Determination of permeability anisotropy in a two-way permeameter." *Geotechnical Testing Journal*, 2(3), 167-169.

Mualem, Y. (1976). "A new model for predicting the hydraulic conductivity of unsaturated porous media." *Water Resources Research*, 12, 1248-1254.

Panton, R. (1984). *Incompressible flow*, John Wiley & Sons, Inc., New York.

Pare, J. J., Ares, R., Cabot, L., and Garzon, M. (1982). "Large scale permeability and filter tests at LG3." *Proc., 14th Congress on Large Dams*, Rio de Janeiro, 55(7), 103-122.

Patankar, S. V. (1980). *Numerical heat transfer and fluid flow*, Hemisphere Publishing Corporation, USA.

Patankar, S. V., and Spalding, D. B. (1970). "A calculation procedure for heat, mass and momentum transfer in three-dimensional parabolic flows." *Int. J Heat Mass Transfer*, 15, 1787-1806.

Pavement Work Tips. (1999). "Air voids in asphalt." Australian Asphalt Pavement Association, AAPA, 17.

Peric, M. (1985). "A finite volume method for the prediction of three-dimensional fluid flow in complex ducts." Ph.D. dissertation, Imperial College, London University, London, UK.

Petrovic, A. M., Siebert, J. E., and Rieke, P. E. (1982). "Soil bulk density analysis in three-dimensions by computed tomography scanning." *Soil Sci. Soc. Am. Journal*, 46(3), 445-450.

Pilotti, M. (2003). "Viscous flow in three-dimensional reconstructed porous media." *International Journal for Numerical and Analytical Methods in Geomechanics,* 27, 633-649.

Prowell, B. D., and Dudley, M.C. (2002). "Evaluation of measurement techniques for asphalt pavement density and permeability." *Transportation Research Record 1789*, Transportation Research Board, Washington, D. C., 36-45.

Rajani, B. B. (1988). "A simple model for describing variation of permeability with porosity for unconsolidated sands." *In Situ*, 12(3), 209-226.

Rhie, C. M., and Chow, W. L. (1983). "Numerical study of the turbulent flow past an airfoil with trailing edge separation." *AIAA J*, 21, 1525-1532.

Richardson, D. N. (1995). "Drainability characteristics of granular pavement base material." *Journal of Transportation Engineering*, 123(5), 385-392.

Roberson, J. A., and Crowe, C. T. (1997). *Engineering fluid mechanics*, 6th Edition, John Wiley & Sons, Inc., New York.

Roberts, F. L., Kandhal, P. S., Brown, E. R., Lee, D. Y., and Kennedy, T. W. (1996). *Hot mix asphalt materials, mixture design, and construction*, 2nd Edition, NAPA Education Foundation, Lanham, Maryland.

Romero, P. (2000). "Laboratory evaluation of the PQI model 300." *Research Report: DTFH61-00-P-00549, Bituminous Mixtures Laboratory, Turner-Furbank Highway Research Center, Federal Highway Administration*, McLean, VA.

Romero, P., and Masad, E. (2001). "On the relationship between the representative volume element and mechanical properties of asphalt concrete." *Journal of Materials in Civil Engineering, ASCE*, 13(1), 77-84.

Scheidegger, E. (1974). *The physics of flow through porous media*, Univ. of Toronto, Press, Toronto.

Shackelford, C. D., Benson, C. H., Katsumi, T., Edil, T. B., and Lin, L. (2000). "Evaluating the hydraulic conductivity of GCLs permeated with non-standard liquids." *Geotextiles and Geomembranes*, 18(2), 133-161.

Shang, B. Z., Hamman, J. G., Chen, H. L., and Caldwell, D. H. (2003). "A model to correlate permeability with efficient porosity and irreducible water saturation." *Proceedings-SPE Annual Technical Conference and Exhibition*, Denver, CO, 2203-2210.

Shashidhar, N. (1999), "X-ray tomography of asphalt concrete," *Transportation Research Record 1681*, Transportation Research Board, Washington, D. C., 186-192.

Soonswang, P., Tia, M., and Bloomguist, D. (1991). "Factors affecting the strength and permeability of concrete made up with porous limestone." *ACI Materials Journal (American Concrete Institute)*, 88(4), 400-406.

Synolakis, C. E., Zhou, Z., and Leahy, R. M. (1996), "Determination of internal deformation field in asphalt cores using X-ray computer tomography," *Transportation Research Record 1526*, Transportation Research Board, Washington, D. C., 135-141.

Tan, S. A., Fwa, T. F., and Chuai, C. T. (1997). "A new apparatus for measuring the drainage properties of porous asphalt mixes." *Journal of Testing and Evaluation,* JTEVA, 25(4), 370-377.

Tan, S. A., Fwa, T. F., and Chuai, C. T. (1999). "Automatic field permeameter for drainage properties of porous asphalt mixes." *Journal of Testing and Evaluation*, JTEVA, 27(1), 57-62.

Tashman, L., Masad, E., Little, D., and Lytton, R. (2004). "Damage evolution in triaxial compression tests of HMA at high temperatures." *Journal of the Association of Asphalt Paving Technologists,* 73, In Press.

Tashman, L., Masad, E., Crowe, C., and Muhunthan, B. (2003). "Simulation of fluid flow in granular microstructure using a non-staggered grid scheme." *Computers & Fluids,* 32, 1299-1323.

Taylor, S. W., Milly, P. C. D., and Jaffe, P. R. (1990). "Biofilm growth and the related changes in the physical properties of a porous medium 2. permeability." *Water Resources Research*, 26(9), 2161-2169.

Torquato, S. (2001). *Random heterogeneous materials: microstructure and macroscopic Properties*, Springer-Verlag, Inc., New York.

Walsh, J. B., and Brace, W. F. (1984). "The effect of pressure on porosity and the transport properties of rocks." *J. Geophys. Res.*, 89, 9425-9431.

Wang, J. C., Leung, C. F., and Chow, Y. K. (2003a). "Numerical solutions for flow in porous media." *International Journal for Numerical and Analytical Methods in Geomechanics,* 27, 565-583.

Wang, L. B., Frost J. D., and Shashidhar N. (2001). "Microstructure study of Westrack mixes from X-ray tomography images," *Transportation Research Record 1767*, Transportation Research Board, Washington, D. C., 85-94.

Wang, L. B., Frost, J. D., Voyiadjis G., and Harman T. P. (2003b). "Quantification of damage parameters using X-ray tomography images," *Journal of Mechanics of Materials*, 35, 777-790.

Watson, D. E., Masad, E., Moore, K. A., Williams, K., and Cooley L. A. (2004). "Verification of VCA testing to determine stone-to-stone contact of HMA mixtures." Accepted for publication in *Transportation Research Record,* Transportation Research Board, Washington, D. C., In Press.

Wit, K. E. (1966). "Apparatus for measuring hydraulic conductivity of undisturbed soil samples." *American Society of Testing and Materials*, STP 417, 72-83.

Wyckoff, R. D., and Botset, H. G. (1936). "The flow of gas-liquid mixtures through unconsolidated sands." *Physics*, 7(9), 325-345.

Zube, E. (1962). "Compaction studies of asphalt concrete pavements as related to the water permeability test." *Highway Research Board*, 358, 12-38.

VITA

Aslam Ali Mufleh Al Omari was born in Zarka, Jordan, on June 24, 1972. He received his B.S. and M.S. degrees in Civil Engineering from Jordan University of Science and Technology in June 1995 and February 1998, respectively. He worked for six months at the Applied Science University in Jordan and then for two years at Dubai Technical Secondary School in the United Arab Emirates. He started his Ph.D. in Civil Engineering at Washington State University in May 2001, transferred to Texas A&M University in January 2003, and received his Ph.D. in Dec. 2004.

Some of his publications are:

Al-Omari, A., and Masad, E. (2004). "Three Dimensional Simulation of Fluid Flow in X-ray CT Images of Porous Media." *International Journal for Numerical and Analytical Methods in Geomechanics*, 28(13), 1327-1360.

Al-Omari, A., Tashman, L., Masad, E., Cooley, A., and Harman, T. (2002). "Proposed Methodology for Predicting HMA Permeability." *Journal of the Association of Asphalt Paving Technologists,* 71, 30-58.

Al-Omari, A. and Masad, E. (2004). "Three Dimensional Simulation of Fluid Flow in Granular Material Microstructure." *GEO2004: Advances in Geotechnical Engineering with Emphasis on Dam Engineering,* Irbid, Jordan, 177-199.

His permanent address is: Jordan, Irbid, Al-Insherah Street.

Home Phone is: +962 2 725 5476

His e-mail Address is: aslam400@yahoo.com